Lift-Induced Wake Re-Energization for a VAWT-Based Multi-Rotor System

T.J. Broertjes

Delft University of Technology

TU Delft

Lift-Induced Wake Re-Energization for a VAWT-Based Multi-Rotor System

by

T.J. Broertjes

to obtain the degree of Master of Science
at the Delft University of Technology,
to be defended publicly on April 12, 2024 at 13:00.

Student number:	4552326	
Project duration:	February, 2023 — April, 2024	
Thesis committee:	A. Sciacchitano,	TU Delft, supervisor
	C.J. Simao Ferreira,	TU Delft, supervisor
	D. Bensason,	TU Delft, supervisor
	A. van Zuijlen	TU Delft, Chair
	G. la Rocca	TU Delft, Examiner

An electronic version of this thesis is available at `http://repository.tudelft.nl/`.

TU Delft

Preface

The work which lies in front of you is the final piece of what is called a Master of Science in Aerospace Engineering at the Delft University of Technology. At the same time, it also concludes my journey as a student. A journey which started almost seven years ago, in search of a challenge, fueled by a passion for motorsports and aviation. A journey on which seven years later I look back with fond memories. None of this would have been possible without the support and guidance of numerous individuals.

I want to start by thanking my supervisors Andrea, Carlos, and David. Without you, this project wouldn't have existed. Andrea our weekly meetings were invaluable learning opportunities, and I am thankful for your mentorship and insights throughout the process. Carlos, your passion and enthusiasm for this project, which particularly showed during the wind tunnel experiment, left a lasting impression on me. And finally David, no matter what the issue was, I could always reach out. I truly enjoyed working with you. Furthermore, my gratitude extends to the team at DEMO for their assistance during the manufacturing of the wind tunnel model, and the technical staff at both the High-Speed and the Low-Speed Laboratory for their invaluable support throughout the preparation and execution of my experimental campaigns.

On a more personal note, I would like to express my gratitude to all my friends and family who have supported me along this unforgettable journey. To Max, Reinier, Stijn, and Peter, you have made my time here in Delft so much more fun, the friendships we have created here are built to last. To my father and my sister, of whom I know they are always there when I need them. To Nida, who was always there when I needed it the most, I don't think I could have done this without you by my side. And lastly to my mother, who supported me everywhere she could, but unfortunately was not allowed to see the end of this journey. Mom, I've made it, I know you're watching over me with pride. It now is time for me to explore the world.

Thomas Jesse Broertjes
Delft, March 2024

Abstract

In response to the urgent need for renewable energy amidst the escalating impacts of global warming, this study delves into the forefront of wind energy research, particularly focusing on the innovative Multi-Rotor System (MRS). The MRS concept offers a promising departure from the prevailing trend of scaling up traditional turbines, instead proposing a configuration comprising multiple smaller rotors mounted on a single support frame. This approach, identified for its inherent upscaling advantages, presents an opportunity to reduce costs and weight relative to conventional Horizontal Axis Wind Turbines (HAWTs). While the concept is not entirely novel, its application with Vertical Axis Wind Turbines (VAWTs) is. Recent studies have demonstrated the significant potential of the VAWT-based MRS, showcasing comparable power performance to large HAWTs while enhancing Operations and Maintenance (O&M) aspects. Furthermore, the adaptable support frames of the MRS facilitate the integration of wake control devices, such as external lift-generating wings, which introduce cross-flow loading to rapidly re-energize the wake. However, despite these advancements, understanding the wake dynamics within MRS systems, particularly concerning their implications for wind farm applications, remains limited.

The current work aims to investigate the intricate near-wake dynamics of the VAWT-based MRS and study the effects of external lift-generating wings on the deflection and recovery of the wake. To do so, a scaled wind tunnel model of such a VAWT-based system has been designed together with a set of removable high-lift wings. These, in turn, have been tested in the Open Jet Facility of the Delft University of Technology to gather insight into the behaviour of the near-wake. Tomographic Particle Image Velocimetry using Helium Filled Soap Bubbles has been deployed in combination with load measurements to gather data.

Load measurements revealed that the thrust coefficient behaviour of the MRS closely resembles that of single-rotor VAWTs, with an additional thrust induced when the external lift-generating devices are present, attributed to accelerated flow on the suction side of the wings. Furthermore, the PTV measurements have provided a detailed visualization of the near-wake, showcasing symmetric wake structures and lateral deflection induced by the presence of individual rotors. The introduction of external lift-generating wings significantly altered wake behaviour, inducing lateral contraction and promoting streamwise momentum recovery through enhanced vertical advection. Furthermore, analysis of velocity deficit recovery highlighted substantial improvements in power recovery behind the MRS with external wings.

The findings presented in this work underscore the potential of the VAWT-based MRS, particularly when such a system is equipped with lift-generating devices. The presence of such devices effectively manipulates the near-wake of the turbine, enhancing wind farm efficiency, and thereby advancing innovative wind energy solutions.

Contents

List of Figures

List of Tables

Nomenclature

Symbols

α	Angle of attack	$^\circ$
δ	Boundary layer thickness	m
Γ	Circulation	m^2/s
κ	Von Karman Constant	–
λ	Tip speed ratio	–
ω	Angular velocity	rad/s
ω	Vorticity	1/s
Ψ	Inflow angle	$^\circ$
ρ	Density	kg/m^3
θ	Azimuth angle	$^\circ$
θ_p	Blade pitch	$^\circ$
A	Area	m^2
A_{act}	Actuator surface area	m^2
B	Number of blades	–
b	Wing/blade span	m
c	Chord length	m
C_D	Drag coefficient	–
C_L	Lift coefficient	–
c_l	Section wise lift coefficient	–
C_P	Power coefficient	–
C_T	Thrust coefficient	–
D	Actuator surface width	m
D	Drag	N
d	Rotor diameter	m
F	Force	N
G	Geostrophic wind velocity	m/s
H	Actuator surface height	m
h	Rotor height	m
L	Lift	N
n	Number of rotors	–
P	Power	W
p	Pressure	Pa
q_∞	Free stream dynamic pressure	Pa
R	Rotor radius	m
Re	Reynolds number	–
S	Wing/blade surface area	m^2
T	Thrust	N
u	Streamwise velocity	m/s
u^*	Friction velocity	m/s
U_∞	Free stream velocity	m/s
V	Velocity	m/s
v	Lateral velocity	m/s
w	Downwash velocity	m/s
w	Vertical velocity	m/s
z_0	Roughness height	m

Sub- and superscripts

$'$	Per unit span
$'$	Turbulent value
$\bar{}$	Time-averaged value
∞	Free stream value
c	Chord based
n	Normal component
t	Tangential component
w	Wind
x	Streamwise component
y	Lateral component
z	Vertical component
ind	Induced component
max	Maximum value
rel	Relative component
tot	Total quantity

Abbreviations

ABL	Amospheric Boundary Layer
CCW	Counter-clockwise
CW	Clockwise
FOV	Field of View
HAWT	Horizontal Axis Wind Turbine
HFSB	Helium-Filled Soap Bubbles
LE	Leading Edge
LES	Large Eddy Simulation
MRS	Multi-Rotor System
O&M	Operations and Maintenance
OJF	Open Jet Facility
OTF	Optical Transfer Function
PIV	Particle Image Velocimetry
PTV	Particle Tracking Velocimetry
RANS	Reynolds Averaged Navier Stokes
RNA	Rotor-nacelle assembly
STB	Shake the Box
TE	Trailing Edge
TSR	Tip Speed Ratio
VAWT	Vertical Axis Wind Turbine
VSC	Volume Self Calibration

1

Introduction

With the effects of global warming becoming increasingly apparent, the need for renewable energy and achieving net-zero emissions has never been greater. Extreme heat waves in Europe and floods in India and Pakistan are just a few of the events that have occurred in 2023 [9]. In 2015 the United Nations brought the Paris Agreement to life, where the ambitious target of limiting global temperature rise to 1.5 degrees Celsius above pre-industrial levels was set. Despite the efforts, progress towards these goals has fallen short and the energy transition has fallen behind schedule [1]. It is evident that addressing climate change and meeting these targets demand not only commitment but also significant advancements in renewable energy research and development. A large part of these advancements happen within the realm of wind energy, where the main trends are moving wind farms offshore [72], and scaling up turbines, both with the aim of increasing wind farm power production. These developments not only focus on traditional horizontal axis wind turbines (HAWTs), or more recently, vertical axis wind turbines (VAWTs) but also on entirely new concepts such as the 'Multi-Rotor System'.

The emergence of the Multi-Rotor System, also referred to as the MRS, presents an attractive alternative to the prevailing trend of upscaling conventional turbines. It offers a new approach to large-scale wind capture systems, utilising multiple smaller rotors instead of a single large rotor. The concept capitalizes on inherent upscaling advantages, manifested in reduced costs and weight relative to traditional HAWTs [33]. While the concept of an MRS comprising HAWTs is not novel [31], its realization with VAWTs is innovative. Recent investigations into the VAWT-based MRS have shown remarkable potential, demonstrating power performance on par with large HAWTs, while simultaneously enhancing Operations and Maintenance (O&M) aspects [32]. Furthermore, the MRS brings the additional advantage that its support frames can be adapted such that they can serve as integral housing for wake control devices, of which a notable example includes the incorporation of external lift-generating devices introducing cross-flow loading, facilitating rapid re-energisation of the wake. However, despite the promise of this novel concept, understanding the wake structure within such systems remains limited, particularly concerning its implications for wind farm applications.

This thesis therefore aims to shed light not only on the intricate wake dynamics of the VAWT-based MRS but also on how the addition of external lift-generating devices affects this near-wake. To do so, a scaled wind tunnel model of an MRS with removable high-lift wings has been designed and tested in the Open Jet Facility of the TU Delft. Large-scale tomographic Particle Tracking Velocimetry measurements using helium-filled soap bubbles, in combination with load measurements, have been taken to acquire information on the wake and performance of such a system, and how this is affected by the addition of the high-lift wings. As a result, this work aims to give insight into the flow field characteristics by shedding light not only on the velocity and vorticity field in the near-wake but also on the recovery of streamwise momentum and available power.

This report starts by familiarizing the reader with the current state-of-the-art of the wind energy sector and an introduction to the MRS concept in chapter 2. Additionally, it elaborates on the principle of lift-generating wings, and the Particle Tracking Velocimetry method. Chapter 2 concludes with a short synthesis of the existing literature, and the research questions to be answered in this work are posed. In chapter 3 the design of the MRS wind tunnel model and high-lift wings is presented, together with the PTV setup. This is then followed by chapter 4, which presents and discusses the acquired results. These results are concluded upon in chapter 5, together with several recommendations for future research.

2
Background

This chapter serves as an introductory chapter, not only familiarising the reader with the state-of-the-art within the realm of wind energy but also bringing the reader up to speed with the concept of high-lift wings and the measurement technique used. In section 2.1 existing research on wind farm aerodynamics and wake control techniques are presented. This is then followed by the introduction of the Multi-Rotor System concept in section 2.3. The concept of high-lift is treated in section 2.4, after which PTV is elaborated on in section 2.5. This chapter concludes with a summary of the main takeaways from the state-of-the-art, followed by the current research gap and the research questions to fill this gap.

2.1. Wind Farm Aerodynamics

As already mentioned in the introduction of this report, the wind energy industry has been working to increase wind farm power production to achieve sustainability goals. This power is dictated by the kinetic energy of the wind, where the maximum power P_w available in the wind depends on the local wind speed. This relation between wind speed and available power is illustrated in Equation 2.1. The local velocity, and thus power available is however not constant but varies with height from the surface of the Earth due to the boundary layer of the Earth, also referred to as the Atmospheric Boundary Layer (ABL). As a result, wind turbines do not operate in constant conditions. Additionally, as a turbine extracts power from the wind, it decreases the flow velocity locally as a result of this power extraction, inducing a low energy high turbulence wake into the flow.

$$P_w = \frac{1}{2}\rho A U_\infty^3 \tag{2.1}$$

Several studies have been performed on the shape and the behaviour of the ABL. The works of Porté-Agel et al. [46] and Stevens and Meneveau [61] both provide elaborate reviews of existing studies on flow structures within wind farms. The ABL is driven by geostrophic wind, of which its velocity magnitude is denoted at G. Within the boundary layer, the velocity profile is driven by the balance between pressure forces, Reynolds stresses, and Coriolis forces which are induced by the rotation of the Earth. Thermal stratification affects the mean velocity distribution within the ABL, as well as the intensity of turbulence within the flow. Close to the surface, below a thickness of $z = 0.1 - 0.2\delta$, the boundary layer is also affected by the surface roughness such as trees, buildings, and mountains. This region is also known as the surface layer. Equation 2.2 gives the relation for the mean flow velocity u at a given height z within this surface layer region within the ABL. In this equation, u^* is the friction velocity, $\kappa = 0.4$ the Von Karman constant, z_0 a value related to the surface roughness, and $\Psi_M\left(\frac{z}{L}\right)$ a term related to the ABL stability ($\Psi_M = 0$ for neutral conditions).

$$u(z) = \frac{u^*}{\kappa}\left[ln\left(\frac{z}{z_0}\right) - \Psi_M\left(\frac{z}{L}\right)\right] \tag{2.2}$$

From this relation, one can conclude that higher up in the atmosphere wind velocities are higher, and thus more power is available. Additionally, a more energised boundary layer can be found in locations

with low surface roughness (such as offshore), and at stable boundary layer conditions, hence the reason why wind farms nowadays are more often moved offshore. Furthermore, the thickness of the ABL is not fixed. For neutral conditions, the ABL thickness δ is in the order of 1km. This thickness can, however, vary a lot as for a stable ABL it can be in the range of a few hundred meters, but for strongly convective conditions it can be in the range of several kilometres.

As mentioned, when a turbine extracts power from the flow it inflicts a wake on it. The work of Chamorro and Porté-Agel [17] investigated how this wake affects the shape of the ABL through an experimental study, of which an extract of their results is presented in Figure 2.1. Their results show how the ABL recovers to its original profile as it travels downstream. Additionally, they reported an increase in turbulence intensity in the wake of the turbine.
Both the momentum deficit and the increased turbulence intensity in the wake of an individual turbine are of great interest when considering wind farm design. The reduced momentum in the flow affects the available power subsequent turbines can extract, and the increased turbulence affects the structural health of these machines as has been presented in the study of Lee et al. [37]. Here it was shown with numerical simulations that increased turbulence in the wake increases fatigue loads on downstream turbines significantly.

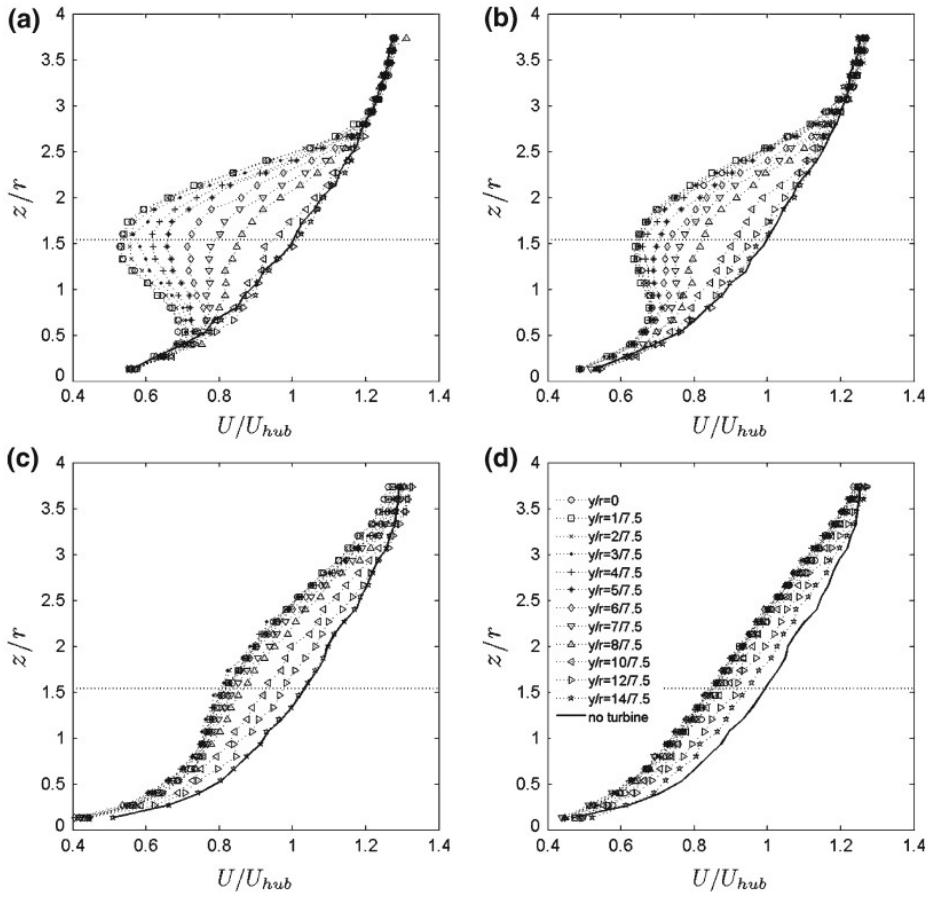

Figure 2.1: Normalized velocity profiles of a HAWT in boundary layer flow at different downstream locations. **a** $x/d = 3$; **b** $x/d = 5$; **c** x/d 10; **d** $x/d = 15$, with d being the rotor diameter. The horizontal line represents the centre of the rotor disc. (results from Chamorro and Porté-Agel [17])

Due to the aforementioned negative effects on structural health and power extraction, the wind farm community aims to minimize wake interference effects. To achieve this wake deflection techniques and optimal wind farm layouts are studied with the aim of maximising wake re-energisation. To optimise wind farm yield it is important that the momentum losses are being replenished. In the work of Hamilton et al. [25], the importance and mechanics of vertical replenishment of the mean

kinetic energy in the flow are studied. This vertical entrainment of momentum is driven by large-scale structures within the flow and is important for the power extraction of downstream turbines. In the work of Verhulst and Meneveau [69] an LES study on a wind farm is performed to identify the effect of synthetic vertical forcing on the vertical entrainment of mean kinetic energy. This forcing, which was treated as a proof of concept and not an already existing device, was found to have a significant effect on the power generated by the wind farm. It is important to note, that upward forcing yielded significant power gains whereas a downward forcing did not have a large effect on power production. These results are in line with the experimental results of Bossuyt et al. [10], who achieved similar results inducing this vertical forcing by tilting the rotor disc of a horizontal axis turbine. The results of these studies are interesting, as they indicate gains in wind farm power production could be obtained through external lift-generating devices and the induction of vertical forcing. Importantly, the synthetic forcing introduced by [69] did not introduce large-scale structures into the flow, highlighting a nuanced approach to enhancing wind farm efficiency.

2.1.1. Wake Control for HAWTs

Next to enhancing energy replenishment of the wake, cross-flow forcing also plays an important role in wake deflection. This concept is often applied to enhance the power production of wind farms, where the wake of leading turbines is deflected away from turbines downstream. As a result, the leading turbine experiences a slightly diminished production of power, however as the downstream turbines operate in a cleaner, high-energy flow, the overall power production of the wind farm is enhanced. The process of wake deflection, for HAWTs often achieved by yawing the rotor disc, visualised in Figure 2.2, has been evaluated extensively within the literature. Where the work of Medici and Alfredsson, [43] and [44], Jimenez et al. [34], and Schottler et al. [52] dive into the mechanics behind this wake deflection, Campagnolo et al. [14] and Bastankhah and Porté-Agel [7] have studied the effects wake deflection has on wind farm power production. In the experimental study of Campagnolo et al., it was reported that deflecting the wake through yaw can result in a total increase in power production of 21% depending on the layout of the wind farm. Similar results were found by Bastankhah and Porté-Agel, who reported an increase in efficiency of up to 17% when comparing farm performance to non-yawed conditions. The work of Fleming et al. [22] and Howland et al. [27] invigorate these findings through field tests, where both studies reported a measurable increase in power generation when employing wake deflection as a wake-control strategy.

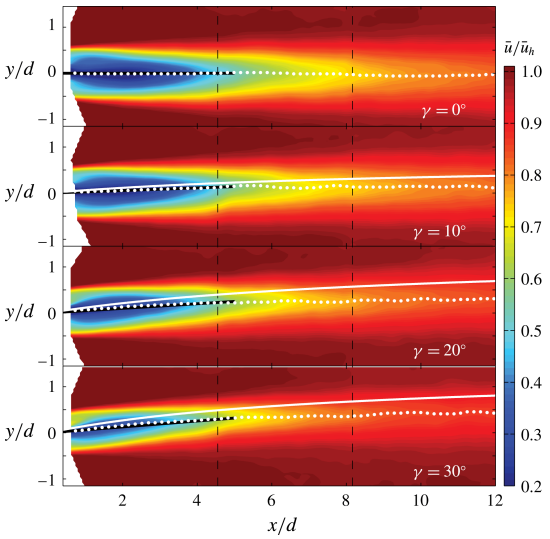

(a) Normalised mean streamwise velocity of the HAWT wake for different yaw angles.

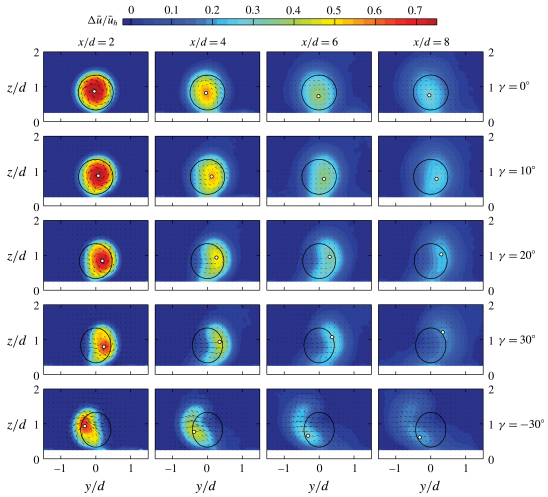

(b) Normalised mean streamwise velocity deficit of the HAWT wake for different yaw angles.

Figure 2.2: Stereo-PIV results of the horizontal axis wind turbine wake in yaw. Figures adapted from [7].

2.2. Vertical Axis Wind Turbines

As this work revolves around the concept of a VAWT-based Multi-Rotor System, the following section delves into the Vertical Axis Wind Turbine. Where HAWTs have traditionally dominated wind energy research, recent years have seen a resurgence of interest in VAWTs. The roots of the vertical axis turbine trace back to ancient Persia in the 9th century, Figure 2.3, initially adopting drag-based designs [2]. As time moved on, VAWT designs have evolved from these simple drag-based designs to more sophisticated lift-based configurations. During the 1980s significant research was conducted on the vertical axis concept, however, attention shifted rather fast to its horizontal axis counterpart. Renewed interest in VAWTs emerged around 2010, one of the reasons being the shift towards offshore wind energy. VAWTs bring the benefit of having their gearbox and generator located much lower in their structure, resulting in a much lower centre of gravity. This not only results in ease of access during maintenance, resulting in a reduction in operating cost, but also results in a cost reduction when it comes down to the manufacturing of the foundation. In addition, this low centre of gravity and their symmetric design make them a feasible option when considering floating structures. To add to that, Rolin and Porté-Agel [47] have shown the potential of higher power densities compared to HAWTs when placed in a windfarm as a result of faster wake recovery, allowing the turbines to be more closely spaced.
The following section will start with introducing the reader to the perhaps complex aerodynamics of the VAWT system, after which a detailed look is presented at existing research on the wake dynamics and re-energisation of these machines.

Figure 2.3: Persian vertical axis windmills, primarily used for grist milling and in the sugarcane industry.[1]

2.2.1. Fundamental VAWT Aerodynamics

Having discussed the resurgence of interest in the VAWT, the current subsection will delve into the fundamental aerodynamic principles that govern their operation. The theory presented focuses solely on the lift-driven VAWT, where the theory has been taken from the dissertation of De Tavernier [18].
For the following discussion consider a 2D blade element as presented in Figure 2.4. Here the top view of a 3-bladed VAWT rotor is represented. An arbitrary VAWT design however would be defined by its radius R, number of bladed B, blade chord c, blade length H, swept area A, rotating at an angular velocity ω.
At a given 2D blade element as presented in Figure 2.4, as the turbine rotates, three different velocity components act. The two primary components are the freestream velocity V_∞, and the rotational velocity $V_{rot} = \omega R$. A third velocity component, the induced velocity V_{ind} is a result of the forcefield around the turbine and varies over the rotation of the turbine. These individual components can be decomposed into V_x and V_y, as represented in Equation 2.3 and Equation 2.4, being the inflow and cross-flow direction respectively, or into V_t and V_n, Equation 2.5 and Equation 2.6, being the tangential and normal velocity as perceived by the blade. From this the relative velocity V_{rel} as perceived by the blade is given by Equation 2.7.

[1] https://www.amusingplanet.com/2014/07/the-ancient-windmills-of-nashtifan.html

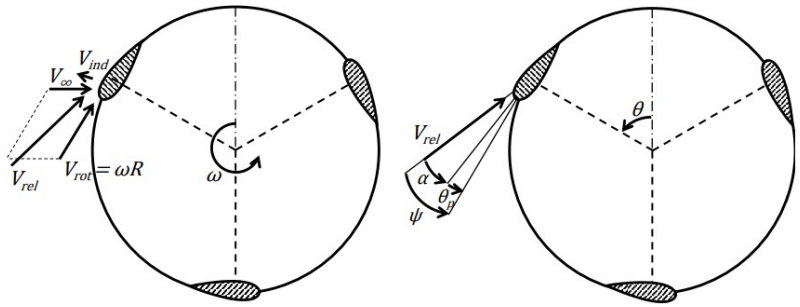

(a) Relative velocity (b) Angles

Figure 2.4: Representation of the 2D VAWT blade element, representing velocity vectors and angle definitions. Figure from De Tavernier [18].

$$V_x = V_\infty + \omega R \cdot cos(\theta) + V_{ind,x} \tag{2.3}$$

$$V_y = \omega R \cdot sin(\theta) + V_{ind,y} \tag{2.4}$$

$$V_t = V_x \cdot cos(\theta) + V_y \cdot sin(\theta) \tag{2.5}$$

$$V_n = V_x \cdot sin(\theta) - V_y \cdot cos(\theta) \tag{2.6}$$

$$V_{rel} = \sqrt{V_x^2 + V_y^2} \tag{2.7}$$

The angle of attack as perceived by the blade element then follows from Equation 2.8, with θ_p being its pitch angle.

$$\alpha = tan^{-1}\left(\frac{V_n}{V_t}\right) - \theta_p \tag{2.8}$$

Before the discussion continues it is important to set some definitions in place regarding the different angles. For the azimuth angle θ it is common practice to define this as the angle between the cross-flow direction and blade location. As a result θ has a value between 0° and 180° for the upwind half of the turbine, and 180° and 360° downwind. Inflow angle Ψ is the angle between V_{rel} and the tangent of the blade path, and θ_p between the blade chord line and the tangent of the blade path.
Considering the blade element approach, the lift and drag force acting on the blade per unit span is given by Equation 2.9 and Equation 2.10 respectively. These forces can be decomposed into a normal and tangential component according to Equation 2.11 and Equation 2.12. Figure 2.5 visualizes the forces acting on the 2D blade element. It is important to note that both $C_L(\alpha)$ and $C_D(\alpha)$ are functions of α, and as V_n and V_t vary over the rotation of the turbine, where α is positive over the upwind section of the rotor, but becomes negative when travelling over the downwind section. As a result, the forces acting on the blades also vary over the rotation.

$$L = \frac{1}{2}\rho V_{rel}^2 \cdot C_L(\alpha) \cdot c \tag{2.9}$$

$$D = \frac{1}{2}\rho V_{rel}^2 \cdot C_D(\alpha) \cdot c \tag{2.10}$$

$$F_n = L \cdot cos(\Psi) + D \cdot sin(\Psi) \tag{2.11}$$

$$F_t = L \cdot sin(\Psi) - D \cdot cos(\Psi) \tag{2.12}$$

The power, which is the rate of work performed by the turbine over a single rotation, is then defined by Equation 2.13, and the thrust, which is the force the turbine exerts on the flow, is given by Equation 2.14. The power and thrust coefficient C_P and C_T can be computed with Equation 2.15 and Equation 2.16.

$$P = \frac{1}{2\pi}\int_0^{2\pi} B \cdot F_t(\theta) \cdot \omega R d\theta \tag{2.13}$$

$$T = \frac{1}{2\pi} \int_0^{2\pi} B \cdot (F_t(\theta)cos(\theta) - F_n(\theta)sin(\theta))d\theta \tag{2.14}$$

$$C_P = \frac{P}{0.5\rho A V_\infty^3} \tag{2.15}$$

$$C_T = \frac{T}{0.5\rho A V_\infty^2} \tag{2.16}$$

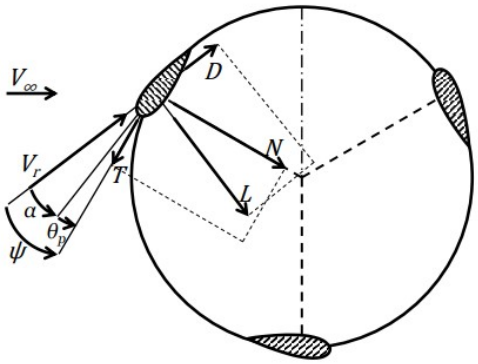

Figure 2.5: Forces acting on the 2D VAWT blade element. Figure from [18].

2.2.2. Unsteady VAWT Aerodynamics

From the analysis above, it became evident that the blade loading of the VAWT varies over its rotation due to the variation in the angle of attack and inflow the blades experience. As a result, several unsteady aerodynamic phenomena occur at the blade level. The flow effects of interest, dynamic stall, flow curvature, and blade-vortex interaction, are briefly touched upon in the following paragraphs.

Dynamic Stall

The term "dynamic stall" usually describes the interaction between the separation of airflow at the trailing edge (TE) and leading edge (LE) of an airfoil. This phenomenon occurs when the airfoil experiences changes in pressure distribution and boundary layer development, often resulting from alterations in the incoming airflow patterns over the airfoil's surface. Figure 2.6 shows the five different stages of dynamic stall, and the effect it has on the normal force coefficient. In short, LE separation is initiated. As a result, a LE vortex is formed, which starts to grow and convects downstream. Due to the vortex travelling over the surface toward the TE, the flow starts to fully separate, after which the flow can reattach again and the loads return to their pre-stall values.
Dynamic stall typically occurs at low tip-speed ratios (TSR, $\lambda = \frac{\omega R}{V_\infty}$), as the amplitude of the angle of attack α increases for decreased TSR. It does not only affect turbine loading but also the dynamics of the wake.

Flow Curvature

The rotational motion of wind turbine blades leads to varying airflow along the blade's chord. This variation in airflow causes the angle of attack of the airfoil to change at different points along the blade's length. In a sense, this changing angle of attack affects the blade's effective camber if we were to consider it as a virtual airfoil in a uniform, non-rotating airflow. This effect, as illustrated in Figure 2.7, is known as flow curvature.

Blade-Wake Interaction

Blade-wake interaction is an inherent feature of VAWTs. As the blades of the turbine rotate they constantly shed vortices into the wake. In the upwind section of the rotor smooth flow is expected, however, in the downwind half of it, these vortices that have been shed in the upwind section interact with the blades passing the downwind section. As a result, the blades in the downwind section experience large oscillations in the induced velocity.

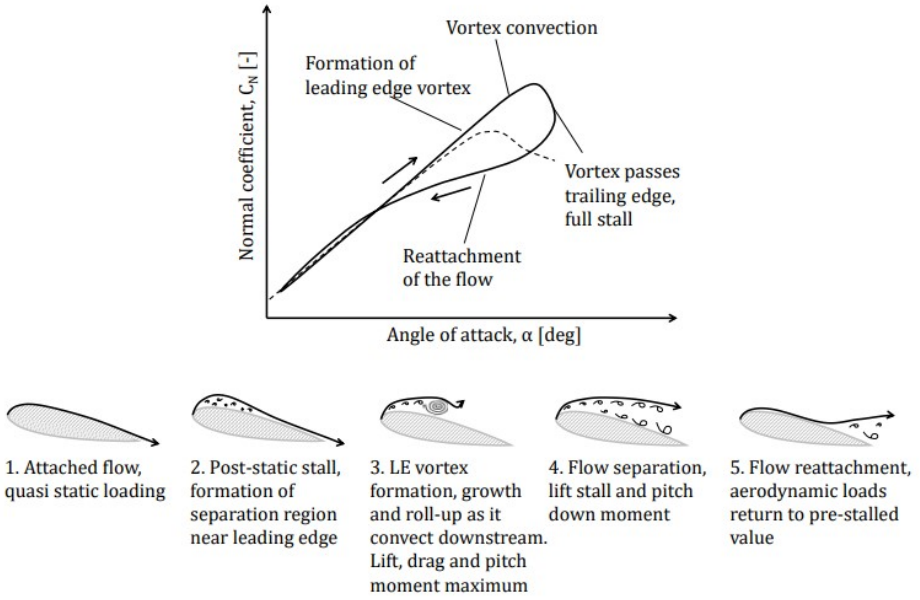

Figure 2.6: Phases of dynamic stall. Figure from [18].

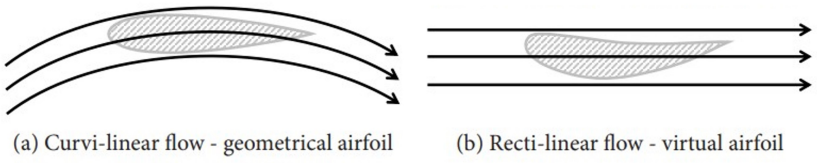

Figure 2.7: Visualistion of flow curvature. Figure from [18].

2.2.3. Wake Dynamics of VAWTs

Due to the interest in the behaviour of the wake of a VAWT-based MRS, it is important to get a basic understanding of the wake dynamics of the isolated VAWT. This wake has been studied extensively by several experimental studies, to understand its complex dynamics. As the VAWT rotates, it imparts vorticity into the surrounding flow, particularly near its blade tips. The detailed study by Ferreira [21] highlights the shedding of trailing and tip vortices along the blade's span, forming counter-rotating vortex pairs that influence the wake structure. This observation was further studied by Tescione et al. [64], where stereoscopic particle image velocimetry (PIV) was employed to study the near wake of the VAWT. The results revealed significant wake asymmetry, characterized by a skewed velocity profile with a pronounced expansion on the windward side. Furthermore, an earlier breakdown of tip vortices was found when compared to the HAWT counterpart, which in turn might contribute to faster recovery of the wake. In the study of Ryan et al. [48] the three-component mean velocity field around and downstream of a VAWT was measured through magnetic resonance velocimetry. They observed a strong counter-rotating vortex pair on the windward side of the turbine, dictating the shape and asymmetry of the wake. This vortex pair was found to entrain high-energy freestream flow into the wake, aiding its recovery. In addition, they studied the effect of TSR, where it was found that the strength of this counter-rotating vortex pair increased for larger TSR, increasing the asymmetry of the flow. Furthermore, in the work of Rolin and Porté-Agel [47], a small-scale VAWT submerged in a boundary layer flow was studied through stereo-PIV. They also identified, similar to the work of Ryan et al., that the strong pair of counter-rotating vortices on the windward side of the VAWT is the principal cause of wake re-energisation by studying the mean kinetic energy budget of the wake. In a recent study by Huang et al. [29], counter-rotating vortex pairs were once again observed, resulting in a wake deflection towards the windward side of the VAWT. Consistent with the findings of Rolin and Porté-Agel, this deflection is associated with the turbine's lateral thrust.

The abovementioned studies show the importance of the counter-rotating vortex pair in the wake dynamics of the VAWT. A visualisation of the VAWT's vortex system, which has been taken from the study of Boudreau and Dumas [11], is presented in Figure 2.8. It can be concluded that the trailing vortices, whose strength is related to the lateral load of the turbine, are responsible for the wake asymmetry and re-energisation. As a result, strengthening them suggests an enhanced recovery of the wake. Studies covering this will be elaborated on in the next section.

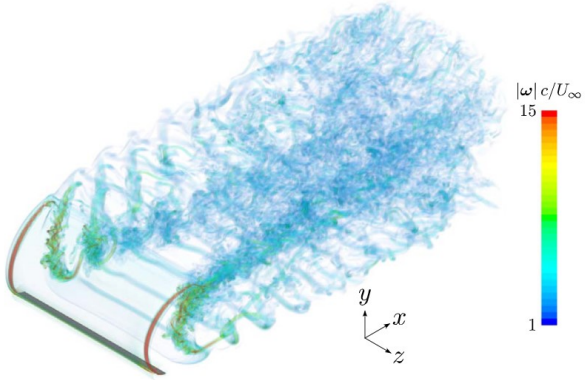

Figure 2.8: Visual rendering of the vorticity magnitude in the wake of the VAWT. Graphic adapted from Boudreau and Dumas [11].

2.2.4. Wake Control for VAWTs

Where the concept of wake control for HAWTs, which was touched upon earlier in this chapter, has been treated extensively in the literature, the concept of wake deflection and re-energisation for VAWTs is still relatively young. For HAWTs, it was found this could be achieved by introducing cross-flow loading by yawing or tilting the rotor disc, however, for VAWTs other techniques must be applied. Wake deflection for VAWTs still relies on the same principle of cross-flow loading as HAWTs, but this loading must be achieved differently.

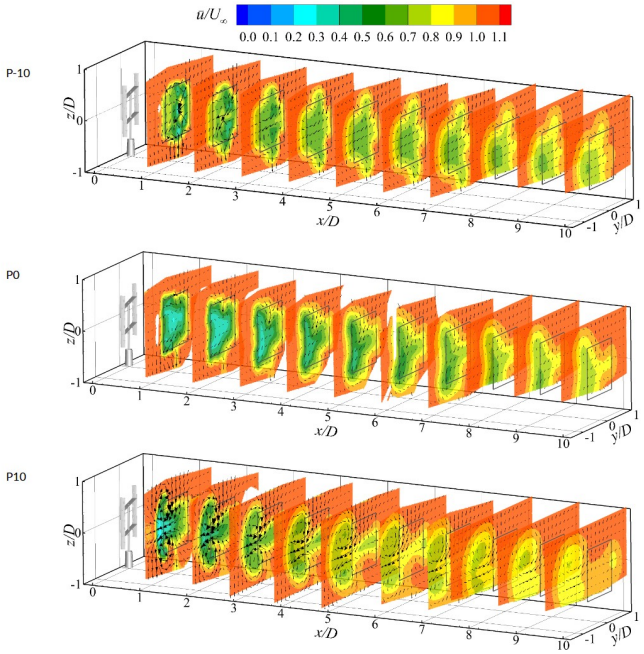

Figure 2.9: Figure adapted from Huang et al. [28] showing the normalised stream-wise velocity at multiple downstream locations for three different blade pitch angles ($\theta = -10°, 0°, 10°$) for a clockwise rotating VAWT.

In the work of LeBlanc and Ferreira [36], who performed experimental research on the thrust of a 2-bladed H-type VAWT, it was shown that crossflow loading can be introduced into the flow by pitching the blades of the VAWT. In a later work of Jadeja [30], the effect this has on the trajectory of the wake of the turbine was studied numerically. Here it was indeed shown that pitching the blades introduces a lateral loading, in turn, promoting deflection of the wake. This behaviour of the wake has been confirmed in the work of Huang et al. [28], where the effect of pitched blades on the wake was studied through stereo-PIV. Results, see Figure 2.9, show experimentally how pitched blades affect the shape and trajectory of the wake, but also the effect of pitched blades on the power production of the turbine. From these works, one can come to a consensus that by pitching the VAWT blades not only cross-flow loading is introduced into the flow, but also the strength of the blade tip vortices is enhanced, both aiding the process of wake deflection and recovery.

2.3. Multi-Rotor Systems

While the preceding sections explored familiar concepts in the wind energy sector, this section ventures into uncharted territory — the Multi-Rotor System, also known as the Multi-Rotor Wind Turbine. Illustrated in Figure 2.10, this concept differs from traditional designs by featuring multiple smaller rotors on a single support frame for power generation. Despite its lesser-known status, the multi-rotor system concept has a longstanding history. The first concepts date back to the 1930s, when Hermann Honnef presented his vision on how large-scale systems could be employed to harvest the power from the wind [33]. In the 1970s Heronemus identified that the concept of a multi-rotor system could bring the benefit of standardising rotor and drive train components, showing the potential for large unit capacity. Nowadays the MRS is increasingly being considered, primarily because upscaling of existing single-rotor turbines at a given technology level always results in an unfavourable weight and cost increase as outlined in the work of Sieros et al. [57]. The most relevant research in the realm of the MRS will be presented in the following subsections.

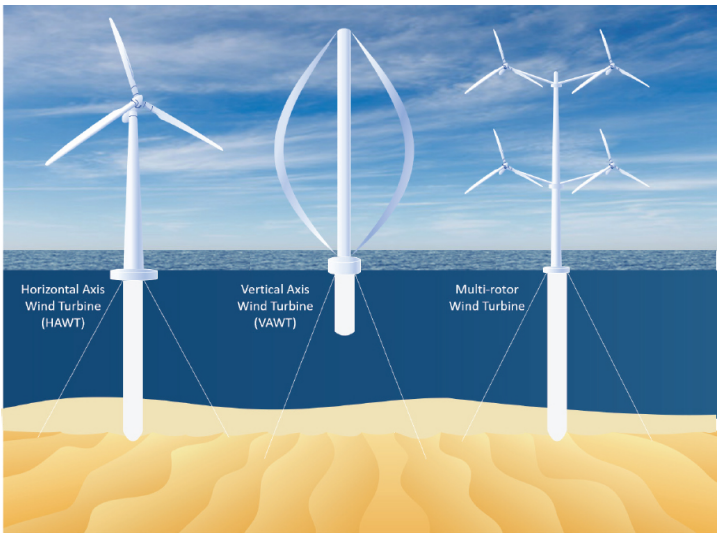

Figure 2.10: Visualization of the turbine types discussed in this work. (Figure adapted from Sandia National Laboratories [45])

2.3.1. Scaling Economics

One of the primary advantages the MRS concept brings comes from the theory of scaling economics. In the book on Innovation in Wind Turbine Design [31], Jamieson delves into this concept of scalability. Jamieson asserts that employing multiple rotors in wind turbine design leads to a more cost-effective solution compared to a single large rotor. The energy capture of a wind turbine is directly related to the rotor's swept area, while for simplicity its cost is linked to the mass of the system. As shown in Figure 2.11, increasing the rotor diameter for enhanced energy capture results in a cubic scaling of blade mass, which directly impacts cost in a similar manner. This behaviour is not only found for the blade mass, but similar trends are presented for the mass of other components such as the shaft and the tower.

Jamieson summarises this relationship with the following expression: For an MRS comprising n rotors, compared to a single large rotor of equivalent capacity, the ratio of total mass and cost of the MRS rotors and drivetrain to that of the single large rotor scales inversely with $1/\sqrt{n}$. It is essential to consider potential additional costs, such as those arising from the need for a different support structure or yawing system. However, Jamieson argues that the cost savings achieved by employing multiple smaller rotors more than offset these additional expenses. Moreover, factoring in the concept of economies of scale, which states that as production volume increases production cost per unit decreases, a further decrease in cost could be realized. This in particular given the fact the MRS consists of a large number of identical parts, such as rotor blades and generators, enabling streamlined production and efficient resource utilization through component standardization.

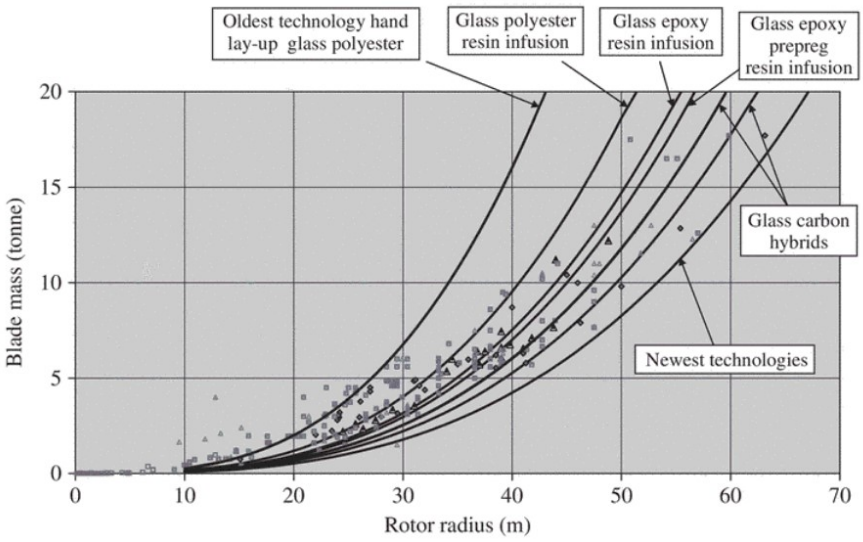

Figure 2.11: Relation between rotor radius and blade mass as presented by Jamieson [31].

2.3.2. From Isolated Turbine to MRS

An important aspect of the MRS is that multiple rotors operate in very close proximity to each other. The following subsection aims to provide insights into the existing literature on closely spaced turbines, and how this spacing affects their performance. In the work of McTavish et al. [42], who investigated experimentally the effect of turbine spacing on their performance, it was found that having multiple turbines in close proximity of each other a certain blockage effect is induced in the flow. As a result, this blockage effect results in higher flow velocities through the rotor discs, increasing the power generation compared to that of an isolated turbine. This effect in particular was observed at turbine spacings between 0.25 and 0.5 rotor diameters, resulting in power gains up to 17%. Additionally, Strickland and Stevens [62] showed similar results employing an LES study, where it was also found that this blockage effect is affected by the thrust coefficient of the rotors.

Where the two aforementioned studies have focussed on the effect of closely spaced HAWTs, similar research has been performed on their vertical axis counterpart. Zanforlin and Nishino [74] conducted a 2-dimensional unsteady Reynolds-averaged Navier-Stoker (RANS) simulation on a pair of counter-rotating VAWTs, studying the effects of gap size, TSR, and wind direction on the performance of the pair. They reported an increase in power output for decreasing gap size, similar to what was found in the case of the HAWT. Additionally, they attributed this effect to two main flow mechanisms:

- Due to the presence of the neighbouring turbine, an increase in lateral velocity was found in the upwind path of the blades. As a result, the direction of local flow is more favourable for generating lift, and thus torque, in this section of the VAWT.
- Due to the presence of the neighbouring turbine the wake is contracted, making a larger momentum flux available for power generation in the downwind part of the turbine.

Moreover, De Tavernier et al. [63], who conducted another numerical study on a pair of vertical axis machines, identified that the rotational direction of the pair influences their power generation. In their work, the largest gain in power output was found for a counter-rotating configuration. In particular, a configuration where the inner blades move in the opposite direction of the flow yields the best performance. Furthermore, De Tavernier et al. show that having the two VAWTs as close as possible together yields the best performance. In the work of Vergaerde et al. [67] an experimental study was performed on a pair of closely spaced VAWTs. Results of this study showed an increase in the power production of up to 16% compared to the power production of two individual VAWTs. Besides, Vergaerde et al. made an interesting observation regarding the power curve, which appeared to flatten as a result of the mutual interaction between the VAWT pair. This stable interaction between the two turbines ensures the pair can produce near-optimum power over a larger range of TSRs. Additionally, it was reaffirmed that the most effective rotational configuration for a pair of VAWTs involves counter-rotating rotors, where the inner blades rotate opposite to the flow direction, a result consistent with the findings in the work of De Tavernier et al.

2.3.3. Multi-Rotor System Concepts

In the previous subsections, two key benefits of the MRS concept have been discussed. The first pertains to scaling, which results in reduced weight and cost compared to individual large wind turbines. The second benefit involves the potential for increased power performance due to a blockage effect caused by closely spaced rotors. The current subsection dives further into the concept of the MRS, presenting existing research on this concept.

Next to the chapter on the Multi-Rotor System in the book of Jamieson [31], which provides a good insight into the system as a whole and the potential benefits it brings, several other studies have been performed. McMorland et al. [41] for example have discussed the operational benefits the MRS brings. They argue that having a single large system comprising multiple smaller rotor-nacelle assemblies (RNAs) allows for alternative maintenance strategies. As the full MRS comprises multiple RNAs, the system as a whole can still operate if one or a few RNAs break down, particularly if the system consists of a large number of RNAs. Additionally, it also allows for a reduced inventory, as one can repair and replace RNAs and cycle through them. In the work of Jamieson et al., as part of the Innwind.EU project [33], a preliminary design of a HAWT-based, 45-rotor, 20MW system has been presented. In terms of performance and aerodynamics, an increase in power production of 8% was found when compared to 45 individual 444kW isolated turbines, along with a decrease in total weight and cost of rotor-nacelle assemblies. This collective improvement is expected to result in a reduction in the levelized cost of energy of 15% and a reduction of 13% in capital expenditure when compared to the single-rotor reference turbine used during the study.
The work of Ghaisas et al. [23] and Bastankhah and Akbar [6] both evaluated the wake of a HAWT-based MRS through LES studies. These works show similar results for the behaviour of the wakes, where individual wake profiles are recognised behind each rotor of the MRS. The wakes of the individual rotors start to interact with each other as they travel downstream, over time merging into a single wake region. In both works the conclusion is drawn that the wake of the MRS recovers faster than that of a single-rotor reference turbine. Moreover, Bastankhah and Akbar's research emphasizes the beneficial impact of increased spacing between individual rotors on wake recovery, with the most substantial advantages of enhanced wake recovery occurring in the region where the individual wakes have not yet merged into a single wake region. Bastankhah and Akbar's study also suggests that the rotational direction of the rotors exerts minimal influence on wake recovery. Additionally, the work of Hebbar et al. [26], where a high-fidelity LES study was performed on the wake of the MRS, strengthens these findings. Here once more a faster recovery was found, this time in combination with a higher degree of uniformity and reduced peaks in the wake deficit compared to a single-rotor reference turbine. Furthermore, the experimental study of Xiong et al. [73] shed more light on the process of wake recovery, and how this process is affected by the presence of gaps between the rotors. Here, Xiong et al. showed that during wake recovery, the individual rotor wakes moved towards each other as they merged into a single wake region. In addition, the effect of yaw on the trajectory of the wake was assessed, where it was presented that the yawed MRS induces a stronger deflection on the wake than a single-rotor turbine.
Special attention should go to the publication of Van der Laan et al. [35], which holds a prominent position in this relatively uncharted territory. This is because it delves into the performance of the MRS

through an on-site field study of a prototype. The work includes a comprehensive comparison between numerical simulations of the Vestas 4R-V29 MRS demonstrator, Figure 2.12, and field measurements of the same prototype, covering aspects of power performance and wake LiDAR data. Results have shown an enhanced power performance between 0% and 2% depending on the weather conditions, with an increase in power performance of 1.8% below rated wind speed, resulting in a 1.5% annual energy production increase. Moreover, the LiDAR measurements showed similar wake characteristics as presented in the literature, and RANS simulations once again showed an enhanced wake recovery.

Figure 2.12: Picture of the Vestas 4R-V29 demonstrator.[2]

The studies outlined earlier in this subsection all focussed on the HAWT-based multi-rotor system. This report, however, revolves around its VAWT-based sibling, visualised in Figure 2.13, a concept which is still relatively unexplored. In his book on innovative turbine design, Jamieson [31] does however touch upon some benefits the VAWT-based MRS concept could bring. Compared to isolated HAWTs, isolated VAWTs have lower aerodynamic efficiency and a higher torque, which in turn results in higher costs. Jamieson states however that when used in a Multi-Rotor configuration, the VAWT design could overcome these flaws. The torque penalty of the VAWT could be resolved by increasing the ratio of blade length over rotor diameter. Usually, this would result in a tall and slender structure which is not rigid. By suspending this VAWT in a frame, for example, as it would be in a Multi-Rotor Configuration, additional support could be provided, overcoming this disadvantage. Additionally, a VAWT might integrate better into a rectangular structure due to its shape, plus it is less sensitive to yaw errors. Moreover, in Jamieson et al. [32] a preliminary design for a VAWT-based MRS comprising 2-bladed H-type rotors is presented. The main conclusions to take away from this publication are that its performance would match, or perhaps even exceed that of a HAWT-based MRS. Furthermore, standardisation of the RNA can offer benefits in overall production cost, and it is likely additional benefits will be found regarding operations and maintenance due to VAWTs having fewer and simpler components than HAWTs.

[2] https://en.wind-turbine-models.com/turbines/1459-vestas-multi-rotor-concept

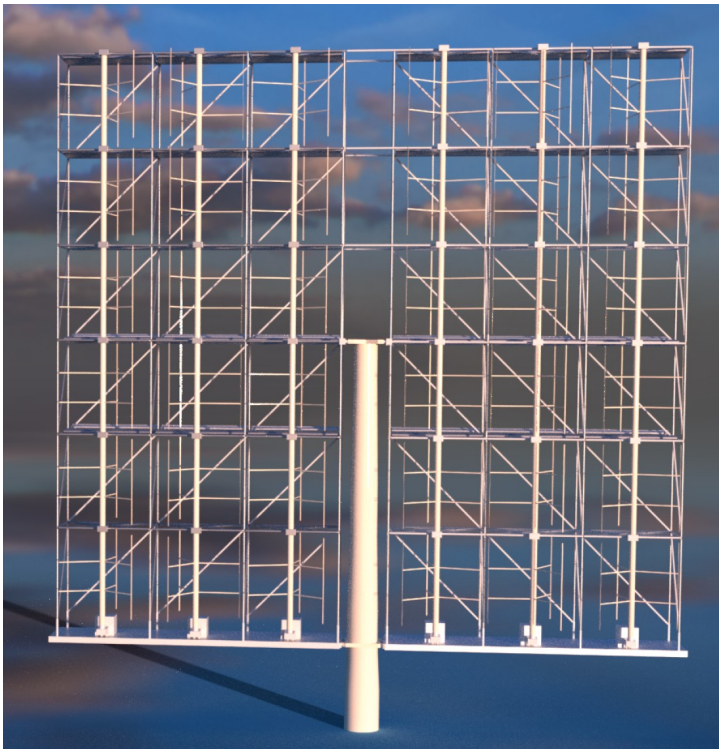

Figure 2.13: Render of the VAWT-based MRS concept. Figure adapted from Distelbrink et al. [19].

2.4. High Lift Aerodynamics

In section 2.1, the concept of the ABL was presented, where it was identified that more wind power is available higher up in the atmosphere due to larger flow velocities. In addition, different wake deflection and re-energisation techniques of wind energy systems were presented, which is an important aspect of wind farm design as it allows downstream turbines to operate in a cleaner flow, resulting in a larger power yield. Both this wake deflection and re-energisation of the wake rely on the concept of cross-flow loading and the introduction of large-scale structures in the flow. Additionally, it was identified that by introducing cross-flow loading and large-scale structures, for example through high-lift wings, there exists the potential of transporting power available in the higher regions of the atmosphere to the lower regions. This section delves into the concept of high-lift wings, how this high-lift can be achieved, and how their induced upwash and tip-vortices relate to the lift they generate.

As a wing generates lift, a pressure difference is found between the suction and the pressure side of the wing. The net difference between these pressures induces the lifting force. However, as air tends to flow from high to low pressure regions, due to this pressure imbalance the flow near the tips tends to curl from the high to the low pressure region. This phenomenon introduces a circular motion into the flow that trails downstream. This is known as the trailing tip vortex. These trailing vortices, in combination with the bound vortex of the wing, induce a velocity component in the flow downstream of the wing. This induced velocity is known as the 'downwash' in the context of upward lifting wings. The strength of these vortices and the induced velocity component are related to the lift of the wing according to Prandtl's Lifting Line theory.

2.4.1. Prandtl's Lifting Line Theory

The following paragraphs will introduce the reader to Prandtl's Lifting Line theory. The information presented in this section has been summarised from the book of Anderson on the Fundamentals of Aerodynamics [4], which provides a clear explanation of the theory. Before Prandtl's theory can be discussed it is important to touch upon some fundamental aerodynamic principles, namely the *vortex filament* and the *Biot-Savart Law*.

The concept of the vortex filament extends the idea of a point vortex. Imagine a straight line extending infinitely in both directions, known as the vortex filament, with a strength Γ. At any arbitrary point along the filament, if one considers a plane perpendicular to the line, the vortex filament induces a flow identical to that of a point vortex with the same strength Γ. Expanding on this concept, a vortex filament with a strength Γ, equivalent to the circulation about any closed path surrounding the filament, need not be straight but can possess any arbitrary shape. Regardless of its shape, this filament still induces a velocity on the surrounding flow. The induced velocity at an arbitrary point P, which is located at a distance $\bar{r}$ from the segment of the vortex filament $d\bar{l}$ is defined by the Biot-Savart law, Equation 2.17.

$$d\bar{V} = \frac{\Gamma}{4\pi} \frac{d\bar{l} \times \bar{r}}{\mid \bar{r}^3 \mid} \tag{2.17}$$

To expand on this, Hermann von Helmholtz was one of the first to use the aforementioned vortex filament concept in his analysis of inviscid and incompressible flow. While using this theory, he established some basic principles describing vortex behaviour, nowadays known as Helmholtz's vortex theorems:

1. The strength Γ of a vortex filament is constant along its length.
2. A vortex filament cannot end in a fluid; it must extend to the boundaries of the fluid or form a closed loop.

These theorems are fundamental to Prandtl's Lifting Line theory, a concept developed by Ludwig Prandtl, which in the context of this work will be used to understand the relation between the lift of the wing and the induced velocity of its tip vortices. Prandtl reasoned the following: Consider a vortex filament with a circulation strength Γ that is bound in space. This filament, which contrary to a free vortex does not move with the fluid elements flowing around it, experiences a lift force $L' = \rho_\infty V_\infty \Gamma$ according to the Kutta-Joukowski theorem. Here L' is the section-wise lift force, and ρ_∞ and V_∞ are the freestream properties. As this vortex filament is bound, it can be replaced by a finite wing with span b. Due to Helmholtz theorem however, this bound vortex cannot end in the fluid, thus at the boundaries of the wing at the wing tips the filament must continue as two free vortex filaments trailing downstream to infinity. This bound vortex plus the two free trailing vortices is known as the horseshoe vortex and is represented in Figure 2.14.

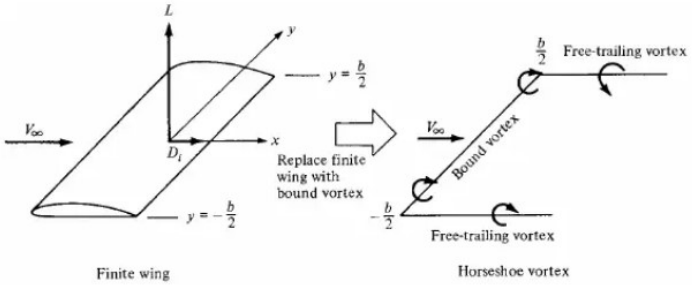

Figure 2.14: Representation of the conversion from the finite wing to the bound vortex. Graphic originates from Anderson [4].

The induced downwash velocity w by the trailing tip vortices at a given y location along the bound vortex filament, considering $y = 0$ is the centre of the wing, is given by Equation 2.18. This theory however is not complete, as one might notice Equation 2.18 tends towards $-\infty$ as y approaches the wingtips ($\pm b/2$), and therefore does not accurately represent the case of a finite wing.

$$w(y) = -\frac{\Gamma}{4\pi} \frac{b}{(b/2)^2 - y^2} \tag{2.18}$$

To resolve this singularity, Prandtl decided to instead of replacing the 'lifting line' of a wing with a single horseshoe vortex, replace it with multiple superimposed horseshoe vortices as represented in Figure 2.15. By doing so a more detailed lift distribution could be simulated, and instead of having only two trailing vortex filaments there now is a sheet of trailing vortices. The strength of each individual

trailing vortex is equal to the change in circulation along the lifting line. The total downwash induced at the centre of the wing y_0 by the full vortex sheet is given by Equation 2.19. From this point onwards Prandtl's theory extends on how this downwash influences the induced angle of attack of the finite wing, and the effect this has on the induced drag. This, however, is not of interest to the current research. Equation 2.19 shows that the downwash induced by the finite wing is driven by the circulation around the wing. Thus, to increase the downwash component, one should aim at increasing the circulation strength Γ.

$$w(y_0) = -\frac{1}{4\pi}\int_{-b/2}^{b/2}\frac{(d\Gamma/dy)}{y_0 - y}dy \tag{2.19}$$

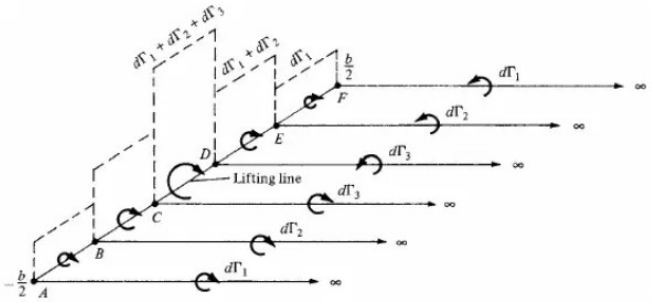

Figure 2.15: Superposition of multiple horseshoe vortices along the lifting line. Graphic adapted from [4].

Induced Downwash Behind the Wing

Equation 2.19 does not tell the full story of the downwash behind a wing. In fact, this equation only gives the downwash induced by the tip vortices trailing the lifting line of the wing. The following paragraph aims to give insight into the total induced upwash at a given point P behind a finite wing, represented by bound vortex AB and the subsequent horseshoe vortex. First, it is important to identify the induced velocity at point P of the isolated bound vortex AB of length L with circulation Γ. For this analysis bound vortex AB is visualised in Figure 2.16a. The total induced velocity at point P, which is located at a perpendicular distance h from AB is given by Equation 2.20. Here θ_A and θ_B are related to the position of point P with respect to the bound vortex.

$$V_{P,AB} = \frac{\Gamma}{4\pi h}(\cos\theta_A - \cos\theta_B) \tag{2.20}$$

As mentioned in the paragraphs before, the trailing vortices also contribute to the upwash induced by the wing. These trailing vortices, which originate from both points A and B, are considered semi-infinite filaments. Considering again Figure 2.16a and Equation 2.20, but now point B approaches ∞, this results in $\theta_B \to \pi$, and the induced velocity originally represented by Equation 2.20 is now given by Equation 2.21.

$$V_{P,A\to\infty} = \frac{\Gamma}{4\pi h}(\cos\theta_A + 1) \tag{2.21}$$

This now gives all the tools to determine the induced velocity V at a given point P, behind the horseshoe vortex originating from finite wing AB. This horseshoe vortex, which consists of lifting line AB, and trailing vortices $A \to \infty$ and $B \to \infty$ has been visualised in Figure 2.16b. The velocity $V_{P,\text{horseshoe}}$, induced at P is given by Equation 2.22. In this equation, the first term represents the contribution of the bound vortex AB, with h_1 being the distance between the bound vortex and point P, the second term represents the contribution of the trailing vortex of point B, and the third term represents the contribution of the trailing vortex of point A. For the contribution of the trailing vortices distances h_2 and h_3 are related to each other as $b = h_2 + h_3$.

$$V_{P,\text{horseshoe}} = \underbrace{\frac{\Gamma}{4\pi h_1}(\cos\theta_{A1} - \cos\theta_{B1})}_{\text{bound vortex AB}} + \underbrace{\frac{\Gamma}{4\pi h_2}(\cos\theta_{B2} + 1)}_{\text{trailing vortex B}} + \underbrace{\frac{\Gamma}{4\pi h_3}(\cos\theta_{A3} + 1)}_{\text{trailing vortex A}} \tag{2.22}$$

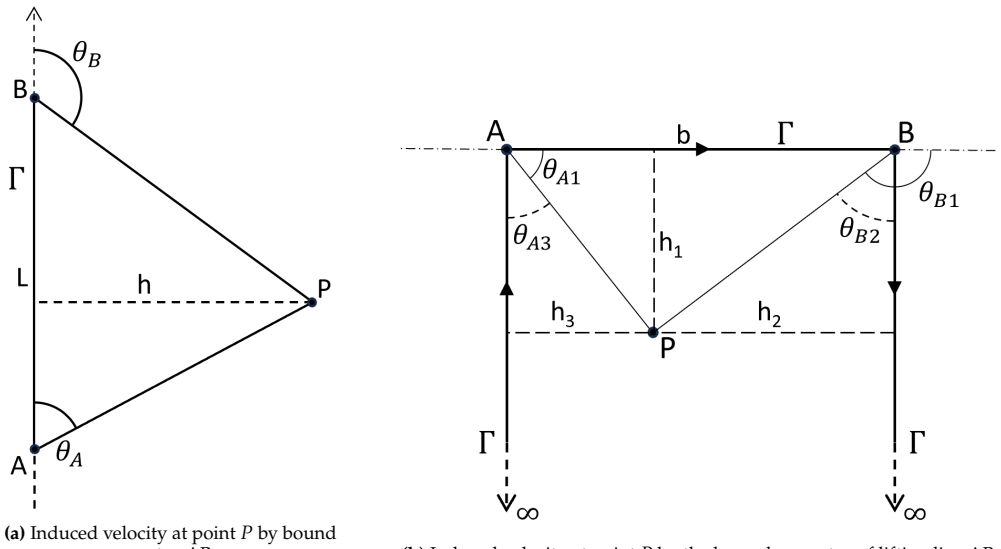

(a) Induced velocity at point P by bound vortex AB

(b) Induced velocity at point P by the horseshoe vortex of lifting line AB

Figure 2.16: Schematic of bound vortex AB (left), and horseshoe vortex originating from lifting line AB (right).

2.4.2. Multi-Element Wings

From the previous section, it became evident that the strength of the induced downwash is related to the circulation strength Γ. In addition, it was noted that the Kutta-Joukowsky theorem links the section-wise lift of the wing to the circulation strength, as once again represented in Equation 2.23. From this same equation it can be observed that to increase the lift, and thus circulation Γ, one can either increase the surface area by increasing the section-wise chord length c or increase the lift coefficient c_l by adjusting the airfoil design of the wing.

$$L' = \rho_\infty V_\infty \Gamma = c_l q_\infty c \tag{2.23}$$

This section focuses on how to increase the lift coefficient by introducing the so-called multi-element wing. The information presented in this section is primarily taken from the paper of Smith [58], which is seen as one of the most relevant papers when it comes to high-lift wings. In this paper, Smith starts by presenting some theoretical limits regarding the lift coefficient, after which he dives into some limiting factors. In short, to increase the lift over an airfoil one needs to increase the velocity of the flow over its top surface. However, as the flow travels over the surface it slows down due to friction, resulting in it experiencing an adverse pressure gradient. To get more lift, one needs to speed up the flow even further, which in parallel also results in an increased adverse pressure gradient. At some point, this adverse pressure gradient becomes too large, and the flow separates from the surface, resulting in a loss of lift instead of the expected gain. To still be able to achieve this high lift, this separation must be prevented by adjusting the geometry of the airfoil. That is where the multi-element wing comes into play.

In his paper, Smith later elaborates on 5 primary beneficial effects multi-element wings have in achieving higher lift. These effects he calls the *slat effect*, *circulation effect*, *dumping effect*, *off-the-surface pressure recovery effect*, and the *fresh boundary layer effect*. A brief explanation of each of these effects is presented below:

- *Slat effect:* The first effect is the so-called slat effect. Consider a slat element located in front of a main element. As the slat element generates a lifting force it has a circulation. This circulation induces a velocity on the main element, reducing the flow velocities over the surface of this downstream element, resulting in reduced pressure peaks, and thus reducing the adverse pressure gradient the flow encounters over this element, delaying separation.
- *Circulation effect:* The slat effect goes hand-in-hand with the circulation effect. As the upstream element affects the flow over the downstream element, so does the downstream element affect the

flow over the upstream element. The circulation over the downstream element increases the flow velocity over the upstream element, in particular the rear half of this element, thus increasing its circulation.

- *Dumping effect:* The dumping effect is another way a trailing element can affect the flow over a leading element. Consider again two elements closely spaced together, with the trailing edge of the upstream element close to the leading edge of the downstream element. Around the leading edge of the trailing element, there exists a low-pressure, high-velocity flow region. Having this low-pressure region close to the upstream element, this region alleviates the adverse pressure gradient the flow encounters over the upstream element, pulling the low energy boundary layer flow at the trailing edge of the upstream element towards it, preventing separation problems.
- *Off-the-surface pressure recovery:* The fourth effect is the so-called off-the-surface pressure recovery effect. As air flows over a lifting element, its velocity increases until it reaches the point of minimum pressure, after which it decelerates again back to free-stream velocity. Once the flow reaches the trailing edge of the element it has often not yet returned to free-stream conditions. This recovery continues after the flow leaves the element. This recovery however is much more efficient when the flow is not in contact with any walls, and thus is it beneficial to introduce gaps so that the flow can recover 'off-the-surface'.
- *Fresh-boundary-layer effect:* The final effect Smith describes as the fresh-boundary-layer effect, perhaps the most well-known effect of multi-element wings. As air flows over a surface the thickness of the boundary layer increases. Thicker boundary layers however are more prone to separation than thinner ones. By introducing gaps, each element starts with a fresh, thin boundary layer capable of withstanding stronger adverse pressure gradients, postponing separation.

Implementing gaps, and thus creating a multi-element airfoil design should result in higher lift coefficients as one takes benefit of the abovementioned effects. However, a question arises regarding how having multiple elements affects the lift slope of a wing. Multi-element airfoils often consist of a single main element, supported by one or multiple smaller elements located either near the leading edge (referred to as a slat) or near the trailing edge (referred to as a flap). Flaps and slats influence the lift curve ($C_L - \alpha$) differently, as illustrated in Figure 2.17. As can be seen, the leading edge slat increases the stall angle of the airfoil, in principle extending the lift curve. It does this by inducing a downwash on the main element, reducing the suction peak and thus the adverse pressure gradient the flow experiences, delaying separation. Smith described this as the *slat effect*. The flap on the other hand increases the effective camber of the airfoil, increasing the lift generated at a given angle of attack, thus shifting the $C_L - \alpha$-curve upward. Combining both flaps and slats results in both an upward shift of the lift curve and a delayed stall angle of attack, thereby extending $C_L - \alpha$ as depicted in Figure 2.17.

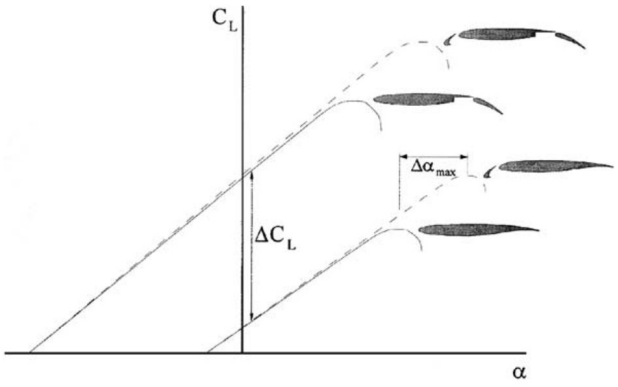

Figure 2.17: Effect of a flap and a slat on the lift curve as visualised in the work of Van Dam [66].

Examples of extreme high-lift solutions through multi-element wings can be found in the realm of airborne wind energy. Most notable is the publication of Bauer et al. [8], where they optimised a 4-element airfoil design, capable of achieving a lift coefficient above 5.0. Although this is only a single example, it still shows the capabilities of multi-element airfoils.

2.4.3. Alternative Methods to Achieve High Lift

The following section will dive into a few notable alternative methods of increasing the lift a wing can generate. One of these methods is the so-called Gurney flap. The concept of the gurney flap, as described in the work of Liebeck [38], was first used on Indianapolis racecars to increase their downforce. It is a small flap, in the order of 1% chord length, located perpendicular to the pressure side of the airfoil. How it looks, and the effect it has on the lift curve is shown in Figure 2.18.

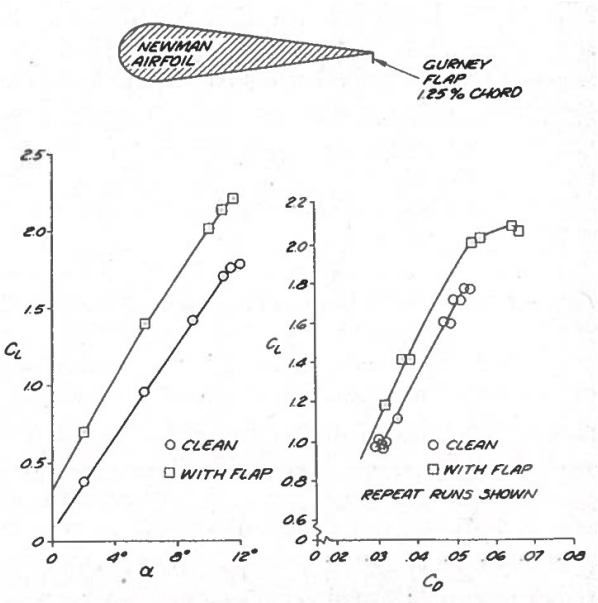

Figure 2.18: Visualisation of the Gurney flap, and its effect on the lift curve as displayed by Liebeck [38].

Another method for increasing the maximum lift of a wing is applying vortex generators. Vortex generators are widely used within the automotive sector, the aviation industry, and the wind turbine industry. The vortex generator is a small plate mounted perpendicular to the suction side of an aerodynamic body, at an angle to the incoming flow. As air flows over the surface, past the vortex generator, it induces a swirling motion into the flow, creating a vortex, which energises the boundary layer. As a result, the boundary layer is less prone to separation, increasing its maximum lift coefficient. The effect the vortex generator has on the flow over the wing section is shown in Figure 2.19. Relevant experimental studies on how the vortex generator affects the lift of an airfoil can be found in Sørensen et al. [59] and Seshagiri et al. [56].

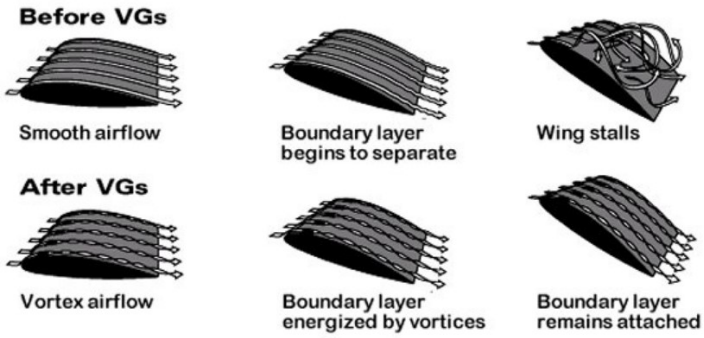

Figure 2.19: Effect of vortex generators on flow separation [53].

2.5. Experimental Techniques

As earlier presented in section 2.1 and section 2.2 multiple studies on the dynamics and interaction of wind turbine wakes have been performed in recent years. Although ideally, one would perform these studies on full-scale models to get an insight into real-world dynamics, obtaining meaningful data of sufficient quality at this scale presents significant challenges. Consequently, researchers have turned to alternative methodologies, primarily relying on a combination of numerical simulations and wind tunnel testing. These two methods often work in tandem, with wind tunnel experiments serving as a crucial component in the validation process for numerical models. Recent efforts by Zhan et al. [75] have shown the potential of full-scale wake measurement for an onshore wind farm using LiDAR. In this publication, Zhan lays out a guideline on how one should perform and analyse such LiDAR measurements. Still, wind tunnel testing offers several advantages which are listed below.

- Flow conditions are repeatable and to a certain extent controllable. As a result, large datasets over a range of flow conditions can be obtained in relatively short timeframes as one does not depend on the wind conditions, but can simply set the desired conditions.
- Several experimental techniques are available for performing detailed flow measurements. These methods include pressure measurements, hot-wire anemometry, Laser Dopler Velocimetry, and Particle Tracking Velocimetry. Measurement resolutions available in the wind tunnel are impossible to achieve at full scale.
- Wind tunnel models can be designed to accommodate geometric changes. Furthermore, when studying the wake dynamics of wind farms one can easily test different layouts.
- The cost of developing and producing a wind tunnel model is much lower than the development and production cost of a full-scale model.

This chapter will not only introduce the reader to the experimental techniques used during this thesis but also provide some insight into the development of a scaled-down wind tunnel model. subsection 2.5.1 dives into the effects of scaling, and which design parameters are driving for replicating the full-scale effects in a scaled-down wind tunnel environment. This is then followed by a section on load measurements in subsection 2.5.2, and this section is concluded by a short introduction to Particle Tracking Velocimetry in subsection 2.5.3.

2.5.1. Design of Experiments

When designing a wind tunnel model it must be scaled accordingly so that the correct flow phenomenons are captured during the experiment. As it is often difficult to match the forces and moments of real-world models, during the design researchers aim to match non-dimensionalized parameters such as force coefficients. By doing so it is assumed the flow in the wind tunnel behaves similar to what it would do in the real world. This is often achieved by applying Buckingham's Π theorem. Buckingham's Π-theorem, formulated by Edgar Buckingham in 1914 [13], states that a scaled-down model behaves similarly to its full-scale counterpart if all relevant non-dimensionalised variables are matched. It is however not always possible to match every dimensionless parameter between the full-scale and scaled system. Therefore it is important to think about which flow effects or performance characteristics are to be captured during the scaled-down experiment, and which parameters must be matched to achieve this.

Scaling of Wind Turbine Models

In the papers of Canet et al. [15] and Wang et al. [70] a review is performed on which parameters are most critical to be matched during the design of a scaled-down wind turbine model. Here Canet et al. have formulated laws on how to scale a horizontal axis wind turbine, and which characteristics of the turbine rotor can be matched faithfully. As a result, two methods are presented on how one should scale a wind turbine model. In the paper, the performance of a 10MW full-scale turbine is compared to three scaled-down models of different scaling factors. Key points to take away from this paper are that the vortex shedding of the blades is associated with the Strouhal number, of which the latter is always matched when the TSR is matched between the full-scale and wind tunnel model. This implies that the wake behaviour, which is driven by the vortex shedding of the blades can be matched by matching the TSR between the scaled-down and real-world model. Canet et al. assert that even when it is challenging to match all relevant parameters, such as the chord-based Reynolds number, which could lead to a

mismatch in rotor loading, a scaled-down model can accurately replicate the performance of a full-scale model. In cases where an exact match is not feasible, the scaled-down model still captures relevant trends.
Wang et al. on the other hand have investigated to which extent wind tunnel experiments can match the physical characteristics of a full-scale horizontal-axis wind turbine wake. During this research, a hybrid experimental-simulation approach was taken, where the full-scale model was represented by a Large Eddy Simulation - Actuator Line Method (LES-ALM) code due to the lack of available data on full-scale wind turbine wakes. Although the code was validated, it still brought some uncertainty to the table. In particular, the uncertainty that perhaps not all physical processes at blade level or within the wake are modelled. With this in mind, they have found that by matching the TSR, non-dimensional circulation around the blade, and wake velocity deficit, of which the latter is matched by closely matching C_T, the far wake of the turbine (4D away from the rotor plane) can accurately be matched. In addition, the near wake was also found to be relatively similar, where only a mismatch between the cores of the wakes was found, primarily due to scaling limitations for the nacelle design of the scaled model. Although this slight mismatch was found, it did not seem to affect the overall wake shape and behaviour.
From the above-mentioned studies, it becomes evident that wake behaviour is driven by the vortex shedding of the blades, which in turn can be matched by matching the TSR. It is however important to point out that these studies have focussed on the scaling of HAWTs, and no research on VAWTs has been presented.

2.5.2. Load Measurements

As mentioned in section 2.2 the thrust T a turbine exerts on the flow is an important parameter regarding its overall performance. This thrust, which usually is non-dimensionalized to the thrust coefficient C_T, can be measured in the wind tunnel using a force balance. Modern balances make use of load cells consisting of strain gauges. These strain gauges are often placed in a Wheatstone Bridge setup, arranged in alternating tension and compression format [60], although they can also be used independently.
Strain gauges function according to the principle of linear elasticity, which dictates that a given material undergoes a predictable change in electrical resistance when subjected to a given deformation. When an external force is applied to the strain gauge or load cell it will result in a deformation, resulting in a change in electrical resistance. Although often small, this change in resistance can be detected and accurately quantified. According to Hooke's law, there is a linear relationship between the stress (σ) and strain (ε) experienced by a material, as expressed in Equation 2.24. In this equation, E represents the modulus of elasticity. Consequently, the deformation registered by the strain gauges can be directly related to the applied stress, facilitating the conversion of deformation into a quantifiable load measurement.

$$\sigma = E \cdot \varepsilon \tag{2.24}$$

Often multiple load cells are integrated in a single force balance. This configuration permits the creation of a six-component balance, capable of measuring forces in, and moments around all three spatial directions: x, y, and z. Such a balance enables comprehensive characterization of forces and moments acting on the model during wind tunnel testing. In addition to these load cells, such a force balance is often equipped with a temperature sensor, as any fluctuation in temperature affects the mechanical properties and thus electrical resistance of the strain gauges. By having a temperature sensor these fluctuations in temperature and thus electrical resistance can be quantified, and corrected accordingly.

2.5.3. Particle Image/Tracking Velocimetry

One of the techniques used a lot nowadays to acquire information on flowfields is Particle Image Velocimetry (PIV) or Particle Tracking Velocimetry (PTV). PIV is a non-intrusive method, capable of acquiring velocity data on a large region within the flow at a time, and has been used in for example the work of Huang et al. [28] and Tescione et al. [64]. Similarly to Laser Doppler Velocimetry, this technique traces particles that have been submerged into the flow, with the main difference being that PTV is capable of instantly measuring an entire velocity field or volume instead of a single point. The work of Scarano [49] provides a good review on the topic of PIV, however, the main principles are covered in this section.

A PIV system consists of a seeding system which seeds the flow with tracer particles, an illumination system illuminating the particles at the measurement location of interest, and a recording system consisting of one or more high-speed cameras. There are three main types of PIV, each of which yields a different output and requires a different setup:

- **Planar PIV:** Requires a single camera orthogonal to the laser sheet. Capable of measuring 2 velocity components in a 2D domain.
- **Stereoscopic PIV:** Requires 2 cameras. The system is capable of measuring 3 velocity components in a 2D domain.
- **Tomographic PIV:** Requires 3 or more cameras. The Tomographic PIV system can reconstruct the measurement volume and measures 3 velocity components in a 3D domain.

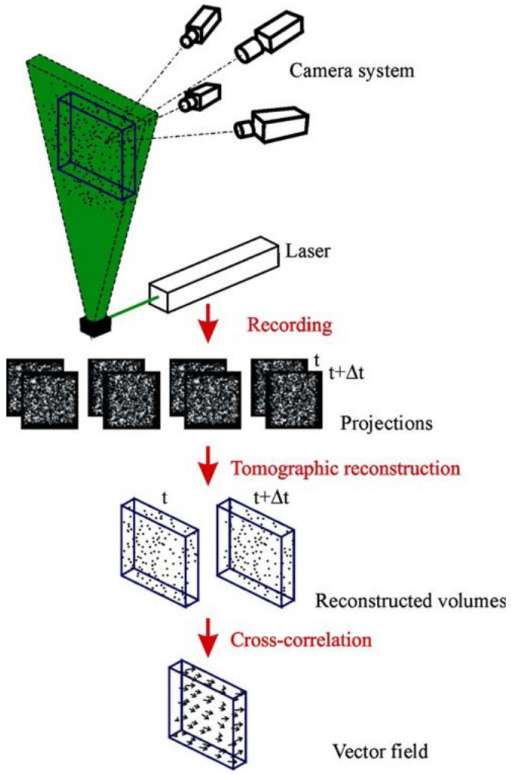

Figure 2.20: Graphical representation of the principle of tomographic PIV. (reproduced from Elsinga et al. [20])

Figure 2.20 gives a graphical representation of the working principle behind the tomographic PIV system, which is the type used during this thesis. As mentioned, the PIV system relies on the tracking of particles within the measurement volume. A seeding system seeds the flow with naturally buoyant particles which scatter light when illuminated, and should not perturb the flow. For large-scale experiments such as the one considered in this thesis, often Helium-Filled Soap Bubbles (HFSB) are used. More information on HFSB and its application and working principles can be found in the doctoral thesis of Caridi [16].
At the location of interest, these particles are illuminated by a high-energy light source. For this often a laser sheet is used, which is formed by deforming a laser beam to a thick sheet through a set of optics. As a result, the particles that are within the measurement volume are illuminated and scatter light to their surroundings. A high-speed camera system consisting of 3 or more cameras, focused on the measurement volume, takes a large number of images from different angles with a short time interval between each set of images. By processing this set of images, and tracking the displacement of particles between each image, the velocity field within the measurement volume can be reconstructed.

It is important to note that there is a difference between PIV and PTV. In PIV the obtained results are based on the displacement of groups of particles, whereas PTV tracks the motion of individual particles. More information on the reconstruction algorithm of PIV, which relies on the concept of cross-correlation, can be found in the work of Elsinga et al. [20]. The algorithm used for the reconstruction of PTV measurements is a Lagrangian tracking method called Shake-The-Box (STB). More information on the STB algorithm, which relies on time-resolved information to predict the position of particles, can be found in the work of Schanz et al. [50].

2.6. Research Objective

In the journey through the preceding sections of this introductory chapter, we have delved into the complex world of wind energy and high-lift systems. This section will summarise the key takeaways from the provided synthesis of the literature, after which it will nicely flow into a research objective for the master thesis project. To support this research objective several research questions will be posed at the end of this section. The main findings of this section are as follows:

- From the review of the ABL it became evident that due to the shear layer near the surface of the Earth, wind velocities and thus wind power available for turbines to extract, are larger higher up in the atmosphere.
- Numerous studies have investigated the optimisation of wind farm yield by studying the mechanics behind wake steering and wake re-energisation. There appears to be a general understanding that the wake of a wind turbine can be deflected by imposing a lateral force on the flow, which for HAWTs is achieved by tilting the rotor disc and for VAWTs by pitching the blades. Additionally, the work of Verhulst and Meneveau [69] showed that a similar effect could be achieved through external lift-generating devices.
- Over the past few years there has been renewed interest in Vertical-Axis Wind Turbines due to their mechanical layout, but also due to their potential to yield higher power densities in wind farm configurations.
- The Multi-Rotor System is shown to be an interesting alternative to the conventional single-rotor turbine. Due to its layout with a large number of small rotors, it brings the benefit of scaling and the potential for new maintenance strategies, resulting in a reduction in weight and production and maintenance costs. Moreover, the MRS is expected to bring comparable, or perhaps even enhanced performance thanks to its closely spaced rotors which due to a blockage effect are capable of capturing more wind energy. One of the challenges the MRS brings is its large support structure, however, this support frame does provide the opportunity to house external devices for wake deflection and re-energisation.
- Several studies on the HAWT-based MRS have been discussed in the chapter on wind energy, but very little information on the VAWT-based system was available and therefore not presented. The studies on the VAWT-based MRS that have been discussed were all numerical and analytical, with none of them being of an experimental nature.
- In the chapter on high lift it was pointed out that lift-generating wings induce vortical structures into the flow as described by Prandtl's Lifting Line Theory. Additionally, the concept of vortex generators was touched upon, which are small aerodynamic devices that induce vortical structures into the flow to energise the boundary layer.

These findings open an interesting avenue when it comes to this master thesis research work. Firstly, as little research exists on the wake dynamics of a VAWT-based MRS system, this master thesis will aim to investigate the near-wake dynamics of such a system by means of an experimental investigation. Secondly, combining the findings on the ABL, the effect of lift-generating devices on wake steering, and the concept of vortex generators, one can make an interesting conceptual reasoning. From a conceptual point of view, it would be interesting to identify the possibilities of enhancing the mixing of the ABL, increasing wind speed closer to the surface of the Earth (thus increasing available wind power), by introducing large-scale vortices into the flow similar to how a vortex generator energises a boundary layer. These large-scale vortical structures could be introduced into the flow by having high-lift wings submerged in the ABL. This is the point where the MRS comes into play again, as its large support structure could function as a mounting point for these lift-generating wings. These lift-generating wings will then not only induce large-scale vortices into the flow but will also assist in deflecting the wake

away from any subsequent turbines when the MRS is placed in a wind farm configuration as a result of the induced upwash. By taking this approach, wake deflection and recovery do not rely anymore on the vorticity induced by the individual VAWT rotors, but are now decoupled from the VAWT rotors and driven by the tip-vortices and upwash induced by the external wings. This allows the rotors to operate under more optimal conditions, in theory resulting in a smaller performance hit. Therefore, the second research objective of the master's thesis work will be to present a proof-of-concept on how having external lift-generating devices mounted on the MRS will affect the behaviour of the near-wake. To gain insights into the aforementioned concepts an experimental study will be performed during this Master's thesis. The experiments will be conducted in the Open-Jet Facility of the Delft University of Technology, where large-scale tomographic PTV with Helium-Filled Soap Bubbles will be used for data acquisition. The research questions that will be answered in this work are as follows:

- What are the flow field characteristics of the near wake of a VAWT-based MRS?
  - Which flow structures can be identified in the near-wake of the VAWT-based MRS?
  - How does the evolution of these identified flow structures contribute to the overall development of the near-wake in the streamwise direction?
- How does the addition of external lift-generating devices affect the near wake of the VAWT-based MRS?
  - Which flow structures can be identified in the near-wake of the VAWT-based MRS with external lift-generating devices?
  - How does the presence of these external lift-generating devices influence the streamwise evolution of the identified flow structures and the overall near-wake?
  - What is the correlation between the presence of external lift-generating devices and the momentum and power recovery of the near-wake in the streamwise direction?
  - What is the effect of the external lift-generating wings on the thrust coefficient of the VAWT-based MRS?

With the research objective of this Master's thesis outlined and the research questions posed, the subsequent chapters of this report will further dive into the VAWT-based MRS and the concept of wake deflection using external lift-generating devices. In chapter 3 the wind tunnel model will be presented, together with the the design process of the external lift-generating wings. Additionally, the measurement setup is elaborated on in this chapter. The results of this Master's thesis are presented in chapter 4. Here not only the velocity and vorticity profile of the MRS wake is discussed, but also the recovery of streamwise momentum and how the external wings affect the re-energisation process of the wake. Finally, this report concludes the findings in chapter 5, together with several recommendations for future research.

3

Experimental Setup

During this thesis, an experimental campaign has been held to gain further understanding of the near-wake dynamics of the Multi-Rotor System, and how the wake of such a turbine can be deflected through external lifting wings. This chapter will introduce the reader to the wind tunnel where the experiment is conducted, the MRS wind tunnel model, the development of the external wing elements, and the load balance, smoke, and PTV measurement setups. Additionally, this chapter concludes with a brief discussion of the PTV post-processing methods.

3.1. The Wind Tunnel

The experiments have been conducted in the Open Jet Facility (OJF) of the Delft University of Technology. This wind tunnel is an atmospheric, closed-loop, open-jet tunnel, powered by a 500kW fan. Its outlet is of octagonal shape, has a dimension of 2.85x2.85 meters, has a contraction ratio of 3:1, and ejects the flow into the test section of 13x8x8 meters. The tunnel is capable of running flow velocities between 4 and 35m/s, with a turbulence intensity of 0.5% as reported by Lignarolo et al. [39]. The settling chamber of the OJF has been fitted with a seeding rake used to seed the flow with Helium-Filled Soap Bubbles for the Particle Tracking Velocimetry measurements. This rake has a width of 1m and a height of 2m and can be translated along the width of the tunnel to seed different areas of the flow. In the work of Giaqiunta [24], it was found that the presence of this rake increases the turbulence intensity to 0.8%. Figure 3.1 shows a visual representation of the OJF. The experiments have been conducted at a flow velocity of $U_\infty = 4\text{m/s}$ and a density of $\rho_\infty = 1.205\text{kg/m}^3$.

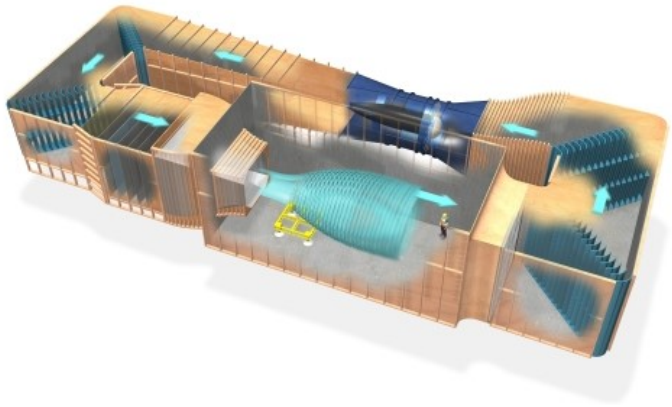

Figure 3.1: Visual representation of the TU Delft OJF.[1]

[1] https://www.tudelft.nl/lr/organisatie/afdelingen/flow-physics-and-technology/facilities/low-speed-wind-tunnels/open-jet-facility

3.2. Wind Tunnel MRS-Model

From the background analysis, it became apparent that little experimental research has been performed on the VAWT-based Multi-Rotor system. As a result, a wind tunnel model had to be developed specifically for this experimental campaign. This and the following section will focus on the design process of the turbine model and the high-lift wings used for wake deflection.
In Figure 3.2 a visual representation of the model and its dimensions is shown. The MRS comprises a grid of 4x4 2-bladed H-type VAWTs mounted to 4 axial shafts. These shafts in their turn are mounted on a support frame constructed from aluminium extrusions. The design of the individual VAWT rotors is based on those in the work of [29], having a rotor diameter of d = 0.30m and a height of h = 0.30m. The blades have a chord length of c = 0.03m and a NACA0012 profile. The rotors on each shaft are staggered 45° with respect to each other, in line with the design as presented in Jamieson et al. [32], where it was selected to ensure a smooth, 8-phase torque input to the generator. The rotor shafts are spaced 1.25d from each other to ensure they benefit from increased performance due to the blockage effect as described in the works of De Tavernier et al. [63] and Vergaerde et al. [67], and avoid them structurally interfering with each other. This rotor spacing results in a total actuator surface width of D = 1.43m, and a height of H = 1.35m, resulting in a turbine reference area of A_{act} = 1.93m^2, used for the calculation of the turbine thrust coefficient. Finally, the support columns of the MRS frame are placed at 1.5R from the rotor edges to minimize any flow interference effects.

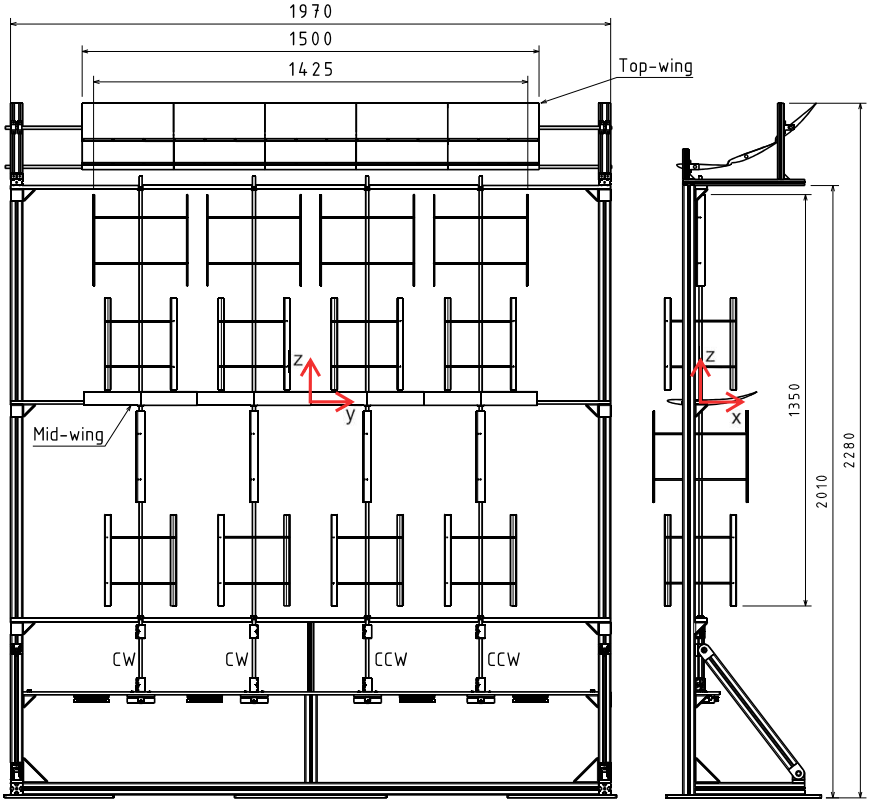

Figure 3.2: Technical drawing showing the main dimensions in millimetres of the MRS, together with the adopted coordinate system. Air flows in the positive x-direction of the illustrated coordinate system.

Each rotor shaft is actively powered by a single Maxon EC90 260W DC motor (500266) and ESCON 50/5 controller (409510) combination. The two rotors on the left of the frame rotate in a clockwise (CW) direction, and the two on the right in a counter-clockwise (CCW) direction, hence the blades of the outer shafts rotate opposite to the flow direction. The rotational directions of the rotors have been annotated in Figure 3.2.

The MRS has been fitted with two removable wing profiles, one in the centre of the actuator plane, and one mounted on top of the MRS frame. These wings aim to induce an upwash into the flow and enhance the mixing of the wake region with their tip vortices. Both wings have a span of 1.5m, with the top wing, oriented at a 21° angle of attack, having a chord length of $c = 0.50$m, and the mid-wing, set at $\alpha = 6°$, having a chord length of $c = 0.30$m. The design of the airfoil profiles of these wings will be further elaborated on in the next section. Both MRS configurations, with and without wings, are displayed in Figure 3.3. Additionally, geometry plots of the final wing profiles have been presented in Figure 3.4.

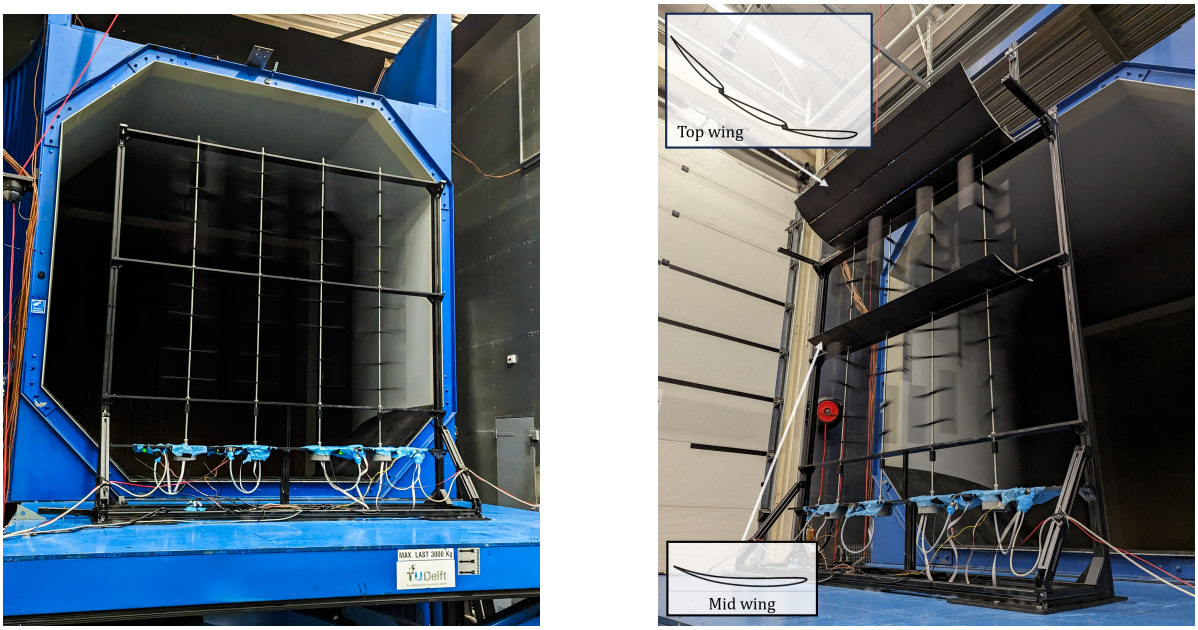

Figure 3.3: Picture of the two MRS configurations (left) without wings and (right) with wings.

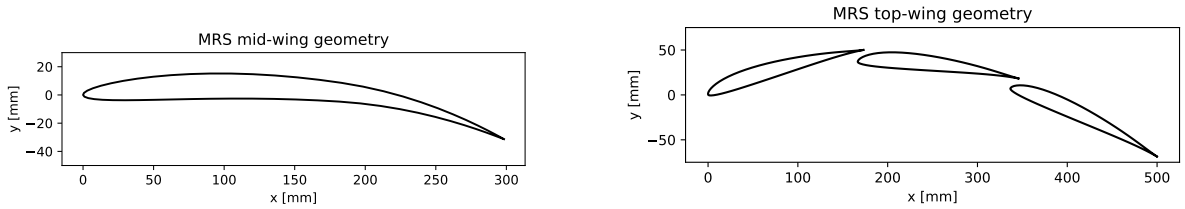

Figure 3.4: Geometry plots of the MRS mid-wing at $\alpha = 6°$ (left) and MRS top-wing at $\alpha = 8°$ (right).

3.3. High Lift Wing Design

As mentioned in the previous section, the wind tunnel model of the MRS is fitted with two wings which have the aim of inducing strong tip-vortices and an upwash onto the wake. The current section takes a close look at the design and development of the airfoil profiles of these wings. From the discussion in section 2.4 it became evident that the strength of the induced upwash of an arbitrary wing is dictated by the circulation around this wing. The larger the circulation Γ, the stronger the tip vortices and upwash. Additionally, here it was stated that to increase this circulation strength one should either aim at increasing the lift coefficient of the wing, increase its surface area/chord length, or apply a combination of the two. While increasing the surface area of the wing is rather straightforward, increasing the lift coefficient is not so much. As was touched upon in section 2.4, the most effective way to achieve such a high lift coefficient is through the concept of a multi-element wing. It was therefore decided during the design process of the MRS model that a large multi-element wing would be mounted on top of the

turbine, and a smaller single-element wing would be located at the centre of its actuator plane. The top wing would be responsible for a strong upwash, whereas the wing on the mid-beam would ensure the wake behind the MRS would be re-energised from the bottom.

3.3.1. Airfoil Selection

During the design of the wind tunnel model and the experiment, it was decided the experiment would be conducted at a flow velocity U_∞ between 4 and 5m/s. This velocity range, which was selected to allow for TSR matching of the VAWT rotors while at the same time keeping the model structurally sound, is an important parameter during the design of the wing, as it dictates the Reynolds number. It soon became evident that depending on the chord length of the wing it would be challenging to achieve a chord-based Reynold number above $1.5 \cdot 10^5$, which in turn would be critical in terms of the maximum lifting capabilities of the wing sections. This relatively low chord-based Reynolds number is not beneficial for the maximum lift coefficient achievable with a given wing section. Primarily because the Reynolds number indicates the ratio between the inertial and viscous forces acting on the wing, and at a lower Reynolds number the boundary layer is more susceptible to laminar separation bubbles and separation in general, which negatively affects these lifting capabilities.
The works of Selig et al. [54] [55] and Lyon et al. [40] were used for the initial airfoil selection, as these references provide numerous $c_l - \alpha$ plots for so-called low-speed airfoils over a range of different Reynolds numbers below $3 \cdot 10^5$. The selected airfoils in turn have at a later stage been used in the design of the multi-element wing which was to be mounted on top of the MRS. In particular, a look was taken at the maximum lift coefficient of these airfoils during the selection process, as the main design requirement was to develop wings that generate as much lift as possible at a given angle of attack. From the aforementioned references, it was found that most airfoils were only capable of achieving a $c_{l,max} = 1.2 - 1.3$ around the Reynolds number range of interest ($Re = 1 \cdot 10^5 - 2 \cdot 10^5$). As a result, only a handful of airfoils were selected to be used during the design process of the multi-element wing. These airfoils are displayed in Figure 3.5, of which their lift polars are displayed in Figure 3.6. The E213, E423, and SD7032 airfoils all had a similar maximum lift coefficient of 1.25 around the desired Reynolds number and were selected based on the behaviour of their lift slope which remained stable over a range of Reynolds numbers, and, which did not have a steep drop after the maximum lift coefficient was reached. Additionally, the S1210 was selected as according to Selig et al. this airfoil had the capability of reaching $c_{l,max} = 1.8$ around the desired Reynolds number, which was significantly higher than the alternative options. The S1210 is capable of reaching this $c_{l,max}$ because it is heavily loaded near the trailing edge, where it sustains a large pressure difference between its upper and lower sides. During the M-tunnel experiments, which will be discussed at a later stage, it was found that the S1210 did not perform as expected. The airfoil suffered from trailing edge separation, thus not being able to sustain this large pressure difference, and thus not achieving the expected lift coefficient.

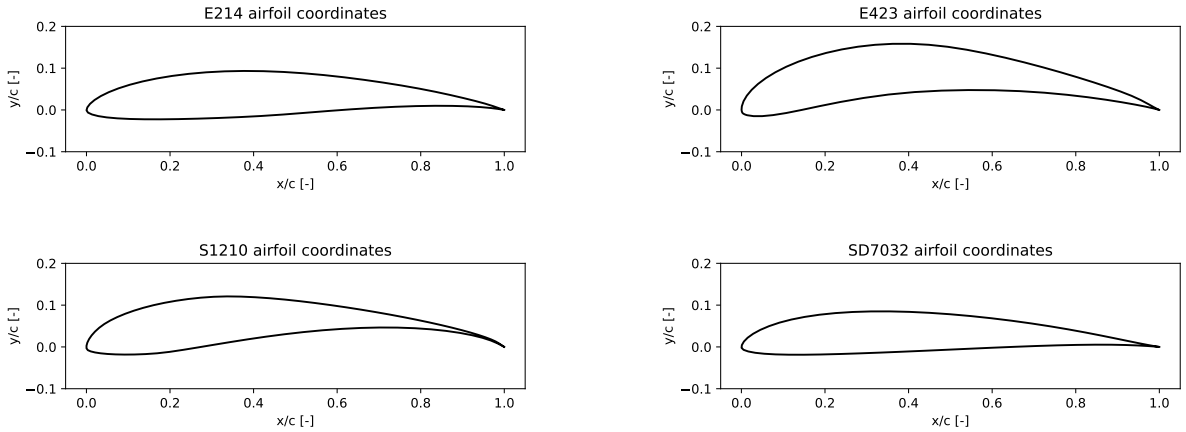

Figure 3.5: Airfoils of interest.

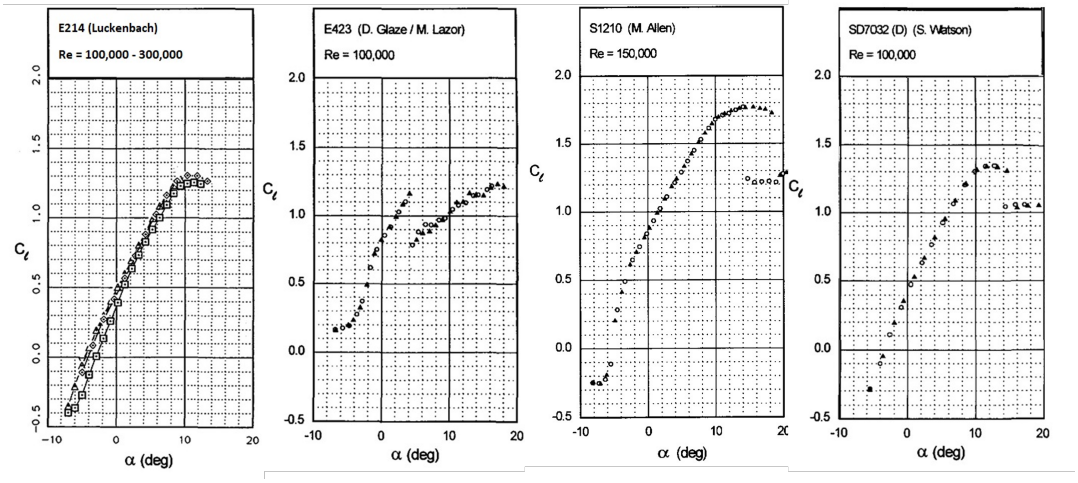

Figure 3.6: $c_l - \alpha$ polars of the E214, E423, S1210, and SD7032 (from left to right). Figures adapted from [54] and [55].

3.3.2. Airfoil Design

With a set of promising airfoils selected the design process was initiated. For this, the software MSES[2] and JavaFoil[3] have been used. Javafoil, which is a potential flow solver, makes use of a *panel method* in combination with a boundary layer analysis to determine the lift slope of a given airfoil. MSES on the other hand makes use of another method where it solves the Euler equations for a grid around the airfoil in combination with a boundary layer analysis. This makes MSES particularly suitable for the analysis of multi-element airfoils when compared to Javafoil.

Three different airfoil designs for the multi-element high-lift wing were configured with the MSES solver, and compared to the performance of the single-element S1210 airfoil. The configured designs are displayed in Figure 3.7. For the 2-element configuration, configured from the E423 airfoil, a $C_{l,max} = 2.0$ was found. For the 3-element airfoil, which was configured from the SD7032 airfoil a $C_{l,max} = 2.5$ was found, and for the 4-element configuration, which consists of a slat element based on the S1210 airfoil, and the E214 airfoil used as the main and flap elements, a $C_{l,max} = 2.6$ was found with MSES. The MSES analyses were performed for $Re = 1.5 \cdot 10^5$. These airfoil designs, of which the numerical results are summarized in Table 3.1, have been validated experimentally in the M-tunnel.

For the wing mounted on the mid-beam of the MRS model, a single-element design was configured in JavaFoil. This airfoil and its dimensions are presented on the left of Figure 3.4. As the MRS design offers little to no room for wing elements with large angles of attack at this location of the turbine, an airfoil was designed with an increased camber towards its trailing edge. According to JavaFoil a $C_{l,max} = 1.6$ at $Re = 0.8 \cdot 10^5$ is to be expected for this design. Due to time constraints, this design could not be validated in the M-tunnel, and thus validation of the design was performed in the OJF, of which the results are discussed in chapter 4.

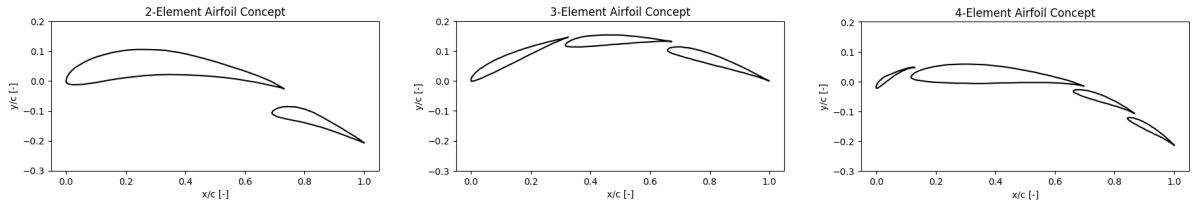

Figure 3.7: Different airfoil designs that have been analysed through MSES and validated in the M-tunnel.

[2] https://web.mit.edu/drela/Public/web/mses/
[3] https://www.mh-aerotools.de/airfoils/javafoil.htm

Table 3.1: Maximum lift coefficient of the 4 different airfoil concepts obtained through MSES (and JavaFoil for the final entry).

Airfoil concept	$C_{l,max}$ [-]	α_{max} [°]	Re_c [-]
2-element concept	2.0	3	$1.5 \cdot 10^5$
3-element concept	2.5	14	$1.5 \cdot 10^5$
4-element concept	2.6	4	$1.5 \cdot 10^5$
Mid wing (*JavaFoil*)	1.6	6	$0.8 \cdot 10^5$

3.3.3. Airfoil Validation

Solvers such as Javafoil and MSES give a good indication of the lift coefficient that is to be expected from a particular wing design, however, it is important to validate these designs through wind tunnel experiments. Therefore the wing designs that were presented in the previous section were 3D printed, and have been tested in the M-tunnel located at the Low Speed Wind Tunnel Laboratory of the Delft University of Technology. The M-tunnel is an open jet tunnel, with a square outlet area of dimensions 0.40x0.40 meters, capable of running flow velocities up to a maximum of 35m/s. Pictures of the M-tunnel setup are shown in Figure 3.8. For the experiment, the multi-element airfoils were mounted to a 3-component balance, also used in the work of Huang et al. [28], where its exact details can be found. The balance utilizes three load cells, two of which are aligned with the normal force direction of the airfoils and the third with the axial force direction. Each load cell is capable of measuring loads over a maximum range of ±50N with an uncertainty of $\leq 0.1\%$. The airfoils have been tested over a range of not only angles of attack but also Reynolds numbers to identify their sensitivity to any change in Reynolds number. Figure 3.8b shows a close-up of the balance setup. Here it is also shown that the angle of attack was varied by rotating the full balance setup manually over a range of angles drawn on the support platform near the M-tunnel exit.

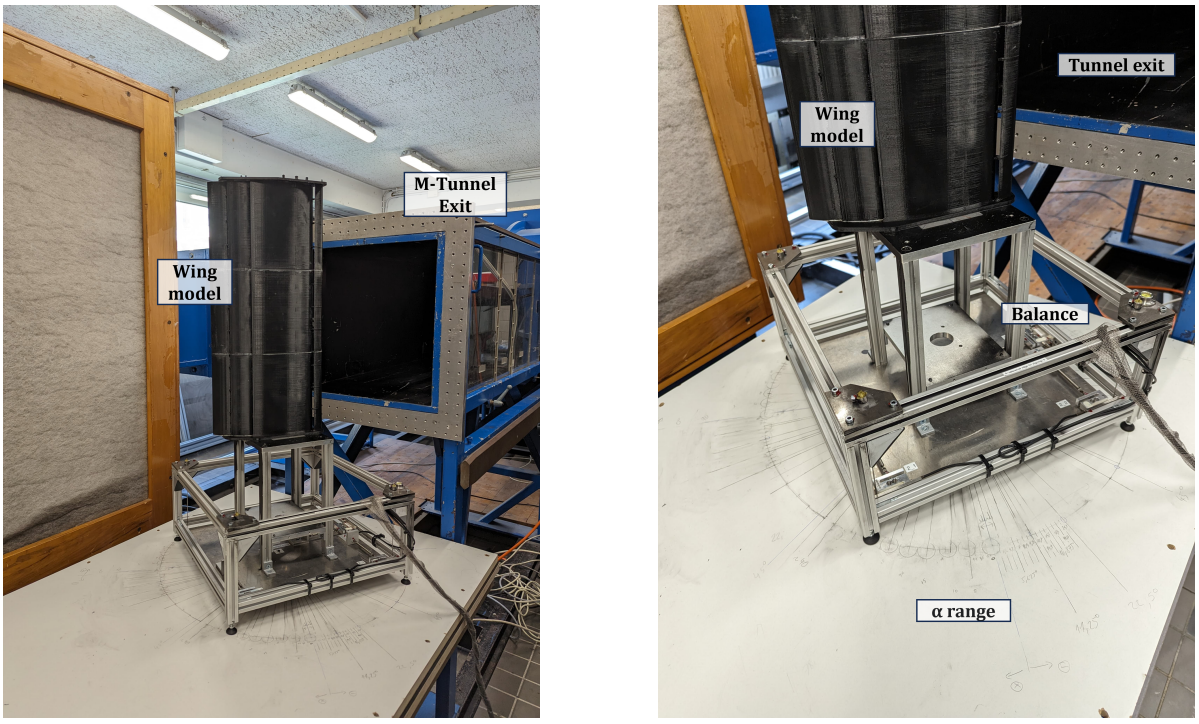

(a) Picture of the M-tunnel setup.

(b) Balance setup and method of setting the angle of attack.

Figure 3.8: M-tunnel wing test setup.

Primary results obtained during the M-tunnel experiment are shown in Table 3.2 and Figure 3.9. Table 3.2 shows an overview of the $c_{l,max}$-values obtained for the different airfoils, together with the corresponding Reynolds number and angle of attack α_{max}. Figure 3.9 shows the lift polars from which

these maximum values have been derived. The results have been corrected for flow blockage and curvature according to the methods described in Garner et al. [3] and Barlow et al. [5].
During the experimental campaign it immediately became clear there existed a large difference between the predicted $c_{l,max}$ by the solvers, and the results obtained during the experiment. Specifically, the measured $c_{l,max}$-values were approximately 40% lower than the predicted values for all three multi-element airfoil designs. It was unclear whether this had to do with the balance or model setup, test method, or wind tunnel corrections, and due to time constraints, there was no room to investigate this discrepancy in depth. As a result, it was decided to choose the best-performing design based on the obtained c_l values. Later on, during the experiment in the OJF, a final validation of the lift coefficient would be performed.

Table 3.2: Results obtained during the M-tunnel experiment for the four airfoil designs of interest.

Airfoil concept	$c_{l,max}$ [-]	α_{max} [°]	Re_c [-]
S1210	1.15	11	$1.6 \cdot 10^5$
2-Element design	1.25	7	$1.3 \cdot 10^5$
3-Element design	1.45	11	$1.5 \cdot 10^5$
4-Element design	1.53	15	$1.5 \cdot 10^5$

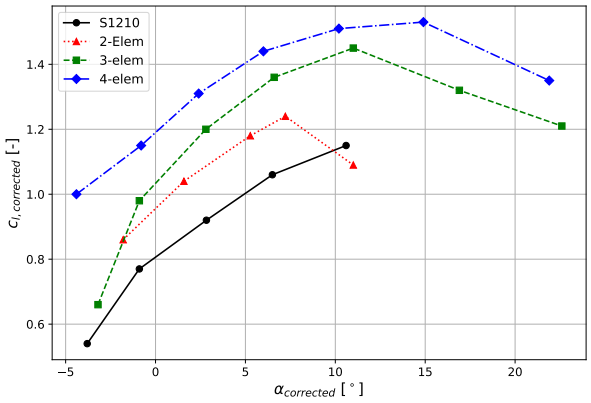

Figure 3.9: Airfoil lift polars obtained from the M-tunnel experiment for the four tested designs, with data collected for increasing angles of attack.

From the table with results it becomes evident that as expected the 3-element and the 4-element designs perform the best, with the 4-element design having a slightly higher $c_{l,max}$. In the end, the decision was made to go with the 3-element design as the final design to be mounted on top of the MRS. The primary reason for this was its simpler design, which would streamline the manufacturing process of the wing since all three elements are identical. Additionally, it was found that this design was less sensitive to flow separation. At its maximum lift coefficient, the 4-element design had almost fully separated flow over its last flap element and a laminar bubble on its main element, whereas the 3-element design was less sensitive to these phenomena.

Before this section on the development of the high-lift wings is concluded, a small sidenote must be made. During the design phase of the airfoils, but more significantly, during the experiment in the M-tunnel, the projected Reynolds number regime ($Re = 5.0 \cdot 10^4 - 1.5 \cdot 10^5$) appeared to be a rather challenging one to operate in. At this relatively low Reynolds number, the boundary layer is prone to flow separation and laminar separation bubbles, resulting in the airfoil not reaching its full potential. Both these effects were visualised during the M-tunnel experiment through surface oil flow visualisation. Once discovered during the experiment, an attempt was made to remove the laminar bubbles and delay the flow separation by actively tripping the boundary layer using zigzag strips. Figure 3.10 shows a subset of the obtained visualisations acquired through the surface oil flow visualisation. In these images, which have been annotated accordingly, clear laminar separation bubbles and flow separation can be observed. Moreover, the effect of tripping the flow using zigzag strips is also seen in these pictures.

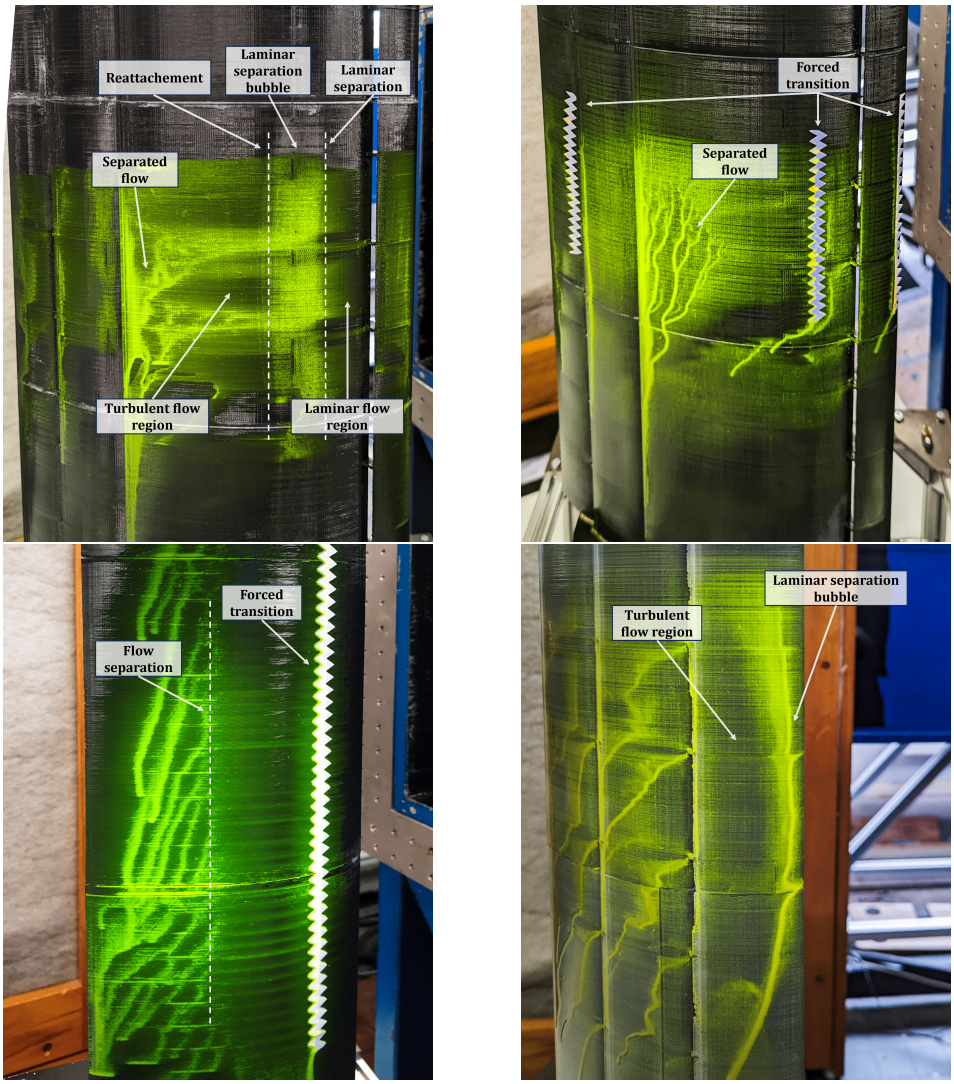

Figure 3.10: Oil flow visualization performed during the M-tunnel experiment on several airfoils at different angles of attack and Reynolds numbers. Freestream flow travels from right to left.

3.4. Load Balance

During the experiment, a number of different load measurements are taken to determine the drag of the turbine frame, and the thrust coefficient of the MRS, but also to validate the lift both the mid-wing and the top wing generate. For these measurements, a 6-component force balance is used, to which the MRS is mounted through a specifically designed mounting plate. Details on the maximum single and simultaneous balance loads for each component are presented in Table 3.3, together with their corresponding percentage maximum error and standard deviation. The error and standard deviation percentages concern the maximum single load values. Here "Single load" refers to the maximum load that a particular component can withstand when it is the only load applied to the balance, whereas "simultaneous load" refers to the maximum load range for that component when all components are loaded simultaneously.

Figure 3.11 shows the setup of the MRS mounted to the load balance for different test configurations. Table 3.4 shows an overview of the different configurations for which load measurements have been taken during the campaign. For each configuration, 5 sets of measurements, each over a period of 10 seconds, are taken and used to compute the mean loads and standard deviations. Measurements have been taken at a range of freestream velocities to identify whether any Reynolds effects or unwanted

vortex shedding takes place. Based on the results of the load measurements a final MRS configuration is selected for which the PTV measurements are performed.

Table 3.3: Summary of the performance metrics for the 6-component force balance.

Component	Max. Single Load	Max. Simultaneous Load	Max. Error	Standard Deviation
F_x	± 250 N	±250 N	0.06%	0.02%
F_y	± 600 N	±500 N	0.23%	0.05%
F_z	±3500 N	±500 N	0.16%	0.05%
M_x	± 550 Nm	±500 Nm	0.05%	0.01%
M_y	± 500 Nm	±250 Nm	0.05%	0.01%
M_z	± 125 Nm	± 50 Nm	0.25%	0.07%

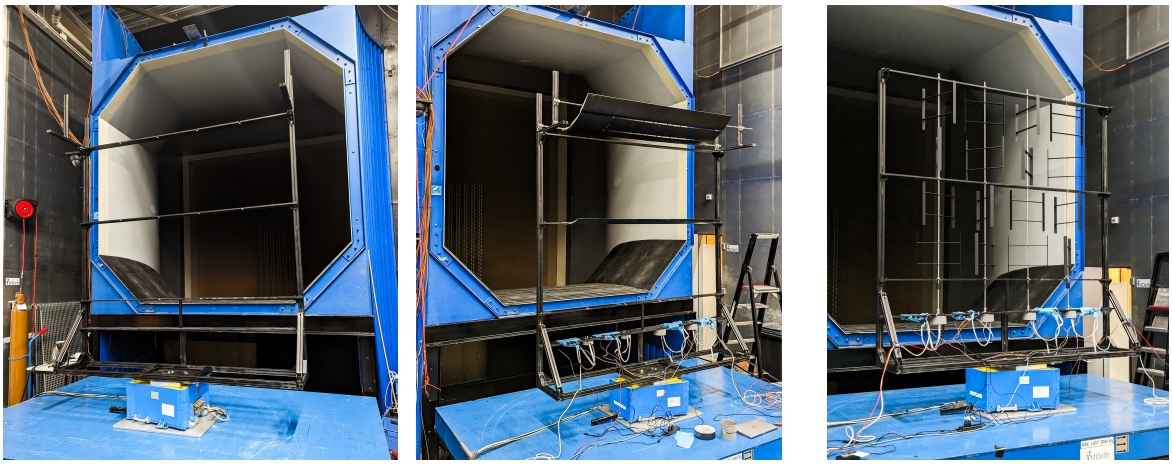

Figure 3.11: Different MRS configurations for which load measurements have been performed. Frame only (left), frame + both wings (middle), and frame + rotors (right).

Table 3.4: Overview of load measurements taken during the experiment.

	Configuration	Flow velocity [m/s]	Rotor Rotational Speed [rpm]
Wing performance	Frame only	3.0 - 5.0	N/A
	Frame + top wing	3.0 - 5.0	N/A
	Frame + mid-wing	4.0	N/A
	Frame + both wings	4.0 - 5.0	N/A
MRS performance ($C_T - \lambda$)	Frame only	3.5 - 4.5	N/A
	Frame + rotors	3.5 - 4.5	0
	Frame + rotors	0	700 - 1200
	Frame + rotors	4.0	700 - 1200
	Frame + rotors + top wing	4.0	750 - 850
	Frame + rotors + both wings	4.0	750 - 850

3.5. Smoke Visualisation Setup

At the start of the experimental campaign, smoke visualizations were conducted as a proof-of-concept, validating whether the presence of the external wings deflected the wake as anticipated. To achieve this, a probe injecting smoke into the flow was suspended at different locations at 0.54m upstream of the MRS, Figure 3.12a. The effect of the presence of the wings was then quantified by tracking the interception point of the smoke streamtube with a grid of strings, located 1.58m downstream of the MRS. This downstream grid is visualised in Figure 3.12b. The strings of this grid had a spacing of 0.10m in both directions. The location where the smoke intercepted with the grid was recorded by a DSLR camera positioned at a fixed location further downstream of the grid. Smoke was injected at 4 different upstream locations, visualised in Figure 3.13, for four different turbine configurations, namely with and without wings and with and without spinning rotors. It is important to note that the grid, used to quantify the location of the smoke stream tube, was shifted from left to right depending on the location where the smoke was injected into the flow, as the grid did not cover the full downstream area of the MRS.

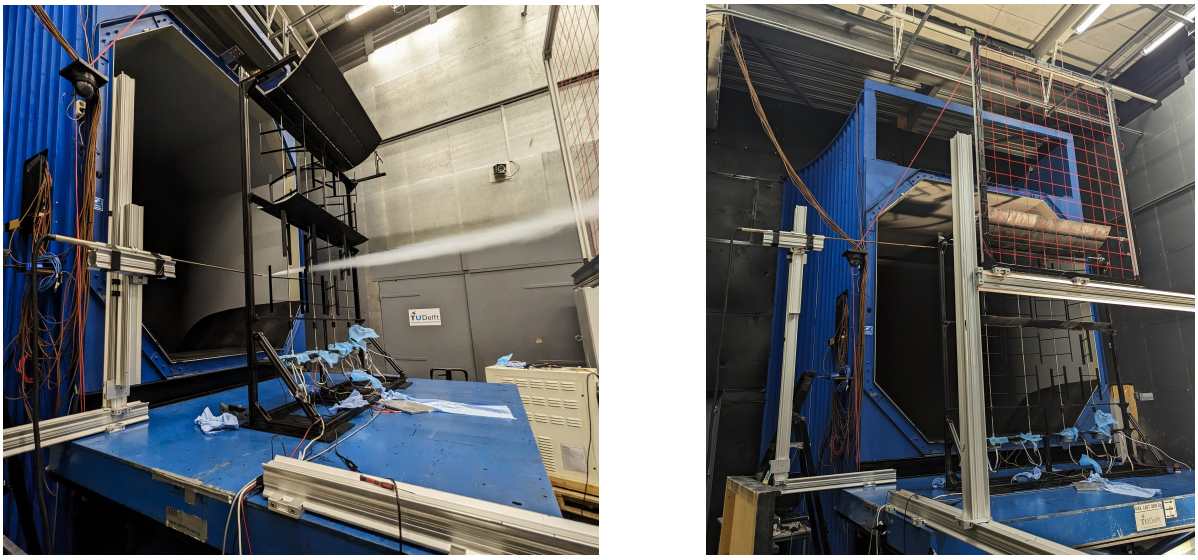

(a) Smoke injection probe.

(b) Downstream grid.

Figure 3.12: Smoke visualisation setup.

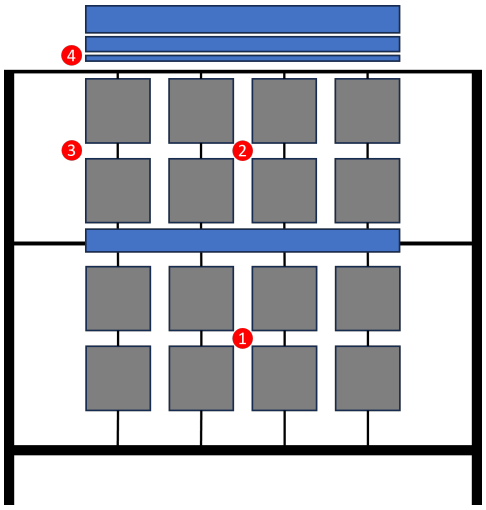

Figure 3.13: Schematic of smoke injection locations.

3.6. PTV Setup

As the aim of this project is to gain insight into the near-wake dynamics of the VAWT-based MRS, Particle Tracking Velocimetry or PTV has been employed to perform measurements in the wake region of the system. In Figure 3.14 a picture of the PTV setup is shown to get the reader acquainted with both the setup and its challenges. This image shows the different elements of the experimental setup, namely the MRS, the wind tunnel exit, and the PTV imaging and illumination setup. Here the cameras, labelled C1-C4, represent the imaging part of the setup, while the laser serves as the illumination element. Figure 3.14 also highlights one of the challenges of the experiment: the limited Field Of View (FOV) resulting from the constrained seeding area. One can see that the illuminated particles do not cover the entire width or the entire height of the MRS. The current section provides an in-depth look into the PTV setup, and how the desired measurements have been achieved. PTV requires three main elements, tracer particles which trace the behaviour of the flow, illumination to visualise the tracer particles at the region of interest, and an imaging setup to capture the tracer particles. All three elements will be covered in this section, together with further details on the model setup and measurement locations.

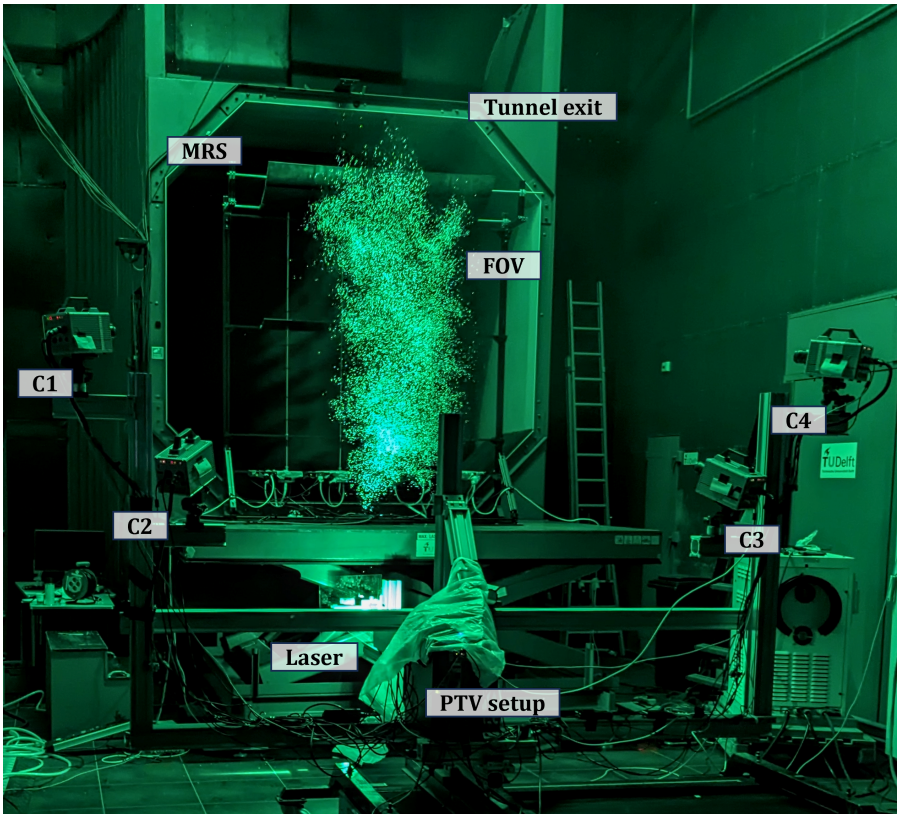

Figure 3.14: Overview of the PTV setup, with C1-C4 representing the high-speed cameras.

3.6.1. Seeding System

As introduced in subsection 2.5.3, to visualise the behaviour of the flow, tracer particles are injected during the experiment. For this purpose, Helium-Filled Soap Bubbles with a median diameter of $300\mu m$ are used. These particles are naturally buoyant and therefore capable of following the motion of the flow. The particles are injected into the flow through a seeding rake, Figure 3.15a, located in the settling chamber of the OJF. This rake, which has a width of 1m and a height of 2m, has a large number of nozzles, visualized in Figure 3.15b, which inject the bubbles into the flow. Due to the contraction ratio of the OJF, the effective area seeded by the rake only equals 1.2m x 0.6m. This region is the portion of the flow that can be visualised by the combination of particles and laser for a given seeding rake location. Although this region might vary a bit due to blockage introduced by the model, it does not cover the full area of interest downstream of the MRS. As a result, the seeding rake was traversed laterally in the settling chamber of the MRS such that different areas of the flow could be seeded.

(a) OJF seeding rake.

(b) Seeding rake nozzles.

Figure 3.15: Pictures of the seeding rake used during the experiment.

3.6.2. Imaging and Illumination Setup

Due to the limited region that could be seeded by the seeding generator, the seeding rake was traversed laterally along the width of the wind tunnel. As a result the illumination and imaging setup also required the capability of traversing laterally along the width of the tunnel to be able to capture the streamtube seeded by the generator. To achieve this the imaging and illumination setup was mounted on a traversing setup, of which a picture is provided in Figure 3.16.

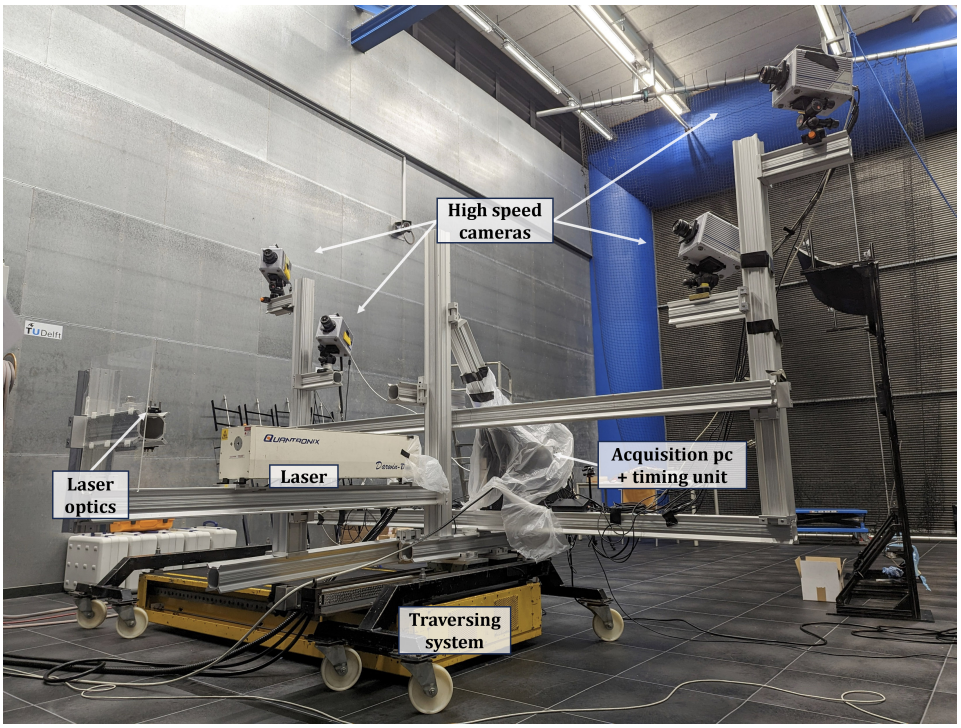

Figure 3.16: Imaging and illumination setup mounted on the traversing system.

The illumination part of the setup consists of a high-power laser and a set of optics converting the laser beam into a thick laser sheet. For this purpose, the Quantronix Darwin-Duo Nd:YLF laser was utilized, emitting light at a wavelength of 527nm with a pulse energy of 25mJ at a repetition frequency of 1kHz. To convert the laser beam into a thick laser sheet with a thickness of 30mm, a combination of a 45° mirror and two cylindrical lenses was used.

For the imaging part of the PTV setup 4 high-speed Photron Fastcam SA1 cameras were used. These cameras have a sensor size of 1 MegaPixel, with a pixel pitch of 20μm, capable of shooting at 5400Hz at full resolution. Each camera was fitted with a 35mm lens, having the aperture set at $f/11$, and being equipped with Scheimpflug adapters to correct for the Scheimplug-principle where the plane of focus of the cameras is not aligned with the acquisition plane. Distances between the laser plane and the individual cameras mounted on the traversing setup are displayed in Figure 3.17.

Data acquisition is performed through the LaVision Davis 10 software, running on a PC located on the traverse system, in combination with the LaVision PTU-X High-Speed Controller unit. PTV data is acquired over a period of 4 seconds, at an acquisition frequency of 1000Hz, resulting in a dataset of 4000 images per camera. The cameras have been directly connected to the acquisition PC by means of ethernet cables to ensure fast transfer speeds between the internal storage of the cameras and the PC.

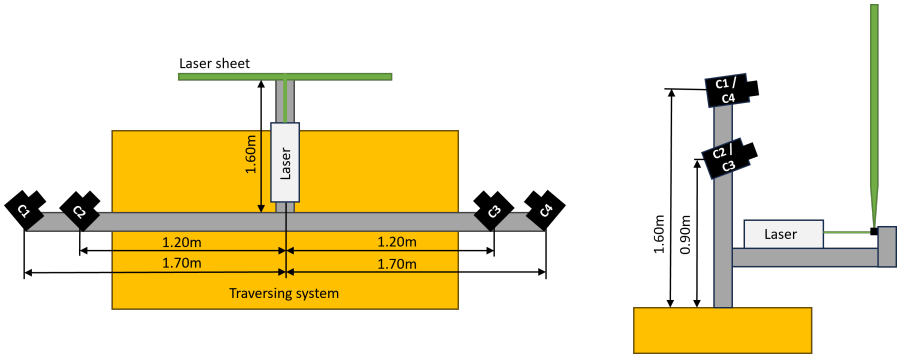

Figure 3.17: Traverse system setup dimensions top view (left) and side view (right).

3.6.3. Measurement Planes

With the aim of gaining insights into the streamwise evolution of the wake properties in the near wake of the MRS, but also due to the limited seeding region, the measurement setup had to be designed to allow for large displacements in both streamwise and lateral directions with respect to the MRS. To achieve this, the PTV acquisition system was mounted on a traversing system, allowing movement of the imaging and illumination setup in both directions. A schematic top view of the traverse system setup, together with a schematic showing the downstream measurement locations is provided in Figure 3.18. Here Figure 3.18a shows the different downstream measurement locations, 4 distinct downstream (x/D)-locations, being 1.0D, 1.5D, 2.0D, and 2.5D, with D being the width of the actuator plane of the MRS D = 1.43m, visualised by the green lines representing the PTV laser sheet. Additionally, Figure 3.18b shows the traversing system setup used to acquire the wake measurements at different locations. The yellow box in this schematic represents a mechanically controlled traversing system, allowing precise movement of the camera (C1 - C4) and laser setup within a limited x- and y-range (1.0m and 1.5m respectively) that have been mounted on top of it using aluminium extrusions. A picture of this setup is provided in Figure 3.16. The range of motion of the traverse system must ring a bell for the attentive reader, as this displacement in the downstream direction does not allow enough range to perform measurements at both 1.0D and 2.5D. To resolve this the entire traversing system was moved up and downstream to perform measurements over the aforementioned range.

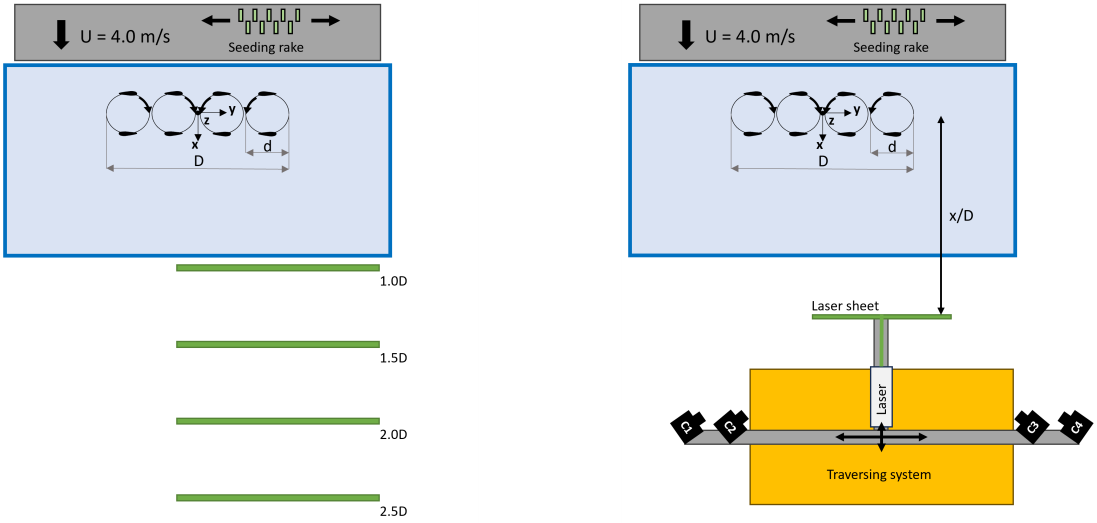

(a) Downstream measurement locations.

(b) Traverse system setup.

Figure 3.18: Schematic representation of the PTV setup.

MRS Orientation

With the turbine in the upright position as presented so far it was not possible to measure the flow field downstream of the top of the MRS. The seeding system, used to seed the flow with tracer particles, was only capable of seeding the flow up to a height of 1.2m. The MRS however surpasses that height, and therefore a solution had to be found to measure the upper regions of the flow. To resolve this, one had the option to lower the table on which the MRS was mounted. This, however, would result in the lower rotors being outside of the jet of the OJF, potentially affecting the flow field behind the MRS. A secondary setup was therefore constructed with the MRS rotated 90 degrees clockwise to resolve this. This allowed the PTV acquisition setup to remain as is, with the orientation of the MRS adjusted to allow measurements of the top half of the turbine. Both orientations of the MRS have been displayed in Figure 3.19.

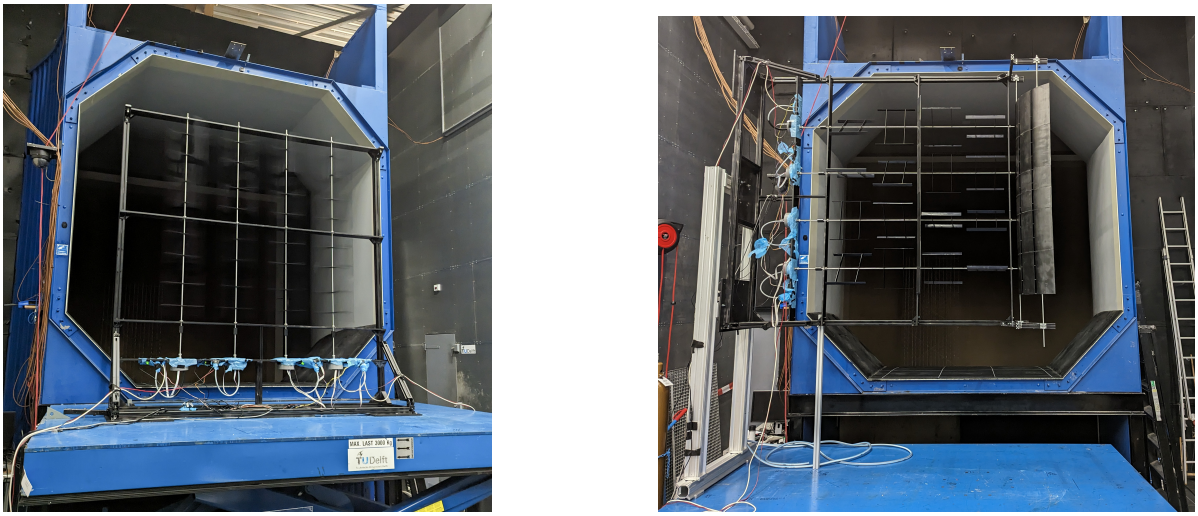

(a) MRS without wing in the upright position.

(b) MRS with wings in the rotated position.

Figure 3.19: Two orientations of the MRS.

Determining the MRS Location in Space

From the sections before, it becomes evident that both the PTV setup and the MRS model were shifted in space multiple times during the experiment to acquire the desired data. As a result, a method had to

be found for locating the MRS within the measurement plane. To locate the MRS, a perspex sheet was elevated within the FOV of the cameras, being aligned with the laser plane as shown in Figure 3.20a. A laser pointer was fired from a known location on the MRS towards the perspex sheet, resulting in the laser becoming visible on the perspex sheet. This process is depicted in Figure 3.20b. By taking pictures with the PTV system of the laser dot on the perspex sheet, the location of the dot could be related to the location from which the laser was shot within the y-z acquisition plane, allowing the determination of the position of the MRS in space during post-processing.

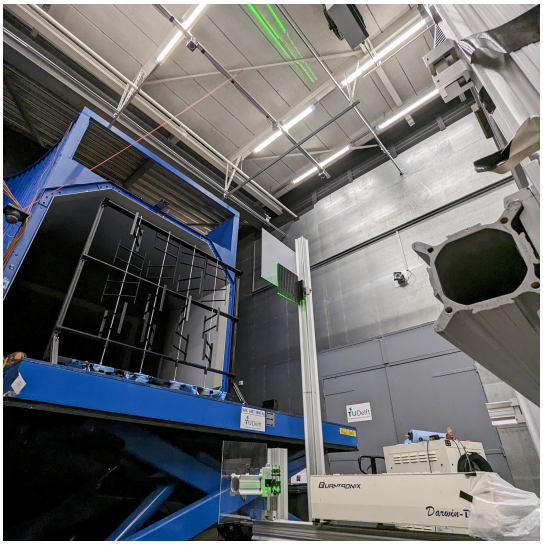

(a) Alignment of perspex sheet with the measurement plane.

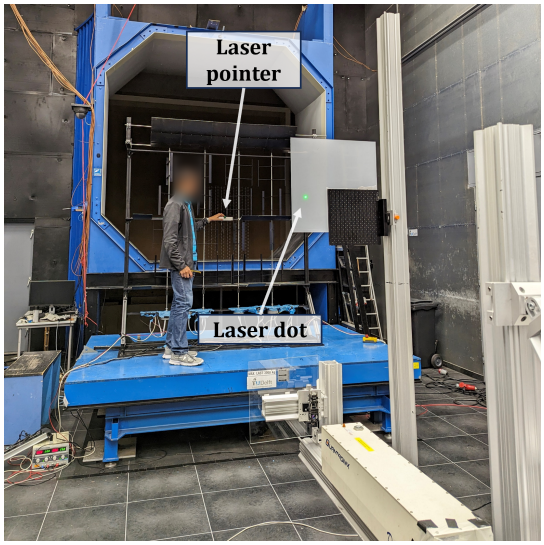

(b) Laserpointer projected on perspex sheet.

Figure 3.20: Setup to determine the position of the MRS within the measurement domain.

3.6.4. Overview of Main PTV-Setup Details

In this section of the report, a table is presented in Table 3.5 showing the main parameters of the PTV setup.

Table 3.5: Table summarising the main PTV setup parameters.

Flow conditions		Acquisition FOV	
U_∞	4m/s	x (thickness)	40mm
Reference length	D=1.43m	y (width)	600mm
Re	$3.81 \cdot 10^5$	z (height)	1200mm
Illumination		**Flow Seeding**	
Laser	Quantronix Darwin-Duo Nd:YLF, $\lambda = 527nm$	Tracer particles	Helium-Filled Soap Bubbles
Optics	45° mirror 2x cylindrical lenses: Cyl-50, Cyl-30	Seeding concentration	1 bubble/cm^3
Imaging			
Camera	Photron FastCam SA1	Objective	Nikkor 35mm f/1.8G
Sensor size	20mmx20mm	Set aperture	f/11
Sensor resolution	1024x1024 pixels	Scheimpflug adapter	±15°
Laser Sheet Distance	2.2m	Magnification factor	0.016
Digital Image Resolution	0.90 px/mm		
Acquisition			
Device	LaVision PTU-X	Acquisition frequency	1000Hz
Acquisition software	LaVision Davis 10	Acquisition interval	4 seconds

3.6.5. PTV Post-Processing

The data acquired during the PTV acquisition is in the form of pictures and is thus not directly quantitative. To convert these images captured by high-speed cameras into quantitative data, representing for example velocity and vorticity fields, the data must be post-processed. This section delves into the main steps of the post-processing of the PTV data.

PTV System Calibration

The conversion of obtained particle fields to velocity fields is done with the LaVision Davis 10 software[4]. For this, a calibration of the software is required, which relates real-world dimensions to the camera pixels. This calibration consists of two parts, the first being a geometric calibration. During the geometric calibration, a 3-dimensional calibration plate is aligned with the PTV laser sheet, after which images are acquired of this plate. A picture of this process is displayed in Figure 3.21. The calibration plate used is in-house developed, and a scaled-up version of the "LaVision Type 30" calibration plate. The pin-hole model was used as the calibration model within the Davis software.

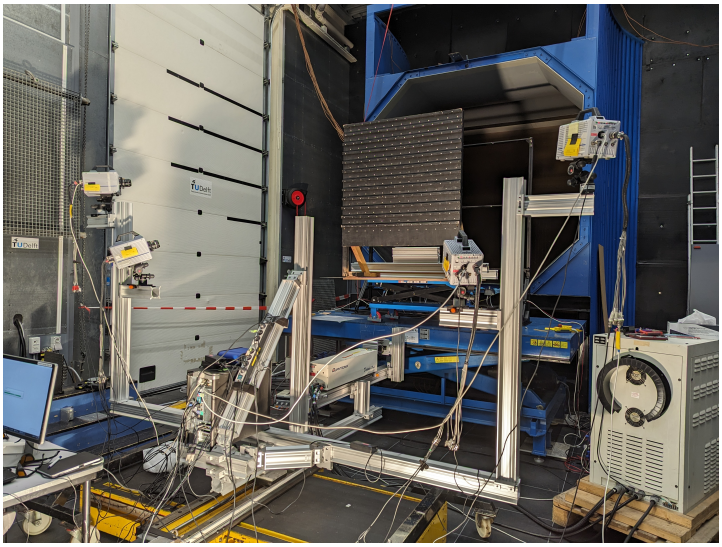

Figure 3.21: Picture showing the acquisition setup for the geometric calibration, with the calibration plate aligned with the laser sheet.

With the geometric calibration in place, which in most cases yielded a fit error in the order of 0.7 pixels, the calibration was refined through the so-called "Volume Self Calibration" (VSC). For this, a small set of particle images, acquired during the PTV measurements, were used. A third-order polynomial fit model was selected, yielding a fit error in the order of 0.01 pixels for most cases after this VSC. For more information on the concept of VSC, the reader is referred to the work of Wieneke [71]. This calibration is then used to compute the Optical Transfer Function (OTF), which is required to perform the Shake-The-Box algorithm later. More background information on the OTF can be found in the work of Schanz et al. [51].

Shake-The-Box

To go from the particle images from the high-speed cameras to the reconstructed volume containing particle tracks the so-called "Shake-The-Box" (STB) algorithm is used. For an in-depth explanation of STB, the reader is referred to the work of Schanz et al. [50], but the main principles will be covered briefly in this section.
In Figure 3.22 the process of shake-the-box is visualised. On the left, it shows the 4 sets of images obtained from each camera. Before the algorithm is applied pre-processing is performed on the images, where the time-averaged minimum light intensity (a moving filter length of 5 images) is subtracted from each image, removing any unwanted background noise. With the pre-processing done the STB algorithm is applied, which yields Lagrangian particle tracks. In short, the algorithm uses the 4 sets of

[4] https://www.lavision.de/en/products/davis-software/

images obtained from the 4 high-speed cameras to compute the temporal and spatial particle tracks, which it uses to reconstruct the measurement volume. On the right of Figure 3.22 such a reconstructed measurement volume is presented, showing the identified particles and their tracks for a given time instance.

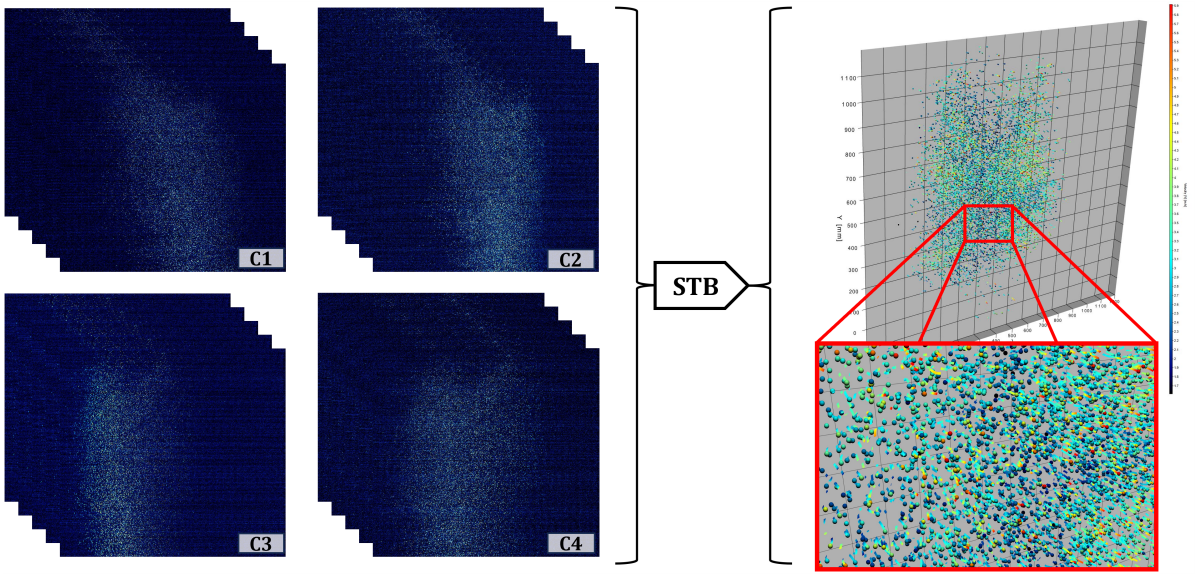

Figure 3.22: Visualisation of the STB process with on the left the raw particle images obtained from the 4 high-speed cameras (C1 - C4), and on the right the reconstructed volume with individual particle tracks.

Stitching of FOVs

As previously mentioned in section 3.6, due to the size of the MRS model and the limited size of the seeding rake, multiple FOVs had to be acquired to construct the measurement volume of interest for a given downstream x/D-location. To construct this full FOV, the individual smaller reconstructed volumes obtained from the STB operation are merged to create a single large volume, covering the full region of interest. This is done through a built-in operation in Davis 10. Figure 3.23 shows a schematic representation of the locations of the different FOVs with respect to the MRS model. The figure on the left shows the case where the MRS is in its upright orientation, and the figure on the right shows the case where the MRS was rotated. Each rectangle, which has either been hatched with dots or circles and is either blue or red, represents a single acquired FOV. For the turbine in the upright orientation, it shows that the full FOV comprises 6 smaller FOVs, whereas the merged FOV for the rotated turbine comprises 3 FOVs. It is important to note that the upper FOVs in the case of the upright turbine were only used for the "no wing" configuration. This is because the process of acquiring these FOVs involved lowering part of the MRS outside of the jet boundary, which in the case of the "with wing" configuration resulted in interference between the wing vortices and this jet-boundary, affecting the flowfield. To conclude, Figure 3.24 visualizes how the smaller reconstructed measurement volumes are merged into a single large measurement volume.

Particle Binning

The STB operation and merging of the sub-volumes yield a single large volume containing many Lagrangian particle tracks, each representing a velocity and acceleration. Such a reconstructed volume is acquired at each downstream measurement location for both MRS configurations. A binning operation is performed on these reconstructed volumes to obtain time-averaged data. For this, the built-in binning operation in Davis 10 was used, where a bin size of 92x92x92 voxels (10x10x10 cm), an overlap of 50%, and a minimum number of 10 particles per bin were selected for this operation. The presented bin size was selected as this covered the full thickness of the measurement volume. Figure 3.25 shows the result of this binning operation, where on the left the particle field is shown for a given time instance, with on the right the resulting time-averaged velocity field.

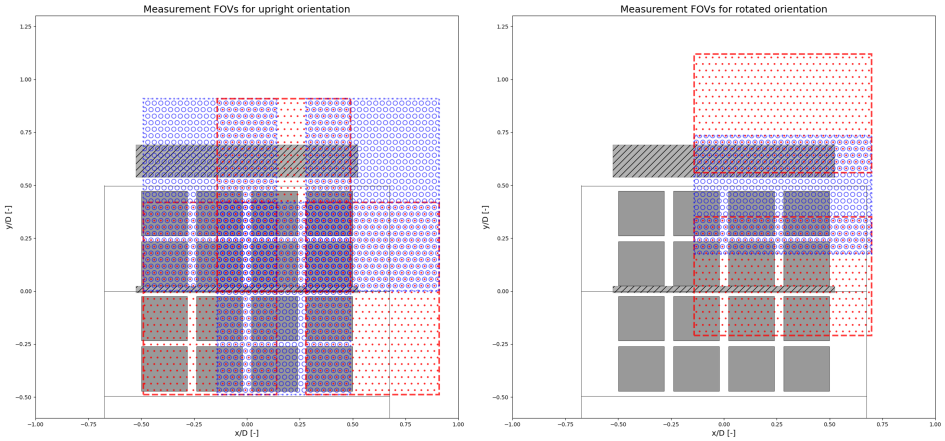

Figure 3.23: Plots showing the individual FOV locations w.r.t. the MRS model. Dimensions have been normalized w.r.t. the actuator width $D = 1.43$m

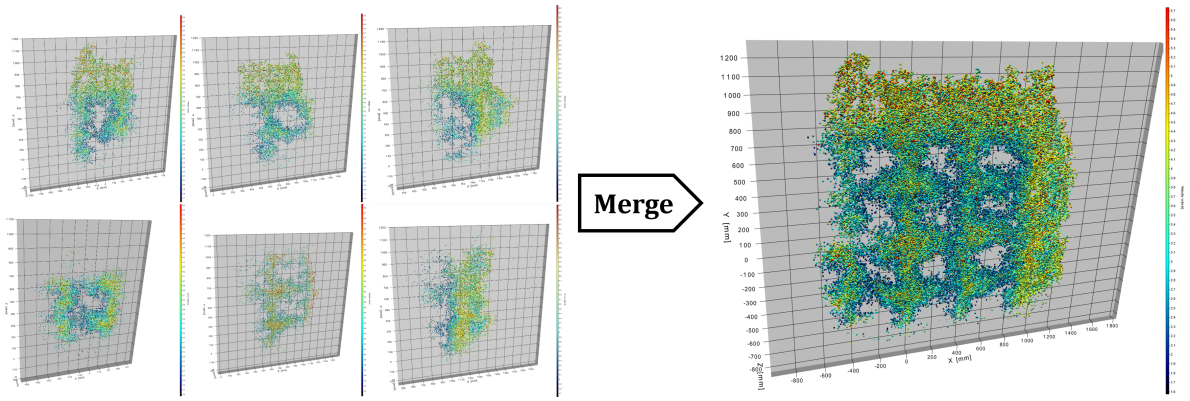

Figure 3.24: Visualisation of the individual reconstructed particle volumes and the merged particle volume at a given time instance.

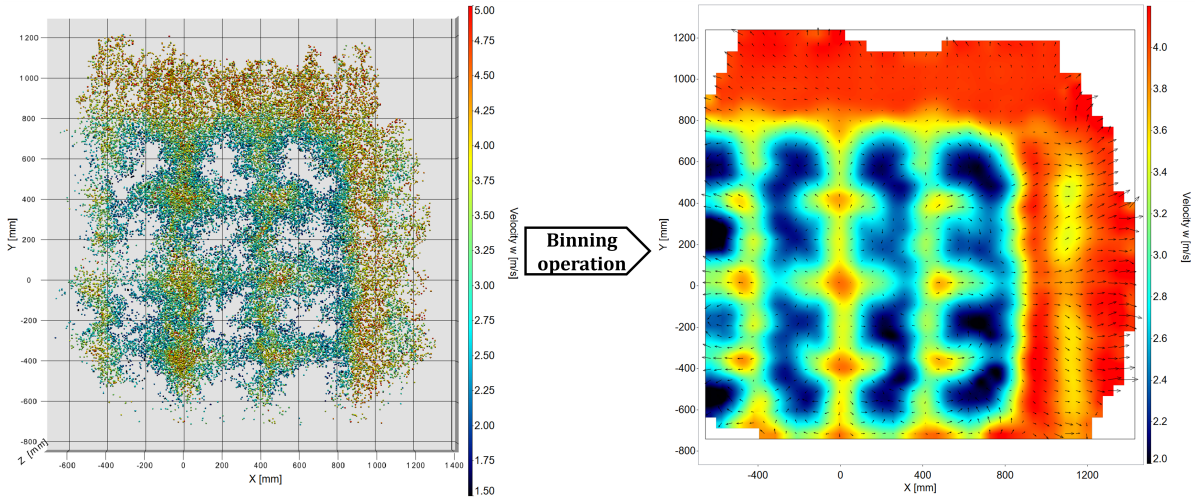

Figure 3.25: Conversion from particle field (left) to binned velocity field data (right).

4

Results and Discussion

With the methodology in place, this chapter will dive into the main findings of this thesis work. The results presented in this section of the report will shed light on the performance and the near-wake of the VAWT-based MRS. First, a look will be taken at the load measurements obtained in the OJF in section 4.1, where both a look is taken at the thrust the MRS exerts on the flow, and the performance of the high lift wings is validated. This is then followed by an intermediate section, section 4.2, which presents the results of the smoke measurements taken ahead of the PTV experiment, providing a proof-of-concept regarding the wake deflection through external lift-generating devices. Finally, the largest part of this chapter will cover the results obtained through the PTV measurements, which are discussed section 4.3. Here not only the velocity and vorticity fields of the near-wake of the MRS are presented and discussed, but also the effect of the external wings on the streamwise momentum and power recovery of the wake.

4.1. Load Results

In the following section, the results of the acquired load measurements will be presented and discussed. The section will start with the validation of the high-lift wing, after which it is concluded by presenting the $C_T - \lambda$ graph for the MRS with and without wings.

4.1.1. High Lift Wing Validation

This section presents the performance of the external wings, of which the development was discussed in section 3.3. Table 4.1 shows an overview of the lift and drag coefficients of both the top wing and the mid-wing. The force coefficients presented in this table represented those of the isolated wings, hence any force induced by the frame has been removed. Additionally, two new force coefficients have been introduced for the wings, namely C_Z and C_X, which are similar to C_L and C_D but are using the actuator surface area A_{act} as reference area instead of the wing surface area S as can be seen in Equation 4.1. The reasoning behind the introduction of these additional coefficients is that the upwash as induced by the wings can be related to the ratio between the thrust force induced by the turbine (represented by C_T) and the lift force induced by the wings. By normalising the forces of the wings in a similar manner to how the thrust force is normalised to C_T, one can easily determine this ratio.

$$C_Z = \frac{F_z}{\frac{1}{2}\rho U_\infty^2 A_{act}} \tag{4.1}$$

Table 4.1: Performance of the isolated external wings. Values have been corrected by removing any forces induced by the support frame.

	Re_c [-]	α [°]	F_z [N]	F_x [N]	C_L [-]	C_D [-]	C_Z [-]	C_X [-]
Top wing	1.34×10^5	21	14.4	4.25	1.97	0.583	0.77	0.23
Mid wing	0.80×10^5	6	2.39	0.05	0.56	0.011	0.13	0.002
Double wing	-	-	16.5	4.56	-	-	0.89	0.24

Effect of MRS Operation on the Wing Lift

The aforementioned results reflect how the wings perform when isolated from the MRS. To assess the influence of the rotating VAWT rotors on their performance, the downward (z) loads generated by the wings in the isolated case will be compared with those mounted on the operating MRS. The loads in the z-direction of the wings, which directly translate to the generated lift, along with their corresponding coefficient C_Z, are reported in Table 4.2 for both cases. The forces presented in this table represent isolated lift values; therefore, any forces induced by the frame or the rotors have been removed.
Comparing the isolated values with the lift values obtained when mounted on the operating MRS it becomes clear that the operating MRS affects the lifting performance of the wing. Both the top and the mid-wing generated less lift when the MRS was operating. This, however, is to be expected as the operating MRS introduces a strong blockage effect. This blockage effect not only causes a reduction in flow velocity, reducing the lift generated but also affects the angle of attack perceived by the wings. This in particular is the case for the top wing. The blockage of the MRS causes air to flow around the system, inducing an upwash in the region of the top wing. This upwash, clearly visible in the PTV results discussed in subsection 4.3.1, causes the perceived angle of attack of the top wing to decrease, resulting in a decrease in lift generated.

Table 4.2: Effect of the MRS on the performance of the external wings.

	Isolated wing		Operating MRS	
	F_z [N]	C_Z [-]	F_z [N]	C_Z [-]
Top wing	14.4	0.77	11.48	0.63
Mid wing	2.39	0.13	2.02	0.11

4.1.2. MRS Thrust Measurements

From the load measurements, the time-averaged thrust coefficient of the MRS in the streamwise direction ($C_{T,x}$) is calculated by Equation 4.2 across various tip speed ratios λ. Here F_x denotes the force exerted in the streamwise direction. This force has been corrected for any drag forces from the frame in the x-direction. Results are displayed in Figure 4.1 for the baseline MRS configuration, and its configuration with external wings. Two configurations with external wings were tested, one with only the top wing mounted and one with both the top and the mid-wing mounted. For each winged configuration, two sets of data points are presented: one where F_x includes both the force induced by the actuator surface and the (drag) force of the external wings in the streamwise direction and another set, labelled with an asterisk (*), where the (drag) force of the wings in the streamwise direction has been removed from F_x, thus representing solely the force induced by the actuator surface.

$$C_{T,x} = \frac{F_x}{\frac{1}{2}\rho U_\infty^2 A_{act}} \tag{4.2}$$

From Figure 4.1, it becomes evident that for increased λ, the thrust coefficient of the MRS increased for all three configurations. This behaviour of C_T aligns with what is observed in the literature for individual VAWTs by for example Huang et al. [29]. Additionally, it can be observed that with the wings mounted to the frame, C_T increases slightly (between 2% – 3%) for a given tip-speed ratio. This increase in C_T when the wings are mounted to the MRS matches with the expectations: the suction side of the wing induces an acceleration on the flow, as a result of which an increased flow velocity is experienced at the actuator plane, resulting in a larger force being exerted on the flow thus increasing the thrust coefficient. Furthermore, the figure indicates that the total streamwise force induced by the actuator surface and the wings is comparable for the configuration with only the top wing and the configuration with both wings. However, when looking at the corrected values for $C_{T,x}$, Figure 4.1 indicates that a larger force is induced by the actuator surface when only the top wing is mounted when compared to the configuration where both wings are mounted. This effect can be explained by the fact that the mid-wing is mounted in the centre of the actuator plane. As a result, its suction side induces an acceleration on the flow, but its pressure side decelerates the flow, as a result also diminishing the effect of the induced acceleration by the top wing. Therefore the actuator surface most likely experiences less accelerated flow when compared to the case where only the top wing is mounted, resulting in a lower induced streamwise force by the isolated actuator surface.

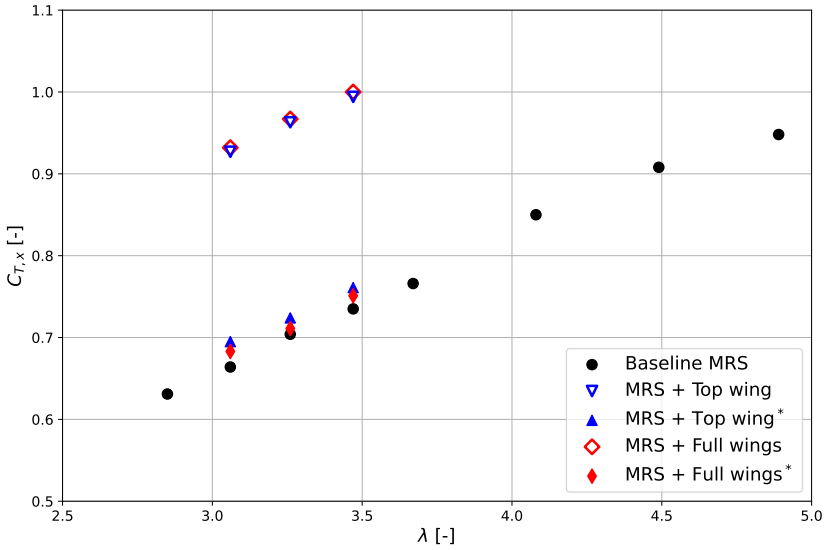

Figure 4.1: Time-averaged thrust coefficient of different MRS configurations ($Re_D = 3.82 \times 10^5$). * indicates the value has been corrected by removing the drag of the isolated wings.

4.2. Smoke Visualisation

As mentioned in the methodology chapter, at the start of the experiment smoke visualisations were performed as a proof of concept to validate whether the presence of the wings affected the deflection of the wake. The results of these smoke visualisations are presented in Figure 4.2. Figure 4.2 shows the intersection points of the smoke streamtube with the downstream grid for the 4 different injection points for the MRS with and without wings. Additionally, it shows how MRS operation (non-rotating versus rotating rotors) affects the behaviour of the streamtube for a given configuration. Displacements of the streamtube between the two MRS configurations for an identical smoke injection point are indicated by the blue arrows.

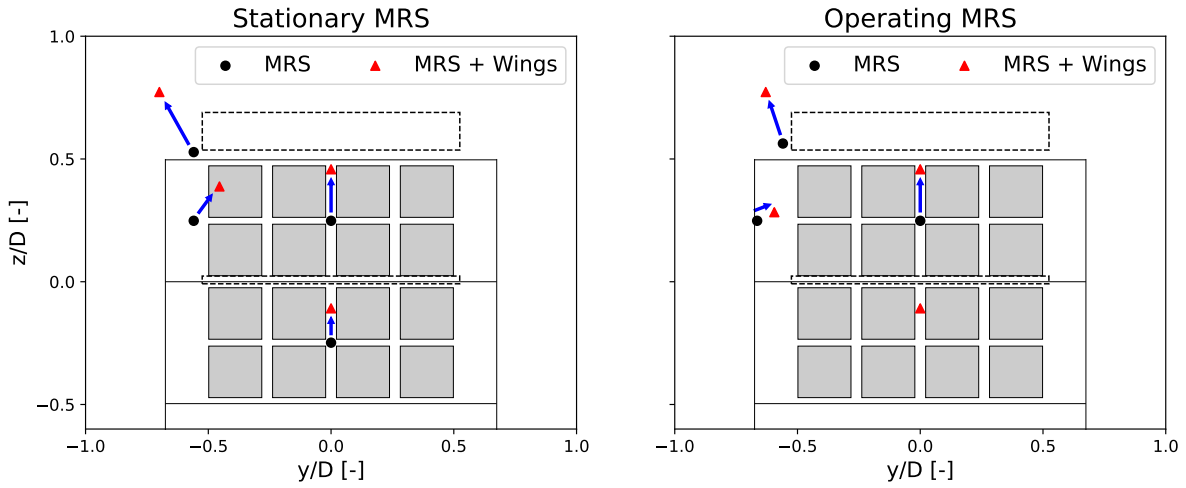

Figure 4.2: Graphical visualisation of the qualitative smoke visualisation results for the MRS without and with wings for the stationary MRS (left) and operating MRS (right) at $x/D = 1.1$.

Looking at Figure 4.2, first, the focus will be placed on the flow behaviour around the stationary MRS (on the left) to identify the effect of the external wings of the flow. When no wings are mounted the smoke streamtube is not significantly affected by the presence of the MRS, and the streamtube intersects with the downstream grid in the same region where it was injected into the flow for all four injection points (Figure 3.13). Mounting the wings on the stationary MRS, Figure 4.2 shows a

significant displacement of the streamtube for all four injection points. A difference can however be observed between the injection points around the centre of the MRS ($y/D = 0.0$), and the edge of the MRS. Near the centre of the MRS, the streamtube is significantly deflected vertically upwards because of the upwash induced by the wings. On the other hand, near the edge of the MRS, a similar vertically upward deflection is observed, combined with a lateral deflection as a result of the tip-vortices induced by the wings. This results in a contraction of the streamtube towards the MRS centre below the upper wing, and an outward movement of the streamtube above the wing, caused by the counter-clockwise rotating tip-vortex present on the left side of the MRS.
Moving the attention now to the effect of MRS operation on the flow around the system, hence comparing the left and right plot in Figure 4.2, primarily the blockage effect the MRS induces when the rotors are spinning becomes evident. For the clean MRS, it is observed that the flow along the centre, around $y/D = 0.0$, is not significantly affected by the rotating rotors. Near the edges of the MRS, the smoke streamtube is displaced laterally away from the turbine. This displacement is caused by the average expansion of the MRS wake and the increased amount of blockage induced by the MRS when the rotors are operating. Looking at the effect of MRS operation for the configuration with wings a similar behaviour is observed, where the streamtube around the MRS centre ($y/D = 0.0$) is not significantly affected, and the streamtube located near the edge of the MRS is displaced further away from the turbine centre. The displacements near the outer edge of the MRS are however less significant compared to when the MRS was stationary. This can be explained by the fact that MRS operation reduces the lift of the top wing, reducing its tip-vortex strength, thus reducing the displacement of the smoke streamtube. All in all these smoke visualisations provide a solid proof-of-concept, visualising that the presence of the high-lift wings could be beneficial for deflecting the wake and keeping the wake region more compact.

4.3. PTV Results

The results obtained through the PTV investigation will be presented and discussed in the following section. The section starts with a discussion of the velocity fields of the MRS with and without external wings at the different downstream locations. Here both the streamwise and in-plane velocity components will be treated. Subsequently, an analysis of the momentum fluxes in the near-wake follows. After the discussion of the momentum flux, the streamwise vorticity fields are presented and discussed, where in addition to this discussion, the lift of the external wings will be related to the circulation of the tip vortices. Finally, this section concludes with a discussion of the recovery of streamwise momentum and an analysis of the available power in the near-wake of the MRS. All PTV measurements have been taken at a freestream velocity of $U_\infty = 4.0\text{m/s}$, and a tip-speed ratio of $\lambda = 3.3$.

4.3.1. Velocity Fields

In the following section, the velocity fields of the MRS with and without wings are discussed. For the configuration without wings, velocity fields obtained for $x/D = 1.0$, 1.5, and 2.0 are presented, and for the configuration with wings, an additional velocity field is presented at $x/D = 2.5$. First, the streamwise velocity fields are discussed, after which the in-plane velocity magnitudes are presented. All velocity fields presented have been normalised by multiplying the velocity components by $1/U_\infty$, with $U_\infty = 4.0\text{m/s}$ being the free stream velocity.

Streamwise Velocity Fields

The streamwise velocity field for the near wake of the MRS configuration without and with external wings are presented in Figure 4.3 and Figure 4.4 respectively. Looking first at the clean MRS configuration, hence without wings as presented in Figure 4.3, a clear wake region with slow-moving air in the stream-wise direction can be identified. This wake region is concentrated behind the actuator surface and primarily expands laterally as the flow moves downstream. Although the wake expands laterally due to blockage induced by the MRS and its average expansion, the centre of the wake remains near the centre of the MRS, with the wake having a certain amount of symmetry around y/D=0.0.
Upon closer examination at x/D=1.0, it becomes apparent that each individual VAWT rotor, depicted by a square outline in the plot, generates its distinct wake region, thereby introducing a velocity deficit into the surrounding flow. Between these flow deficits regions of enhanced flow can be recognized, originating from the gaps between the rotors. These pockets of enhanced flow disappear as the wake becomes more uniform as it travels downstream. The velocity deficits induced by the individual rotors

do not travel downstream in a straight line, but the lateral deflection of the wake centre is skewed towards the side of the VAWT rotor which rotates upwind in the opposite direction of the freestream flow. This observation aligns with findings in the works of Ryan et al. [48], Huang et al. [29], and Rolin and Porté-Agel [47]. The phenomenon can be attributed to the vortex pair formed at the upwind-turning side of the rotors. Specifically, for the two shafts on the left, this occurs on the right side of the rotor, given their counter-clockwise rotation, while for the two on the right, it takes place on the opposite side due to their clockwise rotation. Travelling further downstream to x/D=1.5 and x/D=2.0 these individual wakes from rotors directly above each other gradually converge, moving towards each other until they merge into a unified wake. It is important to remind the reader that between the two top rows of rotors and the two bottom rows, a horizontal support structure is present, similar to the flat plates located above the top row of rotors and below the bottom row of rotors. The wakes appear to contract towards each other between these structures of the MRS frame, however, the wake of the two top rows of rotors does not seem to contract and merge as significantly with the wake region of the bottom two rows of rotors. Although it is uncertain what causes this, this effect could be attributed to the support structure of the MRS interfering with the tip vortices that are being shed from the rotors that dictate the shape of the wake, resulting in an asymmetric wake structure. A similar asymmetric wake behaviour was also found in the work of Ryan et al. [48], and Rolin and Porté-Agel [47]. In both studies, a VAWT was placed close to the ground, resulting in blockage of the tip vortex and an asymmetric vortex system and wake profile. Furthermore, from the velocity field at x/D=1.0 a velocity deficit can be identified near y/D=0.75, which moves laterally with the average expansion of the wake region. This flow deficit can be attributed to the vertical support structure of the MRS model.

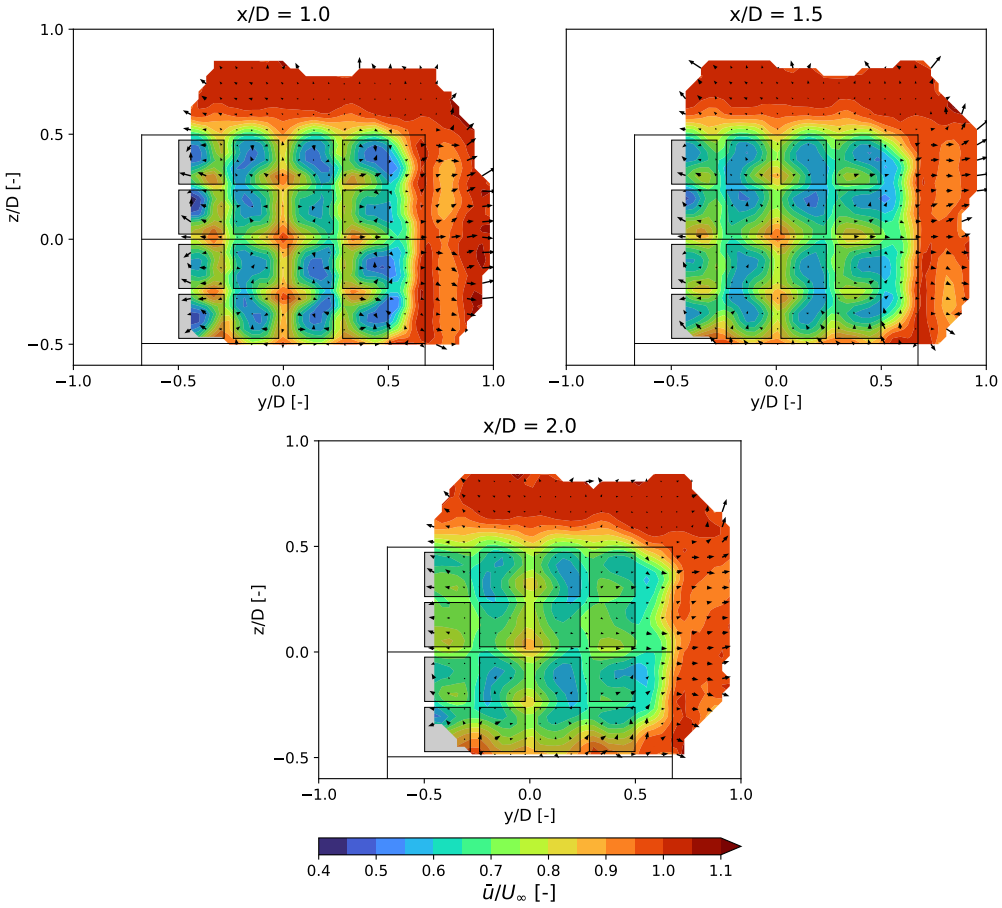

Figure 4.3: Contours of the normalised streamwise velocity of the MRS configuration without wings for x/D = 1.0, 1.5, and 2.0. Additionally, vectors are plotted to visualise the in-plane velocity. The two rotor shafts on the left rotate in the clockwise direction, and the two shafts on the right rotate in the counter-clockwise direction (as seen from the top).

Moving the attention now to the MRS configuration with wing, of which the streamwise velocity profiles have been plotted in Figure 4.4, an entirely different picture of the wake structure of the MRS is painted. The wake behaviour undergoes significant changes due to the presence of the wings, which introduce both an upwash into the flow and tip vortices at the wing tips. In the accompanying figure, the in-plane velocity vectors reveal a strong tip vortex near the wingtip mounted on top of the MRS frame. Additionally, a slightly weaker vortex originates from the mid-wing at x/D=1.0, where this mid-wing vortex deforms and merges into the wake region downstream. These tip vortices result in a lateral contraction of the wake region, leading to the wake region remaining much more centred behind the actuator surface compared to the MRS configuration without external wings. Contrary to the configuration without wings, the individual wake regions behind the rotors cannot be identified anymore. Instead of remaining centred behind the rotor, they are already significantly deformed at x/D=1.0. Looking at the wake that is being shed from the bottom row of rotors, it can be seen that it has moved upwards significantly, and instead of being located around the centre of the rotor ($z/D \approx -0.4$) now can be found near the gap between the two lower rows of rotors ($z/D \approx -0.3$). Looking at the wakes that are being shed by the rotors one row higher, one can observe that instead of a centred flow deficit behind the rotors, these wake profiles are being stretched and displaced in the vertical direction. This effect can be attributed to the presence of the mid-wing, where the tip vortex it sheds and the upwash it induces onto the flow deforms and displaces the wake profiles. The effect of the tip vortex of the mid-wing in particular can be observed at x/D=1.0 and 1.5 around y/D=0.5 where the wake profile of the rotor is deformed by the swirling motion of the vortex and high momentum flow is injected into the flow directly below the wing. The individual wake profiles introduced into the flow by the two upper rows of rotors are due to the upwash generated by the two wings hardly recognizable. At x/D=1.0 the wakes of the rotors located at the second row from the top can be identified near y/D=0.20 and 0.35 and z/D=0.4. The large flow deficit located at y/D=0.25 and z/D=0.8 appears to be the merged and deformed wake structure of the final row of rotors located on the upper row. Moving further downstream, hence looking at x/D=1.5 - 2.5, the individual wake structures that one could still recognize at x/D=1.0 start to merge, resulting in a single large area of flow deficit which is transferred in the vertical direction as it moves downstream as a result of the upwash induced by the wings.
Looking at the overall shape of the wake once again a certain degree of symmetry can be identified around y/D=0.0, similar to the case without wings. Furthermore, comparing the in-plane velocity vectors between the two MRS configurations, the in-plane velocity vectors of the case with wings are of much larger magnitude and exhibit significantly greater alignment compared to the MRS configuration without wings, where the in-plane velocity vectors are rather chaotic and of much lesser magnitude. This again can be attributed to the upwash induced by the external wings. In addition to that, similar to the no-wing case a few pockets of enhanced flow velocity can be recognized, in particular at x/D=1.0 and 1.5. These can be attributed to the gaps between the rotors and the blockage effect the MRS brings, accelerating the airflow. A comparable behaviour of the flow is observed in the work of Zanforlin and Nishino [74] and Vergaerde et al. [68], which both study the flow around a pair of VAWTs. In these works, a similar region of accelerated flow can be recognized in the near-wake behind the turbine pairs in between the individual wakes. As for the wake induced by the vertical support structure of the MRS, which can be recognised at y/D=0.7, instead of moving laterally away from the turbine due to the average expansion of the wake as was the case for the no-wing configuration, it is contracted laterally towards the low-speed wake region as a result of the tip vortices. To conclude, as a result of the upwash and tip vortices induced by the external wings, Figure 4.4 shows that the wake region is not only energized through the sides of the MRS but also via the gap which is present at the bottom of the system.

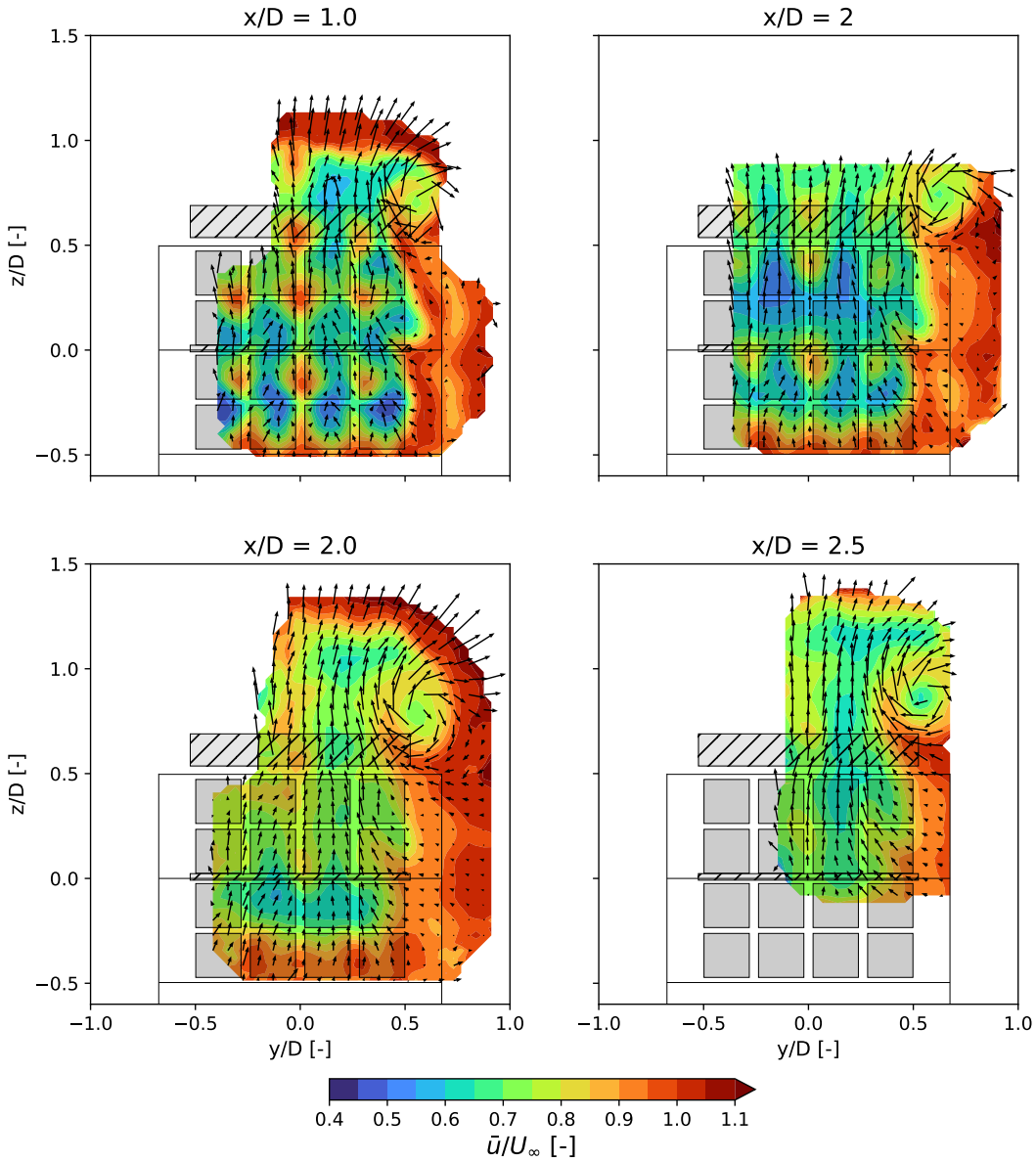

Figure 4.4: Contours of the normalised streamwise velocity of the MRS configuration with wings for x/D = 1.0, 1.5, 2.0, and 2.5. Additionally, vectors are plotted to visualise the in-plane velocity. The two rotor shafts on the left rotate in the clockwise direction, and the two shafts on the right rotate in the counter-clockwise direction (as seen from the top).

In-Plane Velocity Components

Due to the large difference in in-plane velocity magnitudes between the two MRS configurations, it is rather difficult to compare the horizontal and vertical velocity components v and w based on the vectors as presented in Figure 4.3 and Figure 4.4. This section will therefore shed some additional light on the magnitudes of in-plane velocities v and w. To do so, contour plots of the magnitudes of v and w have been plotted in Figure 4.5 for the no-wing configuration of the MRS and in Figure 4.6 for the MRS with wings.

For the MRS configuration without wings, it is observed in Figure 4.5a that patches of horizontal velocity exist in both positive and negative y-direction over the full wake region. The flow primarily moves away from the centre of the turbine (y/D=0.0), which can be attributed to the average expansion of the wake. Additionally, patches of flow are present that move in opposite directions (towards the centre of the MRS). These regions of flow primarily are found in a similar location to where the largest flow deficits in streamwise velocity u were found in Figure 4.3, and can be attributed to the tip vortices that are shed

from the individual rotors. These patches decrease in size as the flow travels further downstream and a more coherent flow structure emerges. Looking at the vertical velocity component in Figure 4.5b a similar, but much lower magnitude, chaotic flow pattern is observed with patches of flow moving in both positive and negative vertical directions in particular for x/D=1.0. As the wake travels downstream this behaviour seems to reduce, and the flow primarily remains stationary.

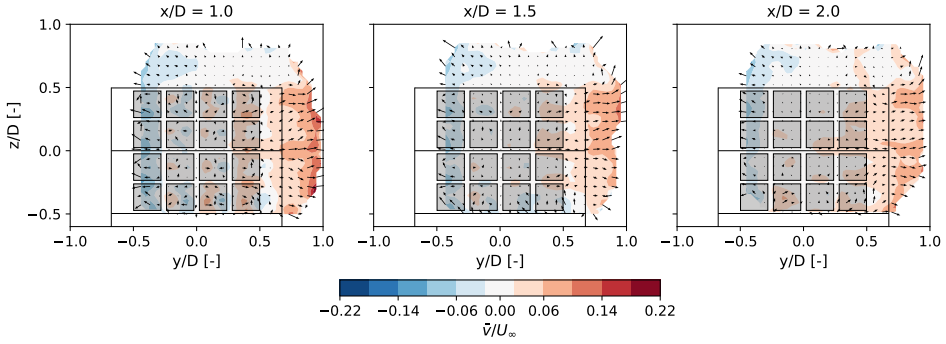

(a) Contours of the normalised horizontal velocity $\bar{v}/U_\infty$.

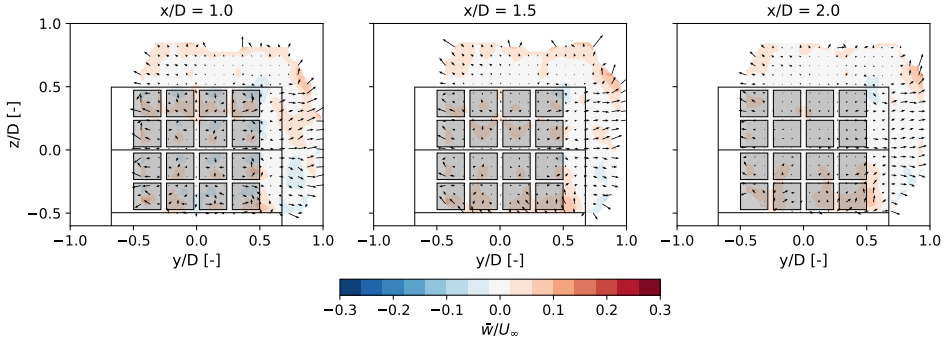

(b) Contours of the normalised vertical velocity $\bar{w}/U_\infty$.

Figure 4.5: Contours of the normalised in-plane velocities of the MRS configuration without wings for x/D = 1.0, 1.5, and 2.0.

Shifting the focus now to the MRS configuration with wings, where in Figure 4.6a the horizontal velocity v is plotted. In this figure immediately one can recognize the tip vortex of the top wing, and the horizontal velocity field this induces onto the flow field. As the wing generates a lifting force in the negative z-direction, a tip vortex in the clockwise direction on the right side of the wing is expected. This vortex induces a horizontal velocity component in the positive y-direction above the wing, and the negative y-direction below. This behaviour aligns with the observed results in the figure. Additionally, the mid-wing also introduces a tip vortex into the flow, but cannot directly be recognized in the figure as similar to the top wing it induces a velocity component in the positive y-direction above the mid-wing, and in the opposite direction below, but the stronger tip vortex of the top wing counteracts the component in the positive y-direction.
Looking at the overall flow field of horizontal velocities it can be seen that near y/D=0.0 the flow tends to move away from the centre of the turbine, which can be attributed to the rotational direction of the rotors, and the resulting tip vortices these rotors shed that dictate their individual wake shapes. Moving further away from the MRS centre, starting around y/D=0.10, the horizontal velocity component is oriented towards the centre of the turbine. A strong inward velocity component below the mid-wing is observed for x/D=1.0 which is a result of the combined effects of the two tip vortices of the top and mid-wing. However, above the mid-wing and around y/D=0.5 there is still a region of flow moving away from the turbine centre resulting from the two tip vortices of the top and mid-wing working in opposite directions in this region. Moving further downstream, this effect is reduced already at x/D=1.5 and non-recognizable anymore from x/D=2.0 onward as the stronger tip vortex of the top wing starts to dominate the flow field. As a result, the top vortices force high momentum flow into the wake region through the sides of the MRS.

Looking at the vertical velocity field w for the MRS with wing configuration in Figure 4.6b immediately the effects of the external wings can be seen. Behind the actuator surface and around its proximity, a strong upward velocity component is present as a result of the upwash that is induced into the flow by the external wings. This upward velocity component has its largest magnitude between the mid- and top-wing, and directly behind the top-wing. Additionally, similar to Figure 4.6a the tip vortices can be recognized by the strong up- and downward velocities components near the tips of the external wings. As the wake progresses downstream, the magnitude of the upwash appears to reduce gradually.

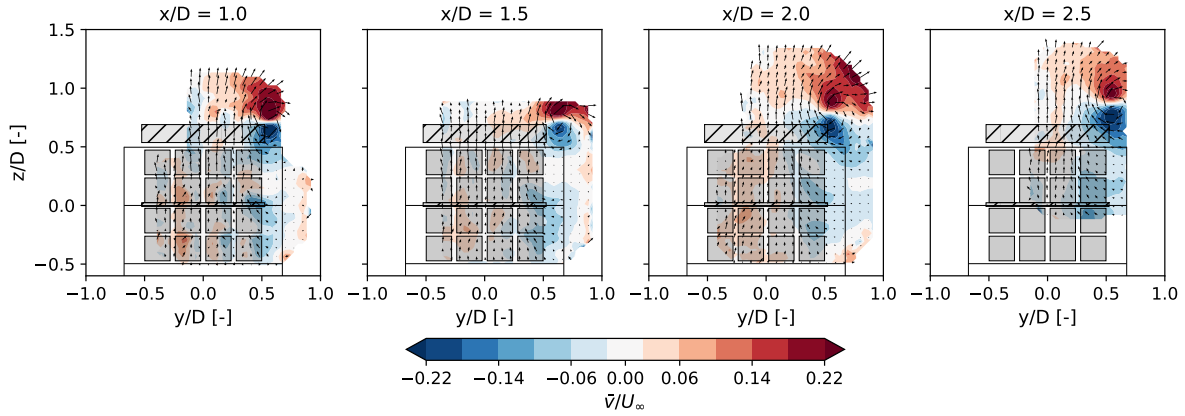

(a) Contours of the normalised horizontal velocity $\bar{v}/U_\infty$.

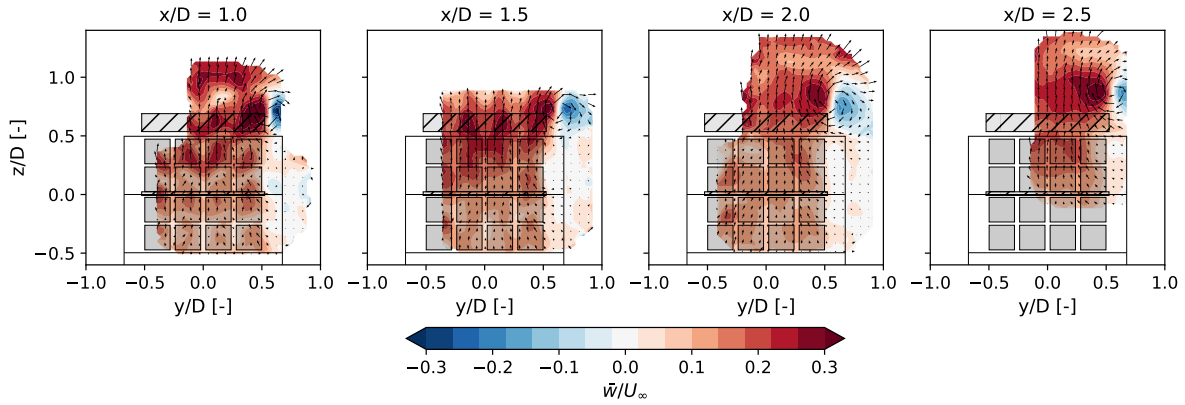

(b) Contours of the normalised vertical velocity $\bar{w}/U_\infty$.

Figure 4.6: Contours of the normalised in-plane velocities of the MRS configuration with wings for x/D = 1.0, 1.5, 2.0, and 2.5.

4.3.2. Mean Momentum Fluxes

The aim of installing the wings on the MRS frame is to enhance recovery of the wake region behind the MRS. For conventional wind turbines with zero yaw angle, wake recovery is dominated by turbulent momentum flux transferring energy from the outer flow regions to the wake region [17]. By having the wings mounted to the frame, the aim is to enhance the advection of high momentum flow into the wake region, by entraining this high momentum flow with the tip vortices originating from the wings. Additionally, the upwash induced by the wings is utilised to entrain the low momentum flow of the wake region and eject this to higher flow regions away from the actuator surface. To qualitatively visualise the effect of the external wings on the momentum convection within the wake of the MRS, the normalised velocity products $-\bar{v}\bar{u}/U_\infty^2$ and $\bar{w}\bar{u}/U_\infty^2$, representing the horizontal and vertical momentum fluxes, have been plotted in Figure 4.7. The velocity products have been defined in such a way that positive values show fluxes of momentum vertically upwards, and horizontally influxes towards the centre (y/D=0.0) of the MRS. To achieve this, the horizontal flux of momentum $-\bar{v}$ is used instead of $\bar{v}$.

For the MRS without wings, one can observe in Figure 4.7 that laterally momentum is transferred away from the turbine centre as a result of the average expansion of the wake region, and vertically only very little momentum transfer occurs in the wake at $x/D = 1.0$, which damps out as the flow travels downstream. Moving the attention to the MRS configuration with external wings, one can see that much larger fluxes of momentum are present in the wake region of the MRS. Similar to the velocity fields as presented earlier, and the vorticity fields which will be presented later in this chapter, the regions where the tip vortices are located can distinctly be identified as regions with large momentum flux. Furthermore, as a result of these tip vortices, a positive lateral influx of momentum towards the MRS centre (y/D=0.0) can be identified at all four downstream locations. This high momentum flow is entrained by the tip vortices of the wings and injected into the wake region through the sides. Moreover, the largest flux of momentum appears to originate from the upwash induced by the external wings. Figure 4.7 shows a strong flux of momentum for the MRS configuration with wings. As a result, low-momentum flow from behind the actuator surface is ejected upwards, promoting the influx of high-momentum flow through the sides and from below the MRS.

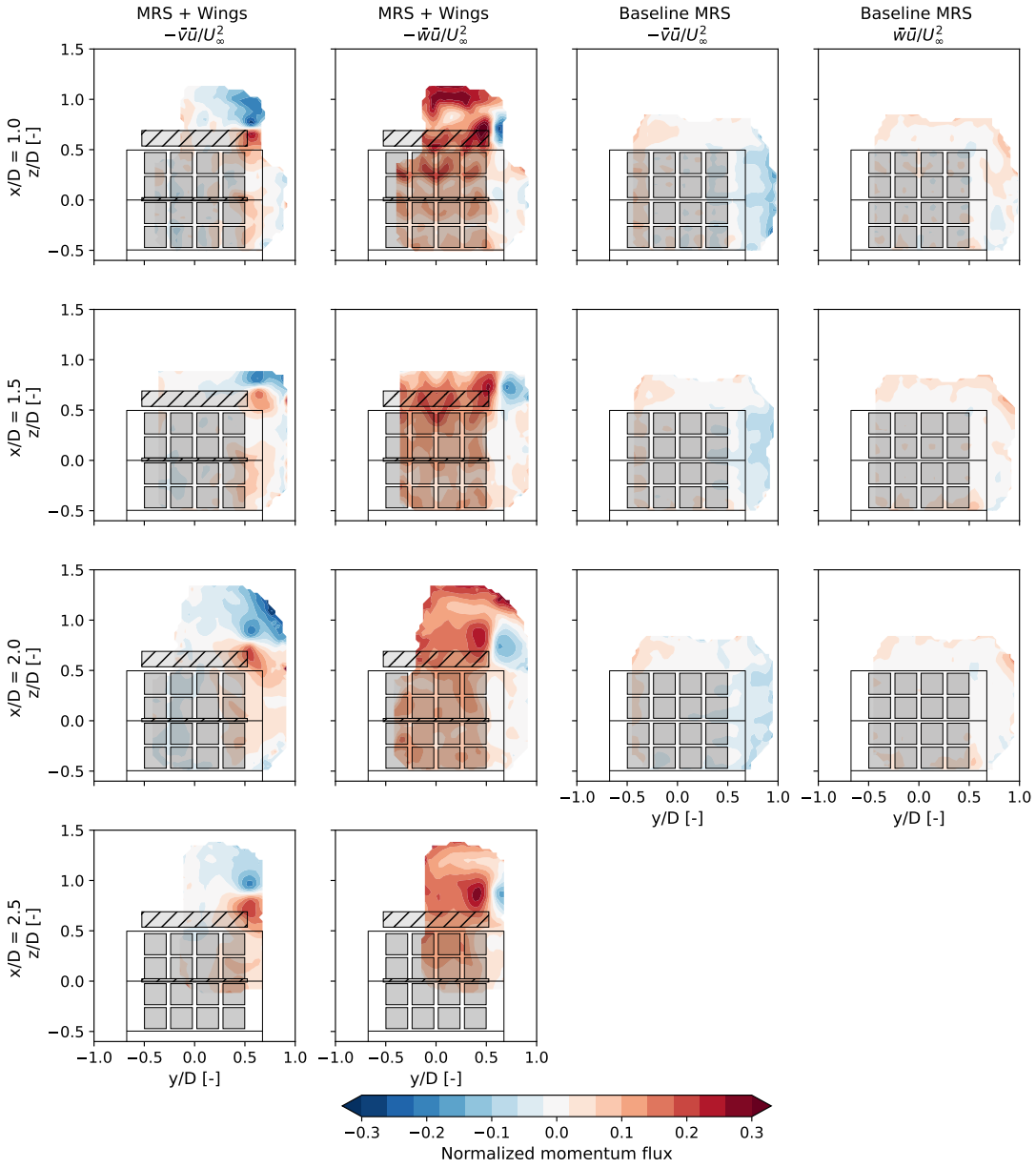

Figure 4.7: Normalised horizontal mean momentum flux $-\bar{v}\bar{u}/U_\infty^2$ and vertical mean momentum flux $\bar{w}\bar{u}/U_\infty^2$ for the MRS configuration with and without wings.

4.3.3. Streamwise Vorticity

The normalised streamwise vorticity for the MRS configuration with and without wings are displayed in Figure 4.8 and Figure 4.9 respectively. The streamwise vorticity plays a large role in the replenishment of momentum in the wake region as it promotes mixing of the wake region, and the injection of high momentum flow through the sides of the MRS by wake utilizing tip vortices introduced by the external wings on the corresponding MRS configuration. The vorticity ω_x has been normalised by multiplying it by D/U_∞ as is well-accepted in the literature (Rolin and Porté-Agel [47], Huang et al. [28]).
The main known source for vorticity for the case where no wing was mounted on the MRS, of which the vorticity fields are plotted in Figure 4.8, are the tip vortices that are shed from the tips of the rotors. This phenomenon in particular is visible at x/D=1.0 along $y/D \approx$0.35. Along this line, looking at the upper rotor and moving down, regions of alternating negative (counter-clockwise) and positive (clockwise) vorticity are found, originating from the vortex system being shed by the blades of the rotors. This behaviour is in line with the vortex structure as found in the work of Huang et al. [28] where they studied the vortex system originating from a single VAWT, and is the result of Helmholtz theorem which states a vortex filament cannot end in a fluid. A similar but opposite vortex system is identified at $y/D \approx$-0.35 and is the result of the two rotor shafts on the left side of the MRS rotating in opposite to the two shafts on the right. As the wake travels further downstream, regions of weaker vorticity merge with the regions of stronger vorticity, resulting in an overall wake region with weaker vorticity.

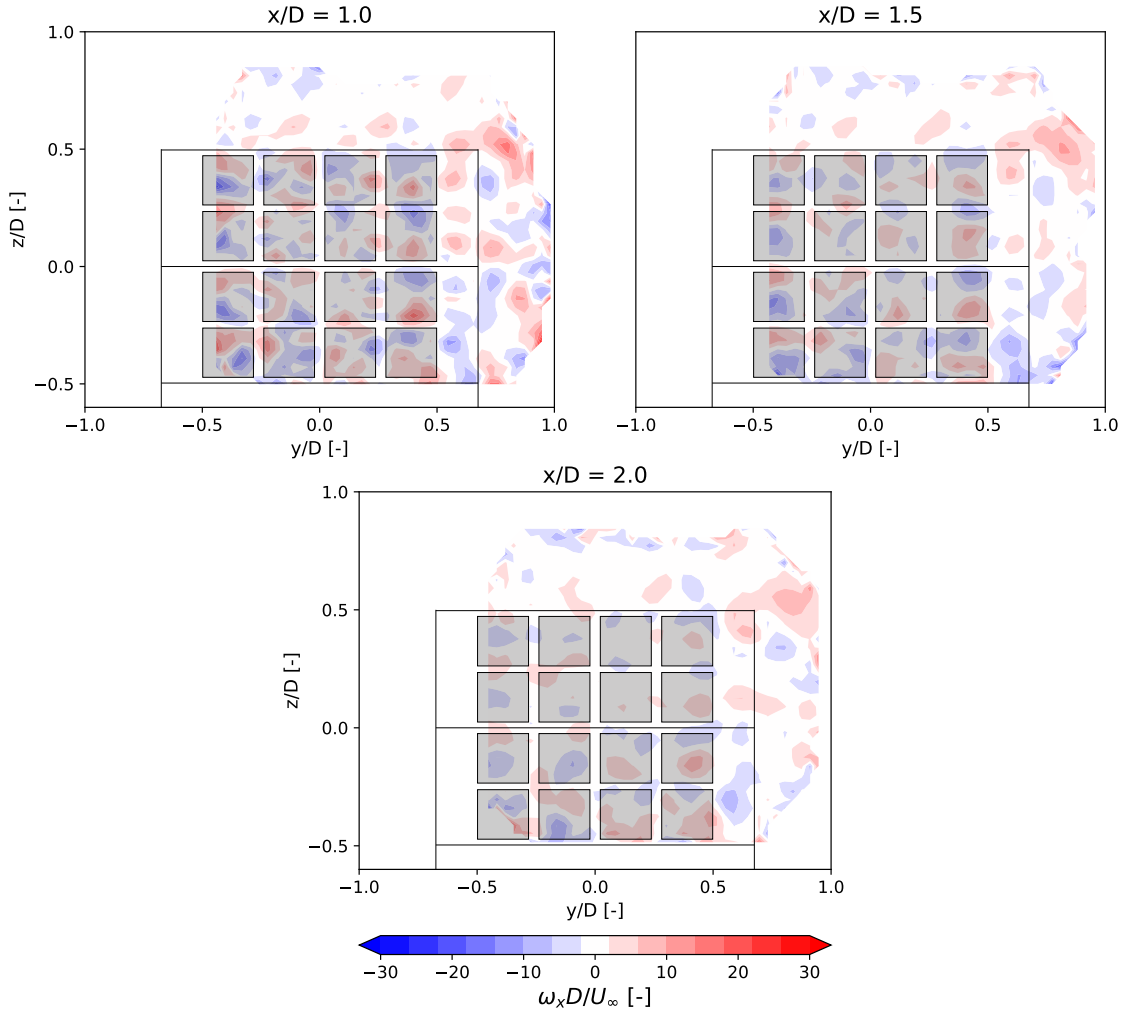

Figure 4.8: Contours of the normalised streamwise vorticity of the MRS configuration without wings for x/D = 1.0, 1.5, and 2.0. The two rotor shafts on the left rotate in the clockwise direction, and the two shafts on the right rotate in the counter-clockwise direction (as seen from the top).

A note must be made on the region of positive (counter-clockwise) vorticity found near the right upper corner of the MRS frame (y/D=0.75, and z/D=0.6). Although it is uncertain what exactly causes this region of vorticity, one theory could be that this behaviour is related to the blockage of the MRS. This blockage induces a vertical displacement of the flow, as is observed in Figure 4.5b, thus inducing a vertical velocity component. As a result, the flat plate which is part of the MRS frame, located around z/D=0.5, experiences a positive angle of attack, resulting in a suction side on the top side of the plate and a pressure side on the bottom, in turn introducing a counter-clockwise tip vortex into the flow at the edge of the frame.

The normalised streamwise vorticity field for the MRS with wing configuration, displayed in Figure 4.9, paints an entirely different picture. This vorticity field is not dominated by the individual tip vortices of the rotors, but rather is dominated by the strong tip vortices originating from the top and mid-wing, which can distinctly be identified at x/D=1.0 along the line of y/D=0.5. Here the tip vortex of the top wing is located around z/D=0.7, and that of the mid-wing around z/D=0.0-0.1. As both wings generate a force in the negative z-direction, they induce a vortex in the clockwise direction, which aligns with the negative vorticity as is observed in the plot. Furthermore, according to Prandtl's lifting line theory, as touched upon in the background section of this report, section 2.4, the wing generating the largest lift introduces the strongest vortex and thus the strongest region of vorticity into the flow. As the top wing generates more lift than the mid-wing, its region of vorticity is expected to be stronger, which indeed is confirmed by Figure 4.9. Another interesting aspect of this vorticity field, of which its behaviour is dominated by the tip vortices of the external wings, is that the patches of vorticity interact with each other, with the strongest region of vorticity primarily dominating this interaction. Looking at the evolution of the vorticity field as it moves downstream from x/D=1.0 to x/D=2.5 the overall vorticity field evolves with different patches of weaker vorticity merging and diffusing as the flow travels downstream. The region of vorticity originating from the top wing vortex however remains persistent, and in turn, strongly contributes to the overall structure of the wake. When a closer look is taken at the vorticity shed from the mid-wing, it can be observed that this is entrained by the stronger top-wing vortex. This region of vorticity not only experiences a rotational displacement around the top wing vortex but its vorticity patch is also stretched out as it moves downstream. Both these effects are a result of the complex interactions between the co-rotating vortex pair and are in line with what is described in the literature (Trieling et al. [65], Brandt and Nomura [12]). This behaviour shows that the evolution of the wake is not only dominated by advection but also by the interactions and entrainment effects of the tip vortices.

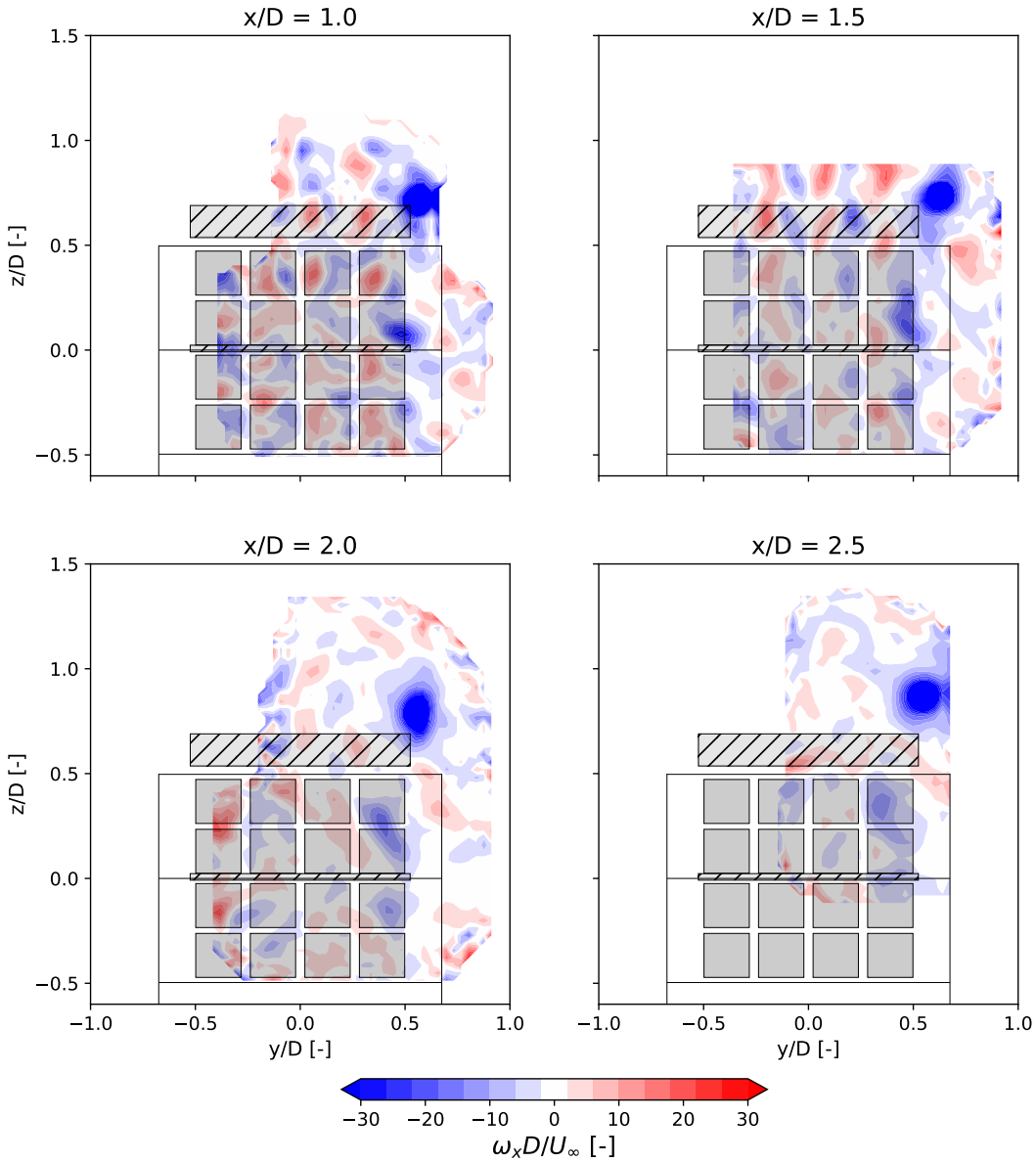

Figure 4.9: Contours of the normalised streamwise vorticity of the MRS configuration with wings for x/D = 1.0, 1.5, 2.0, and 2.5. The two rotor shafts on the left rotate in the clockwise direction, and the two shafts on the right rotate in the counter-clockwise direction (as seen from the top).

Tip-Vortex Circulation

From the introductory section on high lift wings in section 2.4, it was presented that theory relates the lift of the wing to the strength of its trailing tip vortices, which in turn drives the upwash behind the wing. In this section of the report, the circulation strength Γ of the wing and the tip vortices will be quantified, and the theoretical upwash based on the circulation strength will be compared to the actual upwash behind the wing. Two methods will be used to determine the circulation strength of the wing. The first method will make use of the lift generated by the wing, which is related to the circulation through Equation 2.23 by the Kutta-Joukowsky theorem. From this, the circulation can be determined by Equation 4.3. To obtain the circulation of the wing, the loads as reported in Table 4.2 are used, as these represent the loads the wing produces when the MRS is operating.

$$\Gamma = \frac{L}{\rho U_\infty b} \tag{4.3}$$

The second method will utilize the in-plane velocity field to determine Γ of the tip vortex of the top wing. The circulation of the trailing tip vortices can be determined by taking the closed contour integral around the vortex as given in Equation 4.4. This closed contour can be any arbitrary shape, as long as it encloses the core of the vortex. For this work two contours are considered, a circular contour and a square contour, both visualized in Figure 4.10. This figure shows a zoomed-in view of the vorticity field at $x/D = 1.0$ together with the in-plane velocity vectors, where the thin black lines delineate the outline of the upper right corner of the MRS and the right edge of the top wing. The contours around which the Γ integral is taken are indicated by the black square having sides of length $2r$, and the red circle having radius r. These contours are centred around point C which represents the centre of the vortex core, which is the location of minimum vorticity ω_x.

$$\Gamma = -\oint \vec{V} \cdot d\vec{s} \tag{4.4}$$

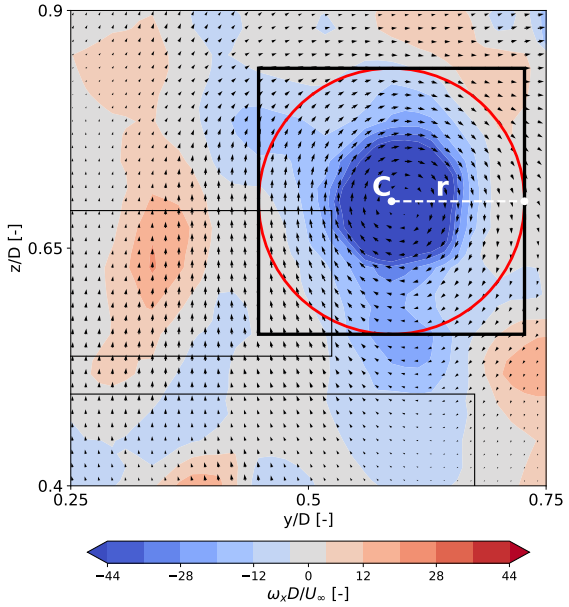

Figure 4.10: Visualisation of the circular and square Γ-integration window at $x/D = 1.0$.

The integration of the velocity field is performed over a range of r-values until a consistent circulation strength is achieved. Results of Equation 4.4 for $x/D = 1.0$ and $x/D = 2.0$ are displayed in Figure 4.11. These results show that circulation strength Γ increases as r increases, until at a given r a maximum Γ strength is obtained. This behaviour aligns with the expectations. Additionally, it can be observed that at $x/D = 1.0$, Figure 4.11a, a slightly lower maximum Γ is obtained compared to $x/D = 2.0$, Figure 4.11b. As one is dealing with a rather complex flow, it is difficult to pinpoint the exact reason for this discrepancy. Multiple factors could be at play causing this mismatch of Γ strengths, such as vorticity originating from the frame or the rotors.

The circulation strengths Γ, obtained through both the load measurements and the velocity integration, have been reported in Table 4.3. These circulation strengths in turn can be converted to lift coefficients through Equation 4.5, which as a result of the selected freestream velocity ($U_\infty = 4.0$m/s) and chord length of the wing ($c = 0.5$m) equates to be equal to Γ. From the values in this table a mismatch is found between the Γ obtained through load measurements and the velocity integration. This mismatch can be explained by the fact that the velocity field used to compute Γ through Equation 4.4 is not only dictated by the vortex core of the top wing but is also influenced by other flow structures originating from the MRS frame and the rotors. Additionally, as one deals with viscous flow, a certain portion of energy gets dissipated, resulting in a reduction in velocity magnitude, reducing the obtained circulation value.

$$C_L = \frac{2\Gamma}{U_\infty c} \tag{4.5}$$

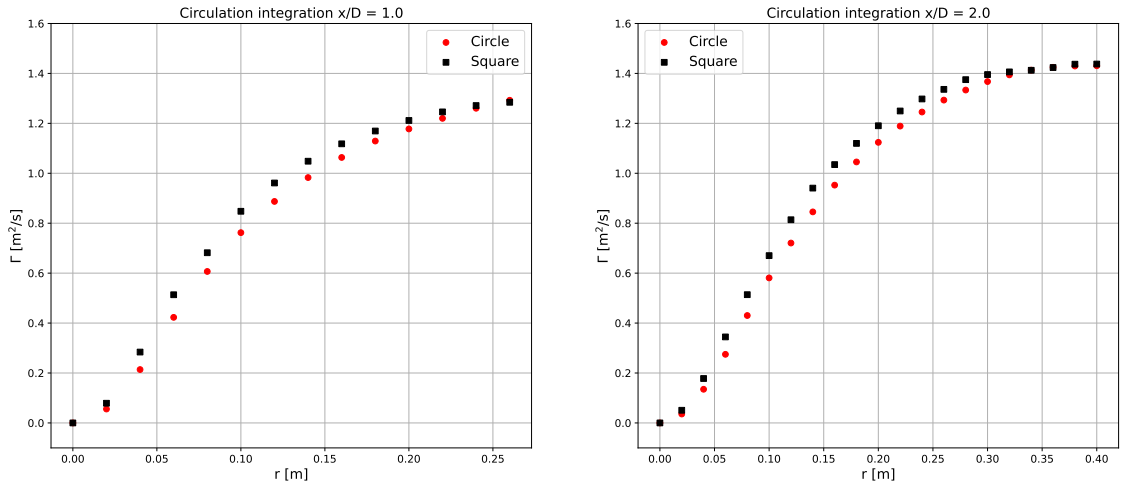

(a) Circulation strength Γ as function of r at $x/D = 1.0$.

(b) Circulation strength Γ as function of r at $x/D = 2.0$.

Figure 4.11: Evaluation of circulation strength Γ as a function of the integration window size.

Converting these circulation values to the lift coefficient it becomes evident that a lower C_L is found for the top wing than what was obtained for the isolated wing, which gave $C_L = 1.97$. This reduction in C_L can be explained by the blockage introduced by the MRS, which not only reduces flow velocity at the wing surface, negatively affecting the lift, but also causes an upwash in the flow reducing the perceived angle of attack of the wing, reducing the lift generated further.

Table 4.3: Circulation around the wing obtained through load measurements and velocity field integration.

x/D	Γ load measurements [m^2/s]	Γ Velocity integration [m^2/s]
1.0	1.62	1.28
2.0	1.62	1.44

In section 2.4, it was also discussed that the circulation around a wing can be related to the upwash generated behind this wing through Equation 2.22. In Figure 4.12 the expected upwash along the wing according to Equation 2.22, based on the circulation obtained from the load measurement and velocity integration, have been plotted for $x/D = 1.0$ and $x/D = 2.0$. These plots show that a larger upwash is induced for a stronger Γ. Additionally, it becomes clear that as one moves towards the wing tip, the induced upwash tends to infinity. This effect can be explained by the fact that in the current analysis, a constant Γ is assumed over the entire wing, however from the discussion in section 2.4 it is known this is not the case in the real world. For the actual wing, Γ is not constant over the entire span but rather distributed over the wing, where $\Gamma \rightarrow 0$ as one approached the wingtip. With the methods employed in this section, it is not possible to obtain the Γ distribution over the wing, and therefore one should keep this discrepancy in mind.
The projected upwash from the circulation has also been compared to vertical velocity values obtained through the PTV measurements. The green circles in Figure 4.12 represent the vertical velocity values at discrete spanwise wing locations vertically aligned with the vortex core, whereas the purple triangles represent the vertical velocity aligned with the centre of the wing. Comparing the theoretical upwash acquired through Equation 2.22 with the actual upwash it can be concluded that Equation 2.22 gives a good approximation, where the largest difference starts to occur as one gets closer to the wing tip, explained by the assumption of having a constant Γ along the span of the wing. Differences between the projected and actual upwash therefore originate from the assumption of constant Γ along the wing span, but also from interference effects between the top wing and mid-wing, and blockage introduced by the MRS frame and rotors.

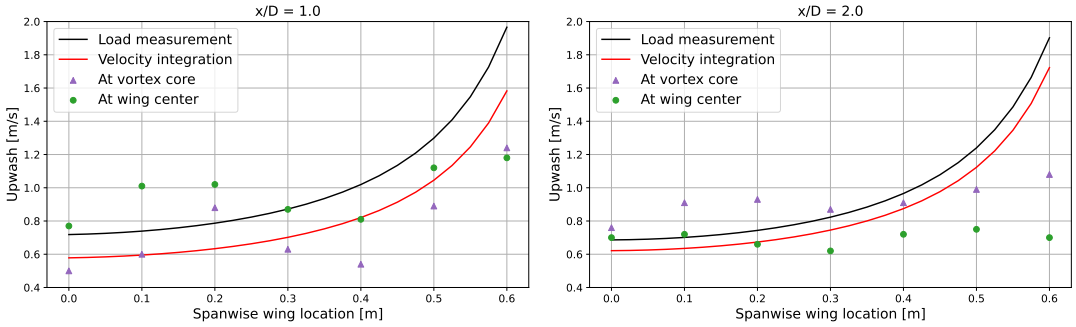

(a) Upwash along the span of the wing at $x/D = 1.0$ based on Γ-strength compared to actual upwash.

(b) Upwash along the span of the wing at $x/D = 1.0$ based on Γ-strength compared to actual upwash.

Figure 4.12: Comparison of the anticipated upwash along the span of the top wing based on Γ-strength acquired through load measurements and velocity integration compared to actual upwash values along the span of the wing.

4.3.4. Streamwise Momentum Recovery

In Equation 4.6 the rearranged Reynolds averaged Navier-Stokes equation for the streamwise direction is presented, which is analysed to study the difference in streamwise momentum recovery between the two MRS configurations. In the equation, u, v, and w represent the streamwise, lateral, and vertical velocity components in x, y, and z direction. Similar methods have been used in the work of Huang et al. [28], Bossuyt et al. [10], and Boudreau and Dumas [11].

$$\underbrace{\bar{u}\frac{\partial \bar{u}}{\partial x} = -\bar{v}\frac{\partial \bar{u}}{\partial y} - \bar{w}\frac{\partial \bar{u}}{\partial z}}_{\text{advection}} \underbrace{-\frac{1}{\rho}\frac{\partial \bar{p}}{\partial x}}_{\text{pressure}} \underbrace{-\frac{\partial \overline{u'u'}}{\partial x} - \frac{\partial \overline{u'v'}}{\partial y} - \frac{\partial \overline{u'w'}}{\partial z}}_{\text{Reynolds stress}} \tag{4.6}$$

On the left-hand side of this equation the streamwise advection term is presented, whereas on the right-hand side, the terms contributing to streamwise recovery are displayed. The streamwise recovery of momentum is driven by 3 main components, advection, pressure, and Reynolds stresses, each of which has been underlined in the equation. For the current analysis, the Reynolds number is considered high enough to neglect viscous terms ($Re_d = 0.8 \times 10^5$, based on the rotor diameter d). Furthermore, as the pressure term was not measured during the measurement campaign, this will be left out of the analysis.

The measured RANS terms at x/D=1.0, 1.5, and 2.0 for the MRS without external wings are displayed in Figure 4.13, and those for the MRS with wings in Figure 4.14. Here, the contours in the figures represent the full terms as stated in the equation (including minus sign), hence positive (red) regions contribute positively to wake recovery, and negative (blue) regions have a negative contribution to the streamwise momentum recovery. Each term has been normalized by dividing its value by the maximum overall value of $\bar{u}\frac{\partial \bar{u}}{\partial x}$ at that specific x/D-location. The value of $\frac{\partial \bar{u}}{\partial x}$ has been acquired through a finite difference evaluation (forwards and backwards) for x/D=1.0 and 2.0. For x/D=1.5, $\frac{\partial \bar{u}}{\partial x}$ is calculated through a second-order polynomial regression using $\bar{u}$ at the three downstream locations, following the work of Huang et al. [28] and Bossuyt et al. [10]. Normalizing the data in this way allows the identification of the main contributors to the redistribution of the streamwise momentum in the wake based on a relative comparison of the momentum budget.
First, a look is taken at the horizontal advection of streamwise momentum, visualised in the first column of both figures. Looking at the distribution at $x/D = 1.0$, one can see that for the MRS without wings, relatively strong regions of positive horizontal advection are found behind the actuator surface. These regions are in a similar location at the patches of vorticity as found in Figure 4.8, which were attributed to the vortices of the rotor blade tips. In the region where the edge of the wake can be found, as also defined in Figure 4.5b, a strong region of negative advection can be found, for which the outboard movement of the wake due to its expansion is responsible. As the wake travels downstream, the regions of positive horizontal advection reduce in strength, but the negative region due to wake expansion remains as this expansion dominates the behaviour of the wake. Moving the focus to the MRS with wing configuration, one can see that strong positive regions of horizontal advection originating from the tip

vortices of the external wings primarily contribute to positive redistribution of streamwise momentum in the wake region. This effect remains as the wake travels downstream up to x/D=2.0.
Shifting the focus now to the vertical advection term, visualised in the second column of the figures, an overall lesser effect on the redistribution of streamwise momentum is found for the MRS without wings. Similar patches of enhanced advection are found at the regions of high vorticity originating the rotor blade tip at x/D=1.0, similar to the horizontal advection term but of lesser strength. Additionally, a strong positive contribution to the redistribution of streamwise momentum is found near the lower corners of the actuator surface, in particular at x/D=1.5. This is primarily due to the contraction of the wake in this region as a result of the tip vortices shed by the rotor blades resulting from their rotational direction. For the MRS configuration with wings, the vertical advection term contributes strongly to the redistribution of momentum in the wake and appears to be the primary term contributing to this redistribution of streamwise momentum. This can primarily be attributed to the upwash induced by the external wings and is sustained up to at least x/D=2.0.
Finally, comparing the Reynolds stress between both MRS configurations displayed in the two rightmost rows of Figure 4.13 and Figure 4.14, it is observed they have a similar but much less significant contribution to the redistribution of the streamwise momentum for both. From this comparison, one can conclude that the redistribution of streamwise momentum in the wake of the MRS is dominated by advection for both MRS configurations. However, having the external wings mounted, the advection of momentum in the wake is enhanced, in turn promoting the redistribution of streamwise momentum in the wake compared to the MRS without external wings.

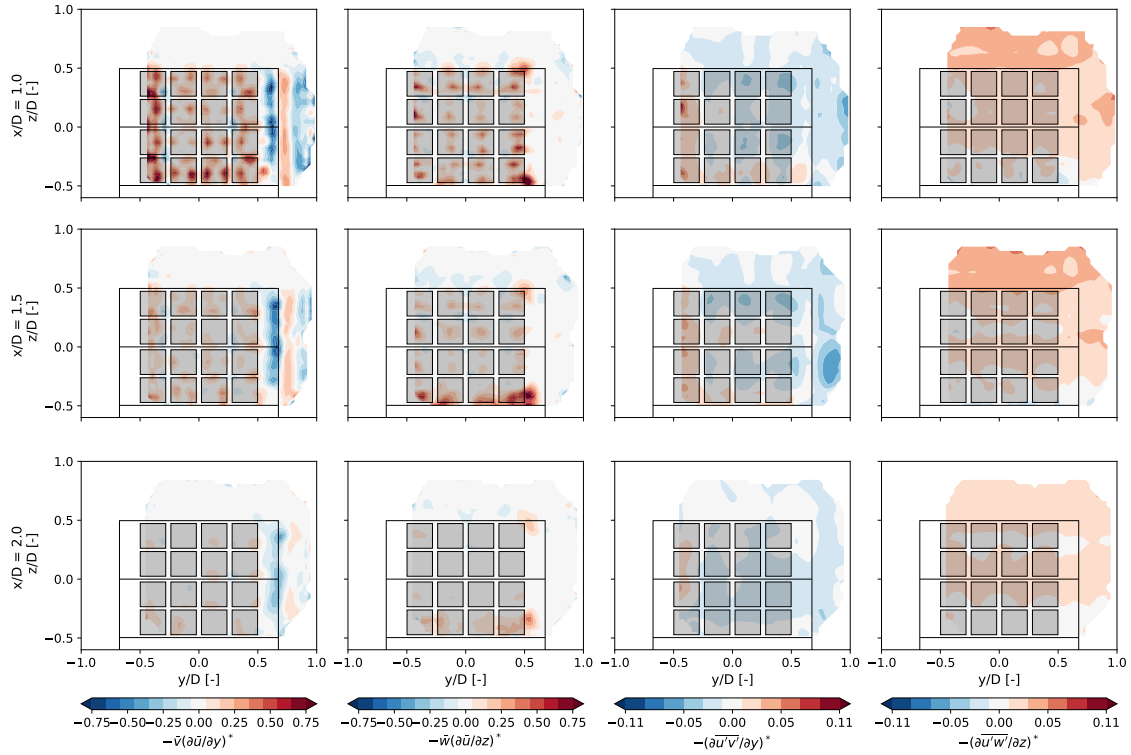

Figure 4.13: Measured terms of the RANS equation in the streamwise direction for the MRS configuration without wings at x/D = 1.0, 1.5, and 2.0. Each term has been normalized by the maximum value of $\bar{u}\frac{\partial\bar{u}}{\partial x}$, as denoted by *.

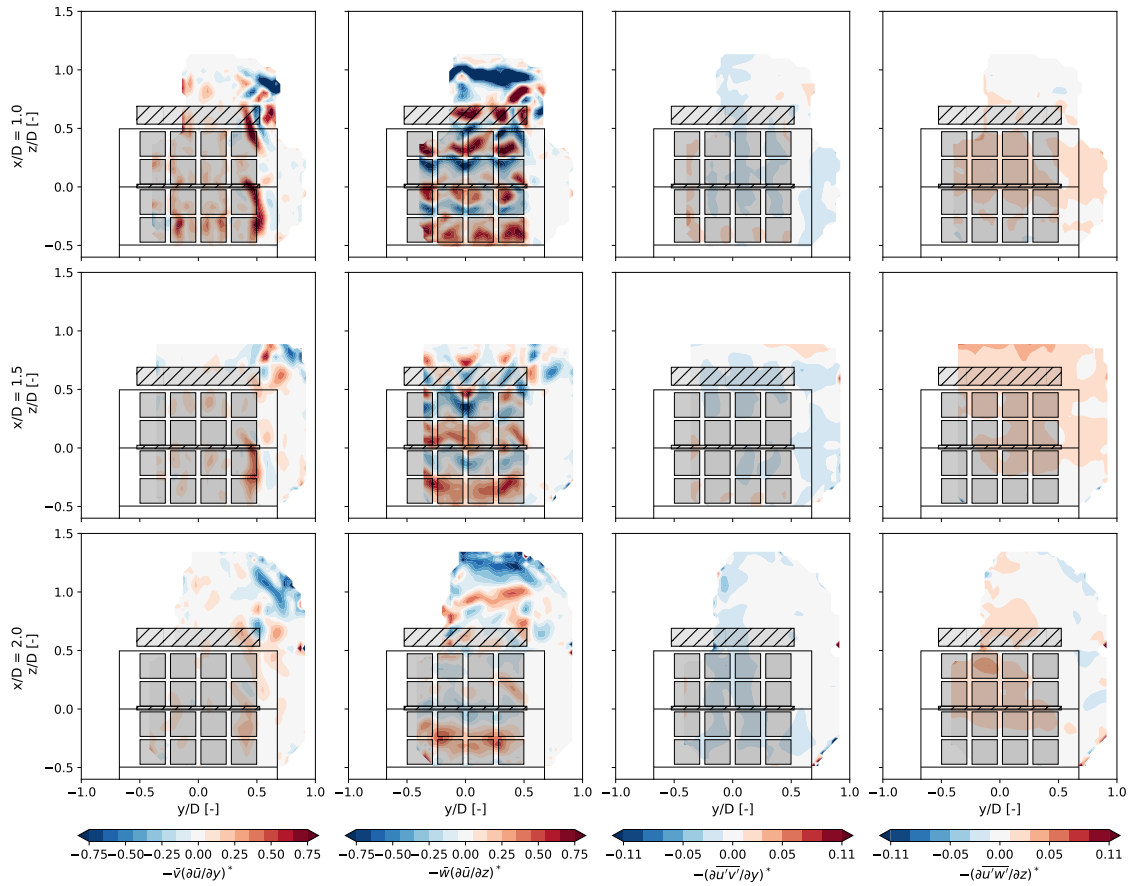

Figure 4.14: Measured terms of the RANS equation in the streamwise direction for the MRS configuration with wings at x/D = 1.0, 1.5, and 2.0. Each term has been normalized by the maximum value of $\bar{u}\frac{\partial\bar{u}}{\partial x}$, as denoted by *.

4.3.5. Power Recovery

As briefly touched upon in the background chapter of this report, the power available in the wind is dictated by the cube of the freestream velocity. As the MRS extracts power from the flow, a wake region is inflicted, resulting in a region with diminished velocity and therefore a reduction in available power within this region. By mounting the external wings on the frame, the aim is to enhance the recovery of power in the wake, maximizing available power for potential downstream turbines. To assess the impact the external wings have on the power recovery within this MRS wake, the normalized deficit of velocity cubed downstream of the MRS, $\left\langle \frac{\bar{u}^3}{U_\infty^3} \right\rangle$, is analyzed. This metric is achieved through evaluating the integral in Equation 4.7, and has been computed for both MRS configurations at all three downstream locations. The integral is evaluated over a region, indicated by the black dashed rectangle in Figure 4.10, covering half of the actuator surface ($y/D \geq 0.0$), with $S = \frac{1}{2}DH$ representing its area, following the approach of Huang et al. [28]. Due to limited data, only half the MRS is considered. Nevertheless, the previously validated assumption of wake symmetry supports the validity of this approach.
To assess the width of the wake region, the integration is also performed for a translating rectangle in the positive y/D direction. Here, y_0 represents the left-most non-dimensional edge of this translating region, normalized by the actuator surface width D. The translating window is depicted in Figure 4.15, where the dotted rectangle represents the region directly behind the MRS. The solid white rectangle indicates the translating integration window positioned at a distance y_0 from the MRS centre.

$$\left\langle \frac{\bar{u}^3}{U_\infty^3} \right\rangle (x_0, y_0, z_0) = \frac{1}{S} \iint_S \frac{\bar{u}^3}{U_\infty^3} dA \tag{4.7}$$

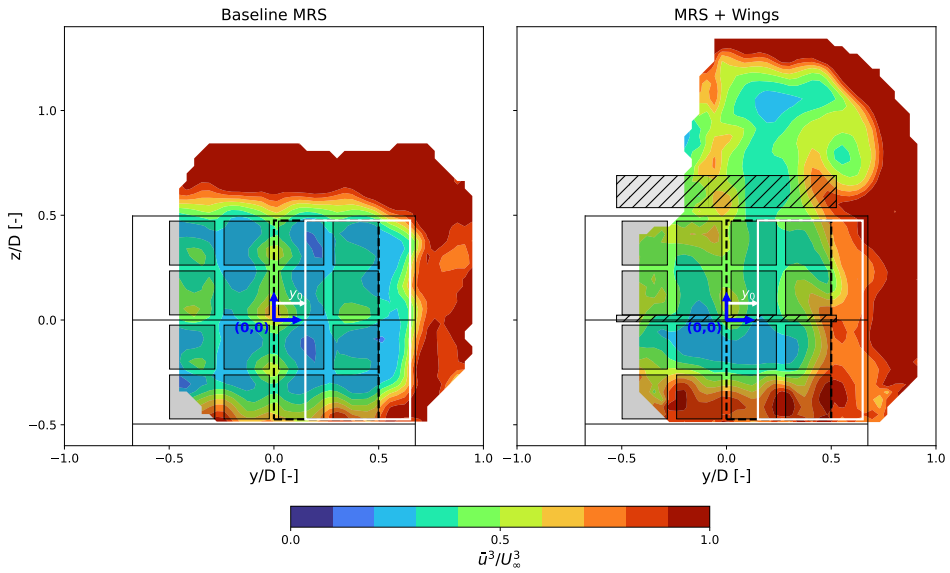

Figure 4.15: Visualisation of the normalized deficit of velocity cubed $\tilde{u}^3/U_\infty^3$ at x/D=2.0, and the integration windows used to compute $\left\langle \frac{\tilde{u}^3}{U_\infty^3} \right\rangle$.

Results for $\left\langle \frac{\tilde{u}^3}{U_\infty^3} \right\rangle$ directly downstream of the actuator surface for both MRS configurations are presented in Table 4.4. From this table, it becomes evident that the wake region behind the MRS with wings recovers faster than the baseline configuration, as $\left\langle \frac{\tilde{u}^3}{U_\infty^3} \right\rangle$ is larger at all three downstream locations. Furthermore, a large enhancement in wake recovery is found from x/D=1.5 to x/D=2.0 for the MRS configuration with wings as $\left\langle \frac{\tilde{u}^3}{U_\infty^3} \right\rangle_{\text{Wing}}$ recovers in this region from 0.36 to 0.49 compared to 0.33 to 0.34 for the MRS without wings. This enhanced recovery is attributed to the increased advection in the wake region of the MRS with wings. A noteworthy observation is the slight dip in $\left\langle \frac{\tilde{u}^3}{U_\infty^3} \right\rangle$ for both configurations from x/D=1.0 to x/D=1.5. This dip is associated with regions of enhanced flow velocity around y/D=0.0, a consequence of the gaps between the rotors. As the wake evolves, these high-velocity regions diminish, resulting in a reduction of flow velocity in this region. While this behaviour for the baseline MRS is attributed to the expansion of the wake, the wake of the MRS with wings undergoes lateral contraction due to the influence of the tip vortices as a result of which these high-velocity regions disappear.

Table 4.4: $\left\langle \frac{\tilde{u}^3}{U_\infty^3} \right\rangle$ downstream of the actuator surface of the MRS for the configuration without and with wings.

x/D	$\left\langle \frac{\tilde{u}^3}{U_\infty^3} \right\rangle_{\text{Baseline}}$	$\left\langle \frac{\tilde{u}^3}{U_\infty^3} \right\rangle_{\text{Wing}}$
1.0	0.35	0.38
1.5	0.33	0.36
2.0	0.34	0.49

Figure 4.16 shows $\left\langle \frac{\tilde{u}^3}{U_\infty^3} \right\rangle$ for the translated integration window at the three downstream locations for both MRS configurations. Several observations can be made from this figure. Firstly, the MRS with external wings has enhanced velocity recovery at all evaluated locations. Looking at the evaluation of the configuration without wing, a slight dip in $\left\langle \frac{\tilde{u}^3}{U_\infty^3} \right\rangle$ can be observed, with the metric reaching its minimum value for y_0=0.05. This dip in available power can once again be attributed to the regions

of enhanced streamwise velocity near y/D=0.0. As the wake moves downstream this dip in $\left\langle \frac{\bar{u}^3}{U_\infty^3} \right\rangle$ decreases, which also is in line with the observations in Figure 4.5b, as the wake becomes more uniform as it travels downstream. Looking at the performance of the MRS with wings, no such dip is found in $\left\langle \frac{\bar{u}^3}{U_\infty^3} \right\rangle$, showing that this configuration is much more effective at keeping the wake centred behind the actuator surface. Moreover, whereas the lateral recovery in the wake for the configuration without wing takes place rather gradually, somewhat of a step improvement in $\left\langle \frac{\bar{u}^3}{U_\infty^3} \right\rangle$ is found for the MRS with wings between y_0=0.05 and 0.10. This effect can once again be attributed to the region of enhanced flow near the centre of the MRS. Due to the narrow wake profile of the MRS with wing, the integration window starts to take into account freestream flow from y_0=0.05 onwards. However, at this point, it also overlaps with the region of enhanced flow near y/D=0.0 as discussed earlier. This region of enhanced flow near the centre ends around y/D=0.10, and from this point onwards the integration window finds only high power flow on its rightmost part, resulting in a decreased lateral recovery rate of $\left\langle \frac{\bar{u}^3}{U_\infty^3} \right\rangle$.
One important note on these results, which offer insights into the quantifiable aspects of wake recovery, is that they may not capture the full potential of the MRS with wings. At the measured downstream locations, the wake of the baseline configuration is still expanding, whereas the wake of the MRS with wings is still being contracted and advected upwards. This suggests a positive contribution of the wings to wake recovery by deflecting the slow-moving air. Nonetheless, these findings indicate an ongoing wake-development process. Further downstream analysis is necessary to confirm further potential power gains.

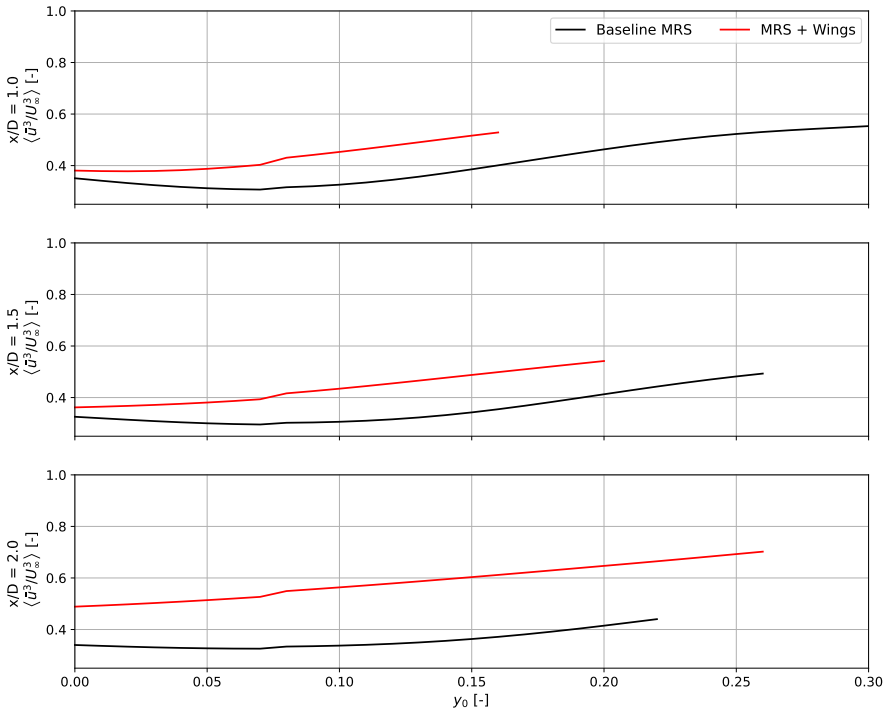

Figure 4.16: Available power coefficient $\left\langle \frac{\bar{u}^3}{U_\infty^3} \right\rangle$ at different y_0 locations for x/D= 1.0, 1.5, and 2.5 for the baseline MRS configuration and the MRS configuration with external wings.

5

Conclusions and Recommendations

The current chapter will conclude this work by presenting the main findings in section 5.1 and answering the research questions as presented in section 2.6. Additionally, since the territory of the VAWT-based MRS is still relatively uncharted, several recommendations for future research are outlined in section 5.2.

5.1. Conclusions

The present work has served as a proof of concept for the VAWT-based MRS, intending to gain an initial insight into the intricate near-wake dynamics of such a novel system. Additionally, the concept of wake deflection through external lift-generating devices has been studied as the MRS provides a suitable platform for such devices. To gain insight into the performance and near-wake dynamics of the MRS with and without external wake deflection devices a wind tunnel model was developed, and a wind tunnel study has been performed in the OJF of the TU Delft. Both load measurements and tomographic PTV have been employed to gather data and provide an initial look into these concepts. In the following section, the main findings of this work are presented by answering the research questions posed in section 2.6.

What are the flow field characteristics of the near wake of a VAWT-based MRS?

Which flow structures can be identified in the near-wake of the VAWT-based MRS?

In the near-wake of the VAWT-based MRS, PTV measurements have visualised a symmetric wake around the centre of the turbine, where clear streamwise velocity deficits behind each individual rotor are recognized. In between these individual rotor wake regions, pockets of enhanced flow are identified. These regions of enhanced flow are attributed to the physical gaps between the individual rotors. The primary source of vorticity in the near-wake of the MRS without external wings originates from the trailing vortices of the rotor blades.

How does the evolution of these identified flow structures contribute to the overall development of the near-wake in the streamwise direction?

As the wake travels downstream from x/D=1.0 to x/D=2.0 the individual wake regions are found to merge, creating a single large region of slow-moving air, where the regions of enhanced flow disappear as the wake evolves. During this process, the velocity deficits behind the individual VAWT rotors were found to deflect laterally towards the windward side of their corresponding rotors, resulting in the wake laterally expanding. Additionally, the wake regions of vertically stacked rotors are found to contract towards each other. As the wake progresses, weaker vorticity regions are found to merge with stronger regions, resulting in a reduction of overall vorticity in the wake.

How does the addition of external lift-generating devices affect the near wake of the VAWT-based MRS?

Which flow structures can be identified in the near-wake of the VAWT-based MRS with external lift-generating devices?

The presence of the external lift-generating wings on the MRS frame drastically alters the identifiable structures of its near-wake. Similar to the MRS without wings the wake is symmetric around the centre of the turbine. The presence of the external lift-generating wings, however, introduces strong regions of vorticity induced by their tip vortices. Additionally, these tip vortices together with the bound vortices of the wings induce a strong upwash into the flow. As a result, the wake is laterally contracted, and the flow deficits behind the individual rotors are vertically elongated and deflected upwards. The primary source of vorticity in the near-wake of the MRS with external wings originates from the tip vortices of the external wings.

How does the evolution of these identified flow structures contribute to the overall development of the near-wake in the streamwise direction?

As the wake progresses from x/D=1.0 to x/D=2.5, the region of vorticity induced by the top wing remains persistent and is found to dominate the evolution of the wake. As a result, instead of the wake laterally expanding as was the case for the MRS without external wings, the tip vortices of the wings cause the wake region to laterally contract by feeding it with high moment flow through the sides. Consequently, the wake profile at x/D=2.0 is significantly narrower than that of the MRS without external wings. Additionally, the induced upwash vertically advects the slow-moving wake region upwards, away from the MRS centre. By doing so the wake region near the bottom of the MRS is also energised with high momentum flow. The evolution of the wake is therefore not solely driven by advection, but also by the interaction and entrainment effects of the tip vortices of the external wings.

What is the correlation between the presence of external lift-generating devices and the momentum and power recovery of the near-wake in the streamwise direction?

Analysis of mean momentum fluxes and streamwise momentum recovery reveals a positive correlation between the presence of external wings and wake region recovery. The replenishment of streamwise momentum in both MRS configurations is primarily driven by advection, with external wings significantly enhancing this process. Moreover, the evaluation of mean momentum fluxes highlights a significant vertical upward momentum flux due to wing-induced upwash, promoting high-momentum flow influx through the sides and bottom of the MRS. Consequently, this influx significantly enhances power recovery, confirmed by the evaluation of mean velocity deficit recovery. Specifically, at x/D=2.0, the MRS with external wings exhibits a 44% increase in mean velocity directly downstream of the actuator surface, coupled with a notably enhanced recovery rate. These findings underscore the beneficial impact of external wings on wake recovery in VAWT-based MRS.

What is the effect of the external lift-generating wings on the thrust coefficient of the VAWT-based MRS?

From the load measurements, it is found that the thrust coefficient of the VAWT-based MRS without external wings increases with tip-speed ratio, resembling the behaviour of a single-rotor VAWT. This behaviour is also observed for the MRS configuration with external wings. Additionally, the external lift-generating devices are found to slightly increase the thrust induced by the MRS for a given TSR. This effect has been attributed to an increase in velocity at the actuator plane originating from the accelerated flow on the suction side of the external wings.

In conclusion, this study has provided a thorough investigation into the near-wake dynamics of VAWT-based Multi-Rotor Systems and the impact of external lift-generating devices on their wake recovery and power performance. Through a wind tunnel experiment in the OJF of the TU Delft, key insights have been gained into the flow characteristics, evolution of flow structures, and correlations between external wing presence and wake recovery. Notably, the presence of external wings has demonstrated a positive influence on wake re-energization and power recovery. These findings hold

considerable promise for enhancing the efficiency and performance of the VAWT-based MRS within wind farm applications, marking a noteworthy stride towards the advancement of innovative wind energy solutions.

5.2. Recommendations

The current work serves as an interesting proof of concept for the VAWT-based MRS and the concept of wake deflection through external cross-flow loading. While the results obtained are promising, it's crucial to critically assess the main limitations of this work and identify avenues for future research and improvement. This section outlines recommendations aimed at addressing these limitations and advancing future investigations.

When it comes to the current research, an important note must be made regarding the wind tunnel model and any induced flow blockage effects. Generally, when performing experiments in a wind tunnel environment, corrections are applied to the obtained data to account for the difference in conditions between the wind tunnel environment and the real world. Due to the complexity and novelty of the current model, where the MRS comprises multiple VAWT rotors, a support frame, and two high-lift wings, no such corrections have been applied. It is however important to acknowledge that these blockage effects were at play during the experiment. In particular, it was observed that the cross-flow loading imposed by the external wings created a significant disturbance to the wind tunnel jet. Despite this, the results presented in this work provide a credible proof-of-concept for this novel wind turbine design but this also stipulates the importance of quantifying the induced blockage effects by for example a detailed numerical study.
Another avenue for future research was already touched upon in subsection 4.3.5, where the recovery of the mean velocity deficit in the near-wake of the MRS was discussed. The analysis in this section showed that at x/D=2.0 the wake of both MRS configurations was still developing. The results presented therefore do not tell the full story regarding the recovery of the wake. Delving into the behaviour of the far-wake region will provide a more comprehensive understanding of the system's potential and allow for a more accurate assessment of the recovery of the wake.

When it comes to the behaviour of the wake, many design aspects of the VAWT-based MRS are expected to contribute to this. Examples are rotor spacing and rotational direction, but also VAWT-rotor blade angle of attack. Understanding how these design aspects influence the wake dynamics holds significant implications for optimizing MRS performance. In the work of [28] for example, it was presented that rotor blade pitch significantly affects the behaviour of the wake of individual VAWTs. Combining this technique with the concept of wake control through cross-flow loading may lead to narrower wakes that ascend more rapidly. Experimenting with these design variables can unveil the most effective setup for achieving this desired outcome. By conducting thorough investigations into these aspects, researchers can identify optimal rotor configurations that enhance energy capture and wake management.

Continuing on the concept of enhancing wake deflection and re-energization through external cross-flow loading, numerous unknowns remain that require further investigation. The most important aspect to understand is how different lift and circulation strengths affect the behaviour of the wake. Moreover, exploring the impact of various wing placements on the dynamics of the wake to determine the optimal locations on the MRS would offer valuable insights. Similarly, examining the effects of diverse wing configurations, such as using single or multiple wings, can provide valuable perspectives on different design choices for the MRS.
Additionally, in the background section on wind farm aerodynamics, the VAWT-based MRS was recognized as a promising platform for augmenting the mixing of the Atmospheric Boundary Layer, thereby enhancing flow velocities in areas where power extraction occurs. The current study did however not provide any insights into this potential, as no ABL was simulated during the experiments. To address this gap and evaluate the effectiveness of the VAWT-based MRS in enhancing boundary layer mixing and wind turbine power production, a study akin to that of Chamorro and Porté-Agel [17] is recommended. Conducting experiments with the turbine immersed in a simulated ABL environment can offer valuable insights into the platform's capability to enhance power generation by effectively mixing the Earth's boundary layer.

Lastly, to extend the study's relevance to real-world wind energy applications, investigating the behaviour of multiple MRS configurations within wind farm conditions is imperative. This exploration can provide invaluable insights into how MRS interacts within larger wind energy infrastructures and its overall impact on wind farm performance.

When it comes to the recommended research on the topic of wake deflection and re-energization through cross-flow loading, as well as enhancing the mixing of the ABL using external lift-generating devices, there arises the opportunity of utilising a simplified MRS model. In the current work, it was demonstrated that the wake of the MRS at x/D=2.0 already exhibits a relatively uniform behaviour. Replacing the VAWT rotors with one or multiple actuator discs, similar to what has been done by Huang et al [29] for single-rotor VAWTs, therefore appears to be a viable option. Taking this approach allows for testing the effects of many different combinations of turbine thrust coefficients, circulation strengths, and external wing placements on the far wake of the MRS. Furthermore, such a simplified model could prove valuable when analyzing the MRS within a wind farm configuration.

References

[1] IRENA (2023). *World Energy Transitions Outlook 2023: 1.5°C Pathway*. Tech. rep. International Renewable Energy Agency, 2023. URL: https://www.irena.org/Publications/2023/Jun/World-Energy-Transitions-Outlook-2023.

[2] T. Ackermann and L. Söder. "An overview of wind energy-status 2002". In: *Renewable and Sustainable Energy Reviews* 6.1 (2002), pp. 67–127. ISSN: 1364-0321. DOI: https://doi.org/10.1016/S1364-0321(02)00008-4.

[3] H.C. Garner et al. *Subsonic Wind Tunnel Wall Corrections*. Tech. rep. 109. AGARD, 1966.

[4] J.D. Anderson. *Fundamentals of Aerodynamics*. McGraw-Hill Education, 2017. ISBN: 9781259251344.

[5] J.B. Barlow, W.H. Rae, and A. Pope. *Low-Speed Wind Tunnel Testing*. 3rd ed. John Wiley & Sons, 1999. ISBN: 0-471-55774-9.

[6] M. Bastankhah and M. Abkar. "Multirotor wind turbine wakes". In: *Physics of Fluids* 31.8 (Aug. 2019), p. 085106. ISSN: 1070-6631. DOI: 10.1063/1.5097285.

[7] M. Bastankhah and F. Porté-Agel. "Experimental and theoretical study of wind turbine wakes in yawed conditions". In: *Journal of Fluid Mechanics* 806 (2016), pp. 506–541. DOI: 10.1017/jfm.2016.595.

[8] F. Bauer et al. "Drag power kite with very high lift coefficient". In: *Renewable Energy* 118 (Apr. 2018), pp. 290–305. DOI: 10.1016/j.renene.2017.10.073.

[9] R. Binda et al. *Media reaction: Extreme weather hits world's seven continents in July 2023*. 2023. URL: https://www.carbonbrief.org/media-reaction-extreme-weather-hits-worlds-seven-continents-in-july-2023/ (visited on 08/22/2023).

[10] J. Bossuyt et al. "Quantification of wake shape modulation and deflection for tilt and yaw misaligned wind turbines". In: *Journal of Fluid Mechanics* 917 (2021). DOI: 10.1017/jfm.2021.237.

[11] M. Boudreau and G. Dumas. "Comparison of the wake recovery of the axial-flow and cross-flow turbine concepts". In: *Journal of Wind Engineering and Industrial Aerodynamics* 165 (2017), pp. 137–152. ISSN: 0167-6105. DOI: https://doi.org/10.1016/j.jweia.2017.03.010.

[12] L.K. Brandt and K.K. Nomura. "Characterization of the interactions of two unequal co-rotating vortices". In: *Journal of Fluid Mechanics* 646 (2010), pp. 233–253. DOI: 10.1017/S0022112009992849.

[13] E. Buckingham. "On Physically Similar Systems; Illustrations of the Use of Dimensional Equations". In: *Phys. Rev.* 4 (4 1914), pp. 345–376. DOI: 10.1103/PhysRev.4.345.

[14] F. Campagnolo et al. "Wind tunnel testing of wake control strategies". In: July 2016, pp. 513–518. DOI: 10.1109/ACC.2016.7524965.

[15] H. Canet, P. Bortolotti, and C. L. Bottasso. "On the scaling of wind turbine rotors". In: *Wind Energy Science* 6.3 (2021), pp. 601–626. DOI: 10.5194/wes-6-601-2021.

[16] G.C.A. Caridi. "Development and application of helium-filled soap bubbles". PhD thesis. Delft, Netherlands: Delft University of Technology, 2018.

[17] L. Chamorro and F. Porté-Agel. "A Wind-Tunnel Investigation of Wind-Turbine Wakes: Boundary-Layer Turbulence Effects". In: *Boundary-Layer Meteorology* 132 (Dec. 2008), pp. 129–149. DOI: 10.1007/s10546-009-9380-8.

[18] D. De Tavernier. "Aerodynamic advances in vertical-axis wind turbines". PhD thesis. Delft University of Technology, Feb. 2021. DOI: 10.4233/uuid:7086f01f-28e7-4e1b-bf97-bb3e38dd22b9.

[19] L. Distelbrink et al. "30MW Multi-Rotor Turbine Block Design". Bachelor's Thesis. Delft University of Technology, 2023.

[20] G. Elsinga et al. "Tomographic Particle Image Velocimetry". In: *Experiments in Fluids* 41 (Dec. 2006), pp. 933–947. DOI: 10.1007/s00348-006-0212-z.

[21] C. Ferreira. "The near wake of the VAWT: 2d and 3d views of the VAWT aerodynamics". PhD thesis. Delft, Netherlands: Delft University of Technology, 2009.

[22] P. Fleming et al. "Field test of wake steering at an offshore wind farm". In: *Wind Energy Science* 2.1 (2017), pp. 229–239. DOI: 10.5194/wes-2-229-2017.

[23] N. S. Ghaisas, A. S. Ghate, and S. K. Lele. "Large-eddy simulation study of multi-rotor wind turbines". In: *Journal of Physics: Conference Series* 1037.7 (June 2018), p. 072021. DOI: 10.1088/1742-6596/1037/7/072021.

[24] D. Giaquinta. "The Flow Topology of the Ahmed Body in Cross-Wind". Master's thesis. Delft University of Technology, 2018.

[25] N. Hamilton et al. "Statistical analysis of kinetic energy entrainment in a model wind turbine array boundary layer". In: *Journal of Renewable and Sustainable Energy* 4.6 (Nov. 2012), p. 063105. DOI: 10.1063/1.4761921.

[26] U. Hebbar et al. "Analysis of Interactional Aerodynamics in Multi-Rotor Wind Turbines using Large Eddy Simulations". In: vol. 1489. 2020. DOI: 10.2514/6.2020-1489.

[27] M. Howland, S. Lele, and J. Dabiri. "Wind farm power optimization through wake steering". In: *Proceedings of the National Academy of Sciences* 116 (July 2019), p. 201903680. DOI: 10.1073/pnas.1903680116.

[28] M. Huang, A.a Sciacchitano, and C. Ferreira. "On the wake deflection of vertical axis wind turbines by pitched blades". In: *Wind Energy* 26.4 (2023), pp. 365–387. DOI: https://doi.org/10.1002/we.2803.

[29] M. Huang et al. "Experimental Comparison of the Wake of a Vertical Axis Wind Turbine and Planar Actuator Surfaces". In: *Journal of Physics: Conference Series* 1618.5 (Sept. 2020), p. 052063. DOI: 10.1088/1742-6596/1618/5/052063.

[30] A. Jadeja. "Wake deflection technique for vertical axis wind turbines using actuator line model in OpenFOAM". MSc. thesis. Delft, Netherlands: Delft University of Technology, 2018.

[31] P. Jamieson. *Innovation in wind turbine design*. 2nd ed. Wiley and Sons Ltd., 2018. ISBN: 978-1-119-13790-0.

[32] P. Jamieson et al. "Development of a multi rotor floating offshore system based on vertical axis wind turbines". In: *J. Phys.: Conf. Ser.* 2257 (2022), p. 012002. DOI: 10.1088/1742-6596/2257/1/012002.

[33] P. Jamieson et al. *Innovative Turbine Concepts - Multi-Rotor System*. Tech. rep. 1.33. Innwind.EU, 2015.

[34] Á. Jiménez, A. Crespo, and E. Migoya. "Application of a LES technique to characterize the wake deflection of a wind turbine in yaw". In: *Wind Energy* 13.6 (2010), pp. 559–572. DOI: https://doi-org.tudelft.idm.oclc.org/10.1002/we.380.

[35] M. P. van der Laan et al. "Power curve and wake analyses of the Vestas multi-rotor demonstrator". In: *Wind Energy Science* 4.2 (2019), pp. 251–271. DOI: 10.5194/wes-4-251-2019.

[36] B. LeBlanc and C. Ferreira. "Estimation of blade loads for a variable pitch vertical axis wind turbine from particle image velocimetry". In: *Wind Energy* 25 (Aug. 2021). DOI: 10.1002/we.2674.

[37] S. Lee et al. "Atmospheric and Wake Turbulence Impacts on Wind Turbine Fatigue Loading". In: (Jan. 2012). DOI: 10.2514/6.2012-540.

[38] R.H. Liebeck. "Design of Subsonic Airfoils for High Lift". In: *Journal of Aircraft* 15.9 (1978), pp. 547–561. DOI: 10.2514/3.58406.

[39] L.E.M. Lignarolo et al. "Experimental analysis of the wake of a horizontal-axis wind-turbine model". In: *Renewable Energy* 70 (2014). Special issue on aerodynamics of offshore wind energy systems and wakes, pp. 31–46. DOI: https://doi.org/10.1016/j.renene.2014.01.020.

[40] C.A. Lyon et al. *Summary of Low-Speed Airfoil Data*. Vol. 3. SoarTech Publications, 1997. ISBN: 0-9646747-3-4.

[41] J. McMorland et al. "A review of operations and maintenance modelling with considerations for novel wind turbine concepts". In: *Renewable and Sustainable Energy Reviews* 165 (2022), p. 112581. DOI: https://doi.org/10.1016/j.rser.2022.112581.

[42] S. McTavish, D. Feszty, and F. Nitzsche. "A study of the performance benefits of closely-spaced lateral wind farm configurations". In: *Renewable Energy* 59 (2013), pp. 128–135. DOI: https://doi.org/10.1016/j.renene.2013.03.032.

[43] D. Medici and H. Alfredsson. "Wind Turbine Near Wakes and Comparisons to the Wake Behind a Disc". In: *43rd AIAA Aerospace Sciences Meeting and Exhibit*. AIAA. Jan. 2005.

[44] D. Medici and P. H. Alfredsson. "Measurements on a wind turbine wake: 3D effects and bluff body vortex shedding". In: *Wind Energy* 9.3 (2006), pp. 219–236. DOI: https://doi-org.tudelft.idm.oclc.org/10.1002/we.156.

[45] Engineering National Academies of Sciences and Medicine. *Wind Turbine Generator Impacts to Marine Vessel Radar*. Washington, DC: The National Academies Press, 2022. ISBN: 978-0-309-27548-4. DOI: 10.17226/26430.

[46] F. Porté-Agel, M. Bastankhah, and S. Shamsoddin. "Wind-Turbine and Wind-Farm Flows: A Review". In: *Boundary-Layer Meteorology* 174.1 (2020), pp. 1–59. DOI: 10.1007/s10546-019-00473-0.

[47] V. F-C. Rolin and F. Porté-Agel. "Experimental investigation of vertical-axis wind-turbine wakes in boundary layer flow". In: *Renewable Energy* 118 (2018), pp. 1–13. DOI: https://doi.org/10.1016/j.renene.2017.10.105.

[48] K. Ryan et al. "Three-dimensional flow field around and downstream of a subscale model rotating vertical axis wind turbine". In: *Experiments in Fluids* 57 (Feb. 2016). DOI: 10.1007/s00348-016-2122-z.

[49] F. Scarano. "Tomographic PIV: Principles and practice". In: *Measurement Science and Technology* 24 (Oct. 2012), p. 012001. DOI: 10.1088/0957-0233/24/1/012001.

[50] D. Schanz, S. Gesemann, and A. Schröder. "Shake-The-Box: Lagrangian particle tracking at high particle image densities". In: *Experiments in Fluids* 57 (Apr. 2016). DOI: 10.1007/s00348-016-2157-1.

[51] D. Schanz et al. "Non-uniform optical transfer functions in particle imaging: calibration and application to tomographic reconstruction". In: *Measurement Science and Technology* 24 (2013), p. 024009. DOI: 10.1088/0957-0233/24/2/024009.

[52] J. Schottler et al. "Wind tunnel experiments on wind turbine wakes in yaw: redefining the wake width". In: *Wind Energy Science* 3.1 (2018), pp. 257–273. DOI: 10.5194/wes-3-257-2018.

[53] J. Scott. *Nacelle Vortex Generator*. Accessed on October 25, 2023. 2005. URL: https://aerospaceweb.org/question/aerodynamics/q0255.shtml.

[54] M.S. Selig et al. *Summary of Low-Speed Airfoil Data*. Vol. 1. SoarTech Publications, 1995. ISBN: 0-9646747-1-8.

[55] M.S. Selig et al. *Summary of Low-Speed Airfoil Data*. Vol. 2. SoarTech Publications, 1996. ISBN: 0-9646747-2-6.

[56] A. Seshagiri, E. Cooper, and L. Traub. "Effects of Vortex Generators on an Airfoil at Low Reynolds Numbers". In: *Journal of Aircraft - J AIRCRAFT* 46 (Jan. 2009), pp. 116–122. DOI: 10.2514/1.36241.

[57] G. Sieros et al. "Upscaling wind turbines: theoretical and practical aspects and their impact on the cost of energy". In: *Wind Energy* 15.1 (2012), pp. 3–17. DOI: https://doi-org.tudelft.idm.oclc.org/10.1002/we.527.

[58] A. M. O. Smith. "High-Lift Aerodynamics". In: *Journal of Aircraft* 12.6 (1975), pp. 501–530. DOI: 10.2514/3.59830.

[59] N. N. Sørensen et al. "Prediction of the Effect of Vortex Generators on Airfoil Performance". In: *Journal of Physics: Conference Series* 524.1 (June 2014), p. 012019. DOI: 10.1088/1742-6596/524/1/012019.

[60] D. Ştefănescu. "Strain gauges and Wheatstone bridges — Basic instrumentation and new applications for electrical measurement of non-electrical quantities". In: Mar. 2011, pp. 1–5. DOI: 10.1109/SSD.2011.5767428.

[61] R.J.A.M. Stevens and C. Meneveau. "Flow Structure and Turbulence in Wind Farms". In: *Annual Review of Fluid Mechanics* 49.1 (2017), pp. 311–339. DOI: 10.1146/annurev-fluid-010816-060206.

[62] J.M.I. Strickland and R.J.A.M. Stevens. "Effect of thrust coefficient on the flow blockage effects in closely-spaced spanwise-infinite turbine arrays". In: *Journal of Physics: Conference Series* 1618.6 (Sept. 2020), p. 062069. DOI: 10.1088/1742-6596/1618/6/062069.

[63] D. De Tavernier et al. "Towards the understanding of vertical-axis wind turbines in double-rotor configuration." In: *Journal of Physics: Conference Series* 1037.2 (June 2018), p. 022015. DOI: 10.1088/1742-6596/1037/2/022015.

[64] G. Tescione et al. "Near wake flow analysis of a vertical axis wind turbine by stereoscopic particle image velocimetry". In: *Renewable Energy* 70 (Oct. 2014), pp. 47–61. DOI: 10.1016/j.renene.2014.02.042.

[65] R.R. Trieling, O.U. Fuentes, and G.J.F. van Heijst. "Interaction of two unequal corotating vortices". In: *Physics of Fluids* 17.8 (July 2005), p. 087103. DOI: 10.1063/1.1993887.

[66] C.P. van Dam. "The aerodynamic design of multi-element high-lift systems for transport airplanes". In: *Progress in Aerospace Sciences* 38.2 (2002), pp. 101–144. ISSN: 0376-0421. DOI: https://doi.org/10.1016/S0376-0421(02)00002-7.

[67] A. Vergaerde et al. "Experimental validation of the power enhancement of a pair of vertical-axis wind turbines". In: *Renewable Energy* 146 (2020), pp. 181–187. ISSN: 0960-1481. DOI: https://doi.org/10.1016/j.renene.2019.06.115.

[68] A. Vergaerde et al. "Influence of the direction of rotation on the wake characteristics of closely spaced counter-rotating vertical-axis wind turbines". In: *Journal of Physics: Conference Series* 1618.6 (Sept. 2020), p. 062017. DOI: 10.1088/1742-6596/1618/6/062017.

[69] C. VerHulst and C. Meneveau. "Altering Kinetic Energy Entrainment in Large Eddy Simulations of Large Wind Farms Using Unconventional Wind Turbine Actuator Forcing". In: *Energies* 8.1 (Jan. 2015), pp. 370–386. DOI: 10.3390/en8010370.

[70] C. Wang et al. "How realistic are the wakes of scaled wind turbine models?" In: *Wind Energy Science* 6.3 (2021), pp. 961–981. DOI: 10.5194/wes-6-961-2021.

[71] B. Wieneke. "Volume self-calibration for 3D particle image velocimetry". In: *Experiments in Fluids* 45 (2008), pp. 549–556. DOI: 10.1007/s00348-008-0521-5.

[72] WindEurope. *Wind energy in Europe: 2022 Statistics and the outlook for 2023-2027*. Tech. rep. WindEurope, 2023. URL: https://windeurope.org/intelligence-platform/product/wind-energy-in-europe-2022-statistics-and-the-outlook-for-2023-2027/.

[73] X.L. Xiong, S. Laima, and H. Li. "Experimental study of the wake of multi-rotor turbine". In: *Ocean Engineering* 269 (2023), p. 113594. ISSN: 0029-8018. DOI: https://doi.org/10.1016/j.oceaneng.2022.113594.

[74] S. Zanforlin and T. Nishino. "Fluid dynamic mechanisms of enhanced power generation by closely spaced vertical axis wind turbines". In: *Renewable Energy* 99 (2016), pp. 1213–1226. ISSN: 0960-1481. DOI: https://doi.org/10.1016/j.renene.2016.08.015.

[75] L. Zhan, S. Letizia, and G. Valerio Iungo. "LiDAR measurements for an onshore wind farm: Wake variability for different incoming wind speeds and atmospheric stability regimes". In: *Wind Energy* 23.3 (2020), pp. 501–527. DOI: https://doi-org.tudelft.idm.oclc.org/10.1002/we.2430.